Studies on an initial top quark mass measurement at ATLAS in the lepton+jets $t\bar{t}$ decay channel and alignment of the Pixel and SCT subdetectors

Roland Härtel

Max-Planck-Institut für Physik
(Werner-Heisenberg-Institut)

TECHNISCHE UNIVERSITÄT MÜNCHEN

Max-Planck-Institut für Physik
(Werner Heisenberg Institut)

Studies on an initial top quark mass measurement at ATLAS in the lepton+jets $t\bar{t}$ decay channel and alignment of the Pixel and SCT subdetectors

Roland Härtel

Abstract

The main topic of this thesis is a commissioning style top quark mass analysis using the ATLAS experiment at CERN. The analysis focusses on top quark pair decays in the lepton+jets decay channel. Only kinematic selection cuts and no b-tagging information is used for the event selection. This analysis is suitable for the commissioning phase of the ATLAS detector, with not yet final calibration and an incomplete understanding of the detector performance.

Different methods for the reconstruction of the hadronic side of the top quark pair decays are studied and the effect of imposing the known W boson mass as constraint on the reconstruction is investigated. The analysis is modified in several ways to estimate the influence of systematic effects. The influence of the jet selection kinematics on the reconstructed top quark mass is studied, as well as the underlying jet algorithm definition and variations of the jet energy scale. The different jet algorithms under consideration are cone type and k_{T} type algorithms with a set of different steering parameters. The cone jet algorithm with the steering parameter $R_{\mathrm{cone}} = 0.4$ and the inclusive k_{T} algorithm with the steering parameter $R = 0.4$ give the best performance.

Although the top quark mass analysis is suited for the commissioning phase of the ATLAS detector, the performance of the ATLAS detector still affects the quality of the event selection. A high quality alignment of the ATLAS Inner Detector is required for an efficient lepton reconstruction and consequently for an optimal event selection. In the second part of this thesis the *Local* χ^2 alignment approach is presented. The approach is used for the alignment of the Pixel and SCT subdetectors. The approach is first validated on a small detector setup with data that was collected in a combined testbeam run in 2004. Finally the *Local* χ^2 alignment approach is used for the alignment of the whole Pixel and SCT subdetectors with cosmic ray data collected in fall 2008. The results obtained in this thesis have in part already been published in [1–3].

Zusammenfassung

Der Schwerpunkt dieser Arbeit sind Studien für eine Topquarkmassenanalyse mit dem ATLAS Experiment am CERN. Die Analyse ist für die Phase der Inbetriebnahme des ATLAS Detektors gedacht und beschränkt sich auf Topquarkpaarzerfälle in dem Lepton+Jets Zerfallskanal. Für die Ereignisselektion werden ausschließlich kinematische Selektionsschnitte verwendet und bewusst keine b-tagging Information. Dadurch ist die Analyse für die anfängliche Inbetriebnahmephase des ATLAS Detektors geeignet. Diese Phase wird von vorläufiger Detektorkalibrierung und unvollständiger Kenntnis über das Leistungsvermögen des Detektors geprägt sein.

Verschiedene Methoden zur Rekonstruktion der hadronischen Seite des Topquarkpaarzerfalls werden untersucht, insbesondere wird untersucht, welchen Effekt die bekannte W-Bosonmasse als Zwangsbedingung für die Rekonstruktion hat. Die Analyse wird an verschiedenen Stellen modifiziert um den Einfluss systematischer Unsicherheiten abzuschätzen. Im Einzelnen werden der Einfluss der Jetselektionskinematik auf die rekonstruierte Topquarkmasse, der Einfluss der zugrunde liegenden Jetdefinition und Veränderungen der Jetenergieskala untersucht. Die verschiedenen untersuchten Jetdefinitionen sind Cone-Algorithmen und k_T-Algorithmen mit jeweils unterschiedlichen Sätzen an Steuerungsparametern. Der Cone-Jetalgorithmus mit dem Steuerungsparameter $R_\mathrm{cone} = 0.4$ und der inklusive k_T-Jetalgorithmus mit dem Steuerungsparameter R = 0.4 zeigen das beste Verhalten.

Obwohl die Topquarkmassenanalyse für die Inbetriebnahmephase von ATLAS ausgelegt ist, wird die Güte der Ereignisselektion von dem Leistungsvermögen des ATLAS Detektors abhängen. Ein qualitativ hochwertiges Alignment des Inneren Detektors von ATLAS ist die Vorraussetzung für eine effiziente Leptonrekonstruktion und dadurch für eine optimale Ereignisselektion. Im zweiten Teil dieser Arbeit wird daher die *Local* χ^2 Alignment Methode vorgestellt. Die Methode wird für das Alignment der Pixel und SCT Teildetektoren verwendet. Zuerst wird die Methode mit Daten validiert, die während eines kombinierten Teststrahls im Jahr 2004 mit einem kleinen Detektoraufbau aufgezeichnet wurden. Schließlich wird die *Local* χ^2 Methode für das Alignment der gesamten Pixel und SCT Teildetektoren verwendet, mit Daten der kosmischen Strahlung, die im Herbst 2008 aufgezeichnet wurden. Ein Teil der in dieser Arbeit vorgestellten Ergebnisse wurde bereits in den Referenzen [1–3] veröffentlicht.

Contents

Overview

Within the scope of this thesis a commissioning style top quark mass analysis at the ATLAS detector was explored and the effects of various systematic variations were studied. The results and findings are described. Also, an alignment of the ATLAS Pixel and SCT subdetectors was performed and the details and results of this are presented. The work is split into six chapters that are structured as follows:

- **Chapter 1 – The Standard Model of particle physics**
  A short summary of the Standard Model of particle physics is presented. The mechanism of top quark production in pp collisions and relevant details about the top quark decay are discussed in more detail.

- **Chapter 2 – The Large Hadron Collider and the ATLAS experiment**
  The Large Hadron Collider is described and the concept of luminosity is introduced. The multipurpose ATLAS detector is portrayed and the relevance of each subdetector for top quark physics is highlighted. The Pixel and SCT subdetectors are described in more detail as they will be relevant for the alignment presented in Chapter 5.

- **Chapter 3 – Top quark mass analysis**
  A "commissioning style" top quark mass analysis is presented. The event signature, the background processes, the Monte Carlo datasets and the event selection are described. Various methods for top quark mass reconstruction are portrayed and the results and findings are discussed.

- **Chapter 4 – Systematic effects**
  This Chapter deals with the influence of various systematic effects on the top quark mass analysis. The influence of a variation of the jet selection cuts, a variation of the underlying jet algorithm definition (cone type and k_T type jets) and a variation of the jet energy scale are investigated. The results and findings are discussed.

- **Chapter 5 – Alignment of the ATLAS Inner Detector**
  The *Local* χ^2 alignment approach is introduced and the performance of the *Local* χ^2 approach on combined testbeam data is presented. The results are discussed and compared with the results of other alignment approaches. Finally the performance of the *Local* χ^2 approach with recent ATLAS cosmic data is described.

- **Chapter 6 – Conclusions**
  The main results of the preceding chapters are summarized. Ongoing developments and unresolved issues are pointed out and prospective future developments are discussed briefly.

Chapter 1

The Standard Model of particle physics

The Standard Model of particle physics is a quantum field theory (i.e. a combination of quantum mechanics and relativity) that describes the properties and interactions of fundamental particles [4–7]. It is in agreement with experimental data up to $\mathcal{O}(200)\,\text{GeV}$. All particles of the Standard Model, save the Higgs boson, have been discovered and so far no particle beyond the Standard Model has been observed [8]. Despite its success there are open questions that cannot be answered within the Standard Model, e.g. it does not describe gravitation and it has no dark matter candidate (the merely gravitationally interacting matter permeating the universe). These open questions motivate theories beyond the Standard Model like supersymmetric extensions of the Standard Model [9], large extra dimensions [10] or string theory [11].

A firm understanding of the Standard Model is necessary to discover phenomena beyond the Standard Model. Especially reactions at high energies like top quark pair production and decay need to be thoroughly understood to be able to distinguish the Standard Model from observations of physics beyond the Standard Model.

1.1 The Standard Model

Quantum field theory extends quantum mechanics into the realm of relativity and introduces the 2nd quantization, namely the quantization of the force fields themselves. A particular quantum field theory is known as the Standard Model and is based on the fermion fields shown in Table 1.1, the bosonic gauge fields that arise from the Standard Model gauge group $\text{U}(1)_Y \times \text{SU}(2)_L \times \text{SU}(3)_C$ and the scalar Higgs field.

So far the Standard Model is the best description of fundamental particles and their interactions, apart from gravitational effects. The fundamental fermions of the Standard Model are leptons and quarks that are grouped into three generations as shown in Table 1.1 [12]. A feature of these three generations is that 2nd generation fermions are heavier than their 1st generation cousins and that 3rd generation fermions are heavier still. The heaviest

fermion described by the Standard Model is the up-type quark of the 3rd generation, the so called top quark with a measured mass of 172.6 GeV * [13].

Generation	1	2	3
left-handed leptons	$\begin{pmatrix} \nu^e \\ e \end{pmatrix}_L$	$\begin{pmatrix} \nu^\mu \\ \mu \end{pmatrix}_L$	$\begin{pmatrix} \nu^\tau \\ \tau \end{pmatrix}_L$
right-handed leptons	ν_R^e e_R	ν_R^μ μ_R	ν_R^τ τ_R
left-handed quarks	$\begin{pmatrix} u \\ d \end{pmatrix}_L$	$\begin{pmatrix} c \\ s \end{pmatrix}_L$	$\begin{pmatrix} t \\ b \end{pmatrix}_L$
right-handed quarks	u_R d_R	c_R s_R	t_R b_R

Table 1.1: *The three generations of fermions of the Standard Model are grouped into leptons and quarks. The gauge group $SU(2)_L$ makes the Standard Model a chiral theory where left-handed and right-handed fermions behave differently. Left-handed fermion fields are doublets, whereas right-handed fermion fields are singlets. So far no right-handed neutrinos have been observed, although the existence of nonzero neutrino masses implies that they exist.*

1.1.1   Quantum Chromodynamics

The part of the Standard Model describing the strong interaction is called Quantum Chromodynamics (QCD). It is represented by the $SU(3)_C$ symmetry group based on color charges. The color field is mediated by eight massless spin-1 bosons called gluons. Gluons are color-charged themselves, so they self-interact via 3-gluon and 4-gluon vertices. This non-Abelian nature of $SU(3)_C$ and the scale dependence of the strong coupling constant α_s give rise to the very complex dynamical structure of QCD, particularly asymptotic freedom and confinement.

The QCD coupling constant α_s is a function of the energy scale μ_r of a specific interaction. The coupling constant $\alpha_s(\mu_r^2)$ decreases with increasing μ_r^2 and vanishes asymptotically. Thus, for large μ_r^2 or very short distances the strong interaction becomes indeed weak and quarks in this regime behave asymptotically free [14].

On the other hand $\alpha_s(\mu_r)$ becomes large at large distances or small μ_r, so large in fact that a perturbative description of QCD is no longer applicable. This gives rise to the property of QCD called confinement. Confinement describes the impossibility of separating two colored partons to create an unbound colored object. The increasing interaction energy of separated color charges triggers a process called hadronization in which quark-antiquark-pairs are created from the vacuum and, together with the original partons, group themselves to form observable color neutral bound states called hadrons.

In a hadronic collision, e.g. at the LHC (cf. Section 2.1), the collection of hadrons emanating from an original outgoing parton is called a jet. The theoretical and experimental properties of jets are further discussed in Section 4.2.

---

*In the following we set $\hbar = c = 1$

1.1.2   Electroweak interactions

In the Standard Model electromagnetic and weak interactions are unified into the electroweak interaction represented by the symmetry groups $U(1)_Y \times SU(2)_L$ where Y denotes hypercharge and L denotes handedness. The electroweak interaction is mediated by four spin-1 bosons, namely the massless photon and the massive $W^\pm$ and Z^0 bosons.

To conserve gauge invariance and to accommodate massive gauge bosons the electroweak symmetry group is spontaneously broken. In the Standard Model the spontaneous symmetry breaking is mediated by the Higgs mechanism where a doublet of complex scalar fields Φ is introduced [15]. The symmetry breaking comes from the fact that in the ground state (i.e. the field configuration at minimal energy) Φ does not vanish. While the photon stays massless the other three gauge bosons acquire mass by coupling to the non-vanishing scalar Higgs fields. Three of the four degrees of freedom of the scalar complex Higgs doublet are absorbed in this manner into the gauge boson masses (or more precisely into the degree of freedom coming from the longitudinal polarization of massive spin-1 particles). The field quant of the remaining field is a neutral spin-0 boson, the so called Higgs boson. Presently the Higgs boson is the only unobserved particle of the Standard Model. The discovery of the Higgs boson to verify the Higgs mechanism, or more generally the discovery of the mechanism of electroweak symmetry breaking is one of the main tasks of the LHC and its experiments (cf. Chapter 2).

The Higgs mechanism also provides a means for the a priori massless fermions to acquire mass as well. This happens via Yukawa coupling to the non-vanishing Higgs field:

$$m_f = \alpha_f \cdot v, \tag{1.1}$$

where m_f is the mass of a specific fermion, α_f is the Yukawa coupling constant for this fermion and v is the non-vanishing value of Φ for the ground state, i.e. the vacuum expectation value. From the gauge boson masses and the Fermi coupling constant G_F, v is calculated to be 174.1 GeV. From this follows that the top quark Yukawa coupling is close to unity which is remarkable in itself, but also raises the question whether the top quark plays an active role in electroweak symmetry breaking.

The weak interaction couples to the weak eigenstates of the fermion fields. These weak eigenstates are not identical with the eigenstates of the freely propagating fermions (the so called mass eigenstates). For down-type quarks and neutrinos the weak eigenstates are a mixture of the mass eigenstates of all three generations. The mixing between the two sets of eigenstates in the quark sector is parameterized by the 3×3 Cabbibo-Kobayashi-Maskawa mixing matrix (CKM matrix) [16, 17]. In the neutrino sector the mixing is parameterized by the 3×3 Pontecorvo-Maki-Nakagawa-Sakata matrix (PMNS matrix) [18, 19]. For the other fermions there is no distinction between mass and weak eigenstates.

1.2   Top quark physics

The top quark is the weak isospin partner of the bottom quark and by far the most massive elementary particle discovered so far. The top quark was first observed in 1995 at Fermilab [20, 21] and the current world average of the measured top quark mass is 172.6 GeV [13]. The top quark is a spin-$\frac{1}{2}$ fermion and has an electric charge of $+\frac{2}{3}$. It is produced and

decays via processes calculable within the Standard Model framework. In the following Sections top quark production and decay are described in more detail.

1.2.1 Top quark production

The top quark production cross section can be calculated by using a factorization approach [22]. The production process is factorized into a short-distance partonic cross section $\hat{\sigma}_{ij}$ and long-distance parton distribution functions (pdfs) f_i and f_j for the incoming partons i and j. To calculate the production cross section the pdfs and the partonic cross section are evaluated separately.

There are two main ways of top quark production at the LHC. Firstly there is top quark pair production via the strong interaction and secondly there is electroweak single top quark production [23]. The processes contributing to the partonic cross section of top quark pair production at lowest order are shown in Figure 1.1. The processes are $q\bar{q}$ annihilation and gluon-gluon fusion. The lowest order processes contributing to the partonic cross section of single top quark production are shown in Figure 1.2. The processes are top quark production in the s- and the t-channel, and associated production of a top quark and a W boson, the Wt-channel.
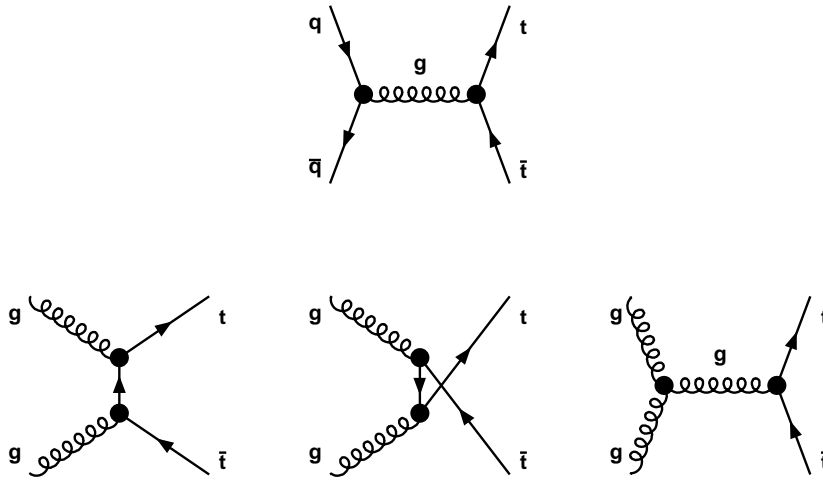
Figure 1.1: *Lowest order Feynman diagrams for top quark pair production.*

At the LHC the colliding protons provide broad band beams of partons with a momentum fraction of the incoming proton momentum. The pdf $f_i(x_i, \mu_f^2 = \mu_r^2)^*$ denote the probability density to observe a parton of flavor i with the momentum fraction x_i of the parent proton when probed at a scale μ_r^2. The pdfs are obtained from global QCD fits mainly to deep inelastic scattering data. An example pdf for $\mu_r^2 = (175\,\text{GeV})^2 \approx m_t^2$ is shown in Figure 1.3.

---

*For simplification the factorization scale μ_f^2 is identified with the renormalization scale μ_r^2

Figure 1.2: *Lowest order Feynman diagrams for single top quark production. The upper left diagram shows the s-channel process. The upper middle and upper right diagram show the t-channel processes. The two lower diagrams show the Wt-channel production processes.*

In summary, the production cross section for top pair production can be evaluated via the following equation:

$$\sigma_{t\bar{t}}(\sqrt{s}, m_{\mathrm{t}}^2) = \sum_{i,j=q,\bar{q},g} \int dx_i dx_j f_i(x_i, \mu_r^2) f_j(x_j, \mu_r^2) \cdot \hat{\sigma}^{ij \to t\bar{t}}(\sqrt{s}, m_{\mathrm{t}}^2, x_i, x_j, \mu_r^2) \qquad (1.2)$$

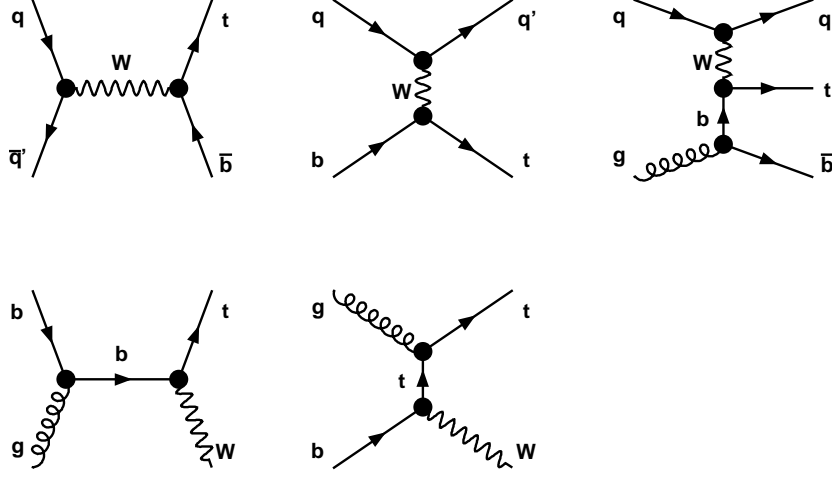with $\sqrt{s}$ the center-of-mass energy of the colliding protons. For proton-proton collisions at $\sqrt{s} = 14\,\mathrm{TeV}$ and $\sqrt{s} = 10\,\mathrm{TeV}$ the production cross sections for top quark pair production and single top quark production are listed in Table 1.2.

	top quark pair	single top quark		
	$\sigma_{t\bar{t}}$	$\sigma_{s-channel}$	$\sigma_{t-channel}$	$\sigma_{Wt-channel}$
LHC ($\sqrt{s} = 10\,\mathrm{TeV}$, pp)	425 pb	4.8 pb	149.6 pb	32.0 pb
LHC ($\sqrt{s} = 14\,\mathrm{TeV}$, pp)	933 pb	10.8 pb	249.1 pb	66.8 pb

Table 1.2: *Calculated cross sections for top quark pair and single top production at the LHC at different center-of-mass energies. $\sigma_{t\bar{t}}$ is calculated at NLO with NLL corrections. The pdf-set used is CTEQ6M and the assumed top quark mass $m_{\mathrm{t}} = 171\,GeV$ [25]. Single top cross sections are calculated at LO and scaled up to NLO. The pdf-set used is CTEQ6M and the assumed top quark mass $m_{\mathrm{t}} = 172\,GeV$ [26].*

1.2.2 Top quark decay

The top quark decays via the weak interaction into a W boson and a down-type quark. As the top quark mass is far above the Wq (q any down-type quark) threshold, the relative branching ratios B are given by the squares of the CKM matrix elements $|V_{td}|$, $|V_{ts}|$ and
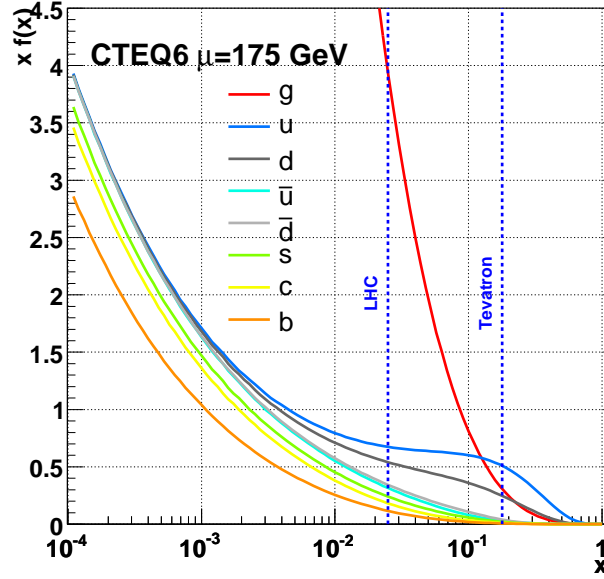
Figure 1.3: *Parton distribution functions, pdfs, for quarks and gluons in the proton as a function of the fractional momentum [24].*

$|V_{tb}|$. Assuming three generations of quarks and unitarity of the CKM matrix the values are estimated to be [23, 27]:

$$
\begin{aligned}
|V_{td}| &= 0.004 - 0.014 &\Rightarrow\quad B(t \to Wd) \approx 0.01\% \\
|V_{ts}| &= 0.037 - 0.044 &\Rightarrow\quad B(t \to Ws) \approx 0.1\% \\
|V_{tb}| &= 0.9990 - 0.9993 &\Rightarrow\quad B(t \to Wb) \approx 99.89\%
\end{aligned}
\tag{1.3}
$$

So, the top quark decay into d or s quarks is enormously suppressed and the top quark almost always decays into W boson and b quark.

For a weak decay the top quark lifetime is very short with a predicted decay width (at next-to-leading order) of $\Gamma_\mathrm{t} = 1.5\,\mathrm{GeV}$ (for $m_\mathrm{t} = 175\,\mathrm{GeV}$) corresponding to a lifetime of $0.5 \cdot 10^{-24}\,\mathrm{s}$ [28]. The top quark lifetime is too short for top flavored hadrons to form, or for $t\bar{t}$ quarkonium bound states to appear.

Top quark pair decays are classified according to the decay channels of the subsequent W-boson decays. A W boson can decay leptonically via $\mathrm{W}^- \to l\bar\nu$ into all three lepton generations or hadronically into a up-type/down-type quark-antiquark pair. In the hadronic decay channels the branching ratios are weighted by the squares of the relevant CKM matrix elements so that the predominant hadronic W decay modes are $\mathrm{W}^- \to \bar{u}d$ and $\mathrm{W}^- \to \bar{c}s$ with a decay into a 3rd generation quark pair kinematically inaccessible, and a decay into a b quark and a 1st- or 2nd generation up-type quark strongly suppressed.

The W boson decay branching fractions at lowest order are listed in Table 1.3. For the decay of top quark pairs this results in the following distinct decay channels:

decay mode	branching fraction
$W^- \to e\bar{\nu}_e$	1/9
$W^- \to \mu\bar{\nu}_\mu$	1/9
$W^- \to \tau\bar{\nu}_\tau$	1/9
$W^- \to \bar{q}q'$	6/9

Table 1.3: *Branching fractions of W boson decays at lowest order.*

- Both W bosons decay leptonically (**di-lepton channel**, $B = 1/9$).

- One W boson decays leptonically, the other hadronically (**lepton + jets channel**, $B = 4/9$).

- Both W bosons decay hadronically (**all jets channel**, $B = 4/9$).

Within the scope of the work presented here the lepton + jets channel is further restricted to W boson decays into electron or muon and the associated neutrino. This definition of the lepton + jets channel has a branching fraction of $B = 8/27$.

Chapter 2

The Large Hadron Collider and the ATLAS experiment

The Large Hadron Collider (LHC)[29] is an accelerator facility at CERN, Geneva with four main experiments (Alice[30], ATLAS[31], CMS[32], LHCb[33]). The following Chapter will focus on the LHC and the ATLAS detector, specifically on those properties of the accelerator and the detector that are relevant for top quark physics.

2.1 The Large Hadron Collider

The LHC is a circular p-p accelerator with a length of 27 km and designed for a center-of-mass energy of the colliding protons of $\sqrt{s} = 14\,\text{TeV}$. During the startup phase the center-of-mass energy will be only $\sqrt{s} = 10\,\text{TeV}$. A lower magnetic field strength is required to keep the proton beams on circular orbits in the case of 5 TeV proton energy than for 7 TeV. For the superconducting LHC magnets this means that the magnetic field strength will stay well below the critical field strength of about 8.5 T. A schematic drawing of the LHC can be see in Figure 2.1.

For colliders, the event rate of a certain process, e.g. top quark pair production, can be calculated via:

$$N = \mathscr{L} \cdot \sigma(\sqrt{s}) \tag{2.1}$$

where σ is the production cross section and depends on the center-of-mass energy of the colliding particles (cf. Equation 1.2). The proportionality factor $\mathscr{L}$ is called luminosity and depends entirely on the beam parameters of the accelerator.

At the LHC the two beams are not continuous but consist of bunches of protons (design value: 2808 bunches per beam). Each bunch contains a number of protons n and at one of the collision points (e.g. in the ATLAS detector) bunches collide with a collision frequency f. With this picture in mind the LHC luminosity can be approximated as

$$\mathscr{L} = \frac{f \cdot n^2}{4\pi\sigma_x\sigma_y}, \tag{2.2}$$

where σ_x and σ_y are the transverse width of the bunches in the horizontal and vertical directions.
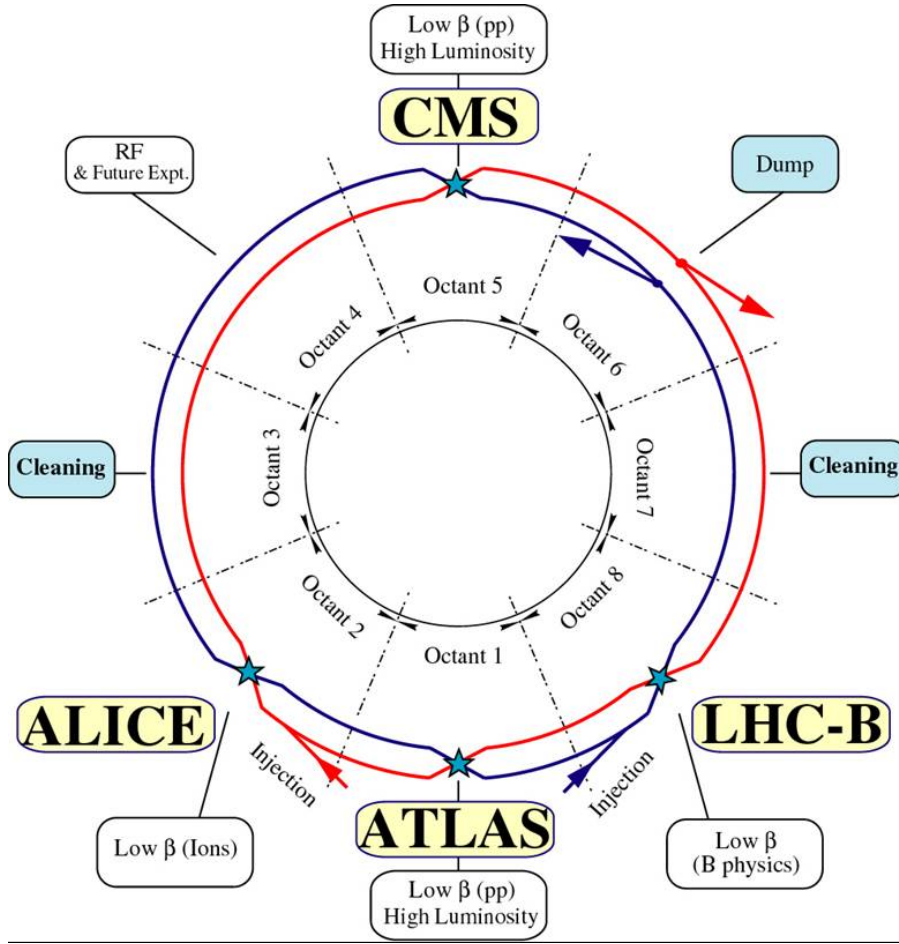
Figure 2.1: *Schematic drawing of the LHC where the interaction points for the four experiments are indicated.*

The relevant beam parameters are listed in Table 2.1. With these numbers the LHC design luminosity can be calculated as $\mathscr{L} = 1.5 \cdot 10^{34} \frac{1}{\text{cm}^2\text{s}}$. Initially $\mathscr{L}$ will be at a lower value in the range $10^{30} - 10^{32} \frac{1}{\text{cm}^2\text{s}}$, so that $1\,\text{fb}^{-1}$ of integrated luminosity can be expected for the first year of LHC operations. This startup period will be followed by a low luminosity running of LHC were $10\,\text{fb}^{-1}$ of integrated luminosity can be expected annually. Finally with $\mathscr{L}$ at its design value an integrated luminosity of $100\,\text{fb}^{-1}$ can be achieved per year.

	LHC design values
f	$40\,\text{MHz}$
n	$11.5 \cdot 10^{10}$
σ	$16.6\,\mu\text{m}$
$\sqrt{s}$	$14\,\text{TeV}$

Table 2.1: *Design values for the LHC beam parameters.*

2.2   The ATLAS experiment

The ATLAS detector is one of the two multipurpose experiments at the LHC (together with CMS). ATLAS is an acronym standing for <u>A</u> <u>T</u>oroidal <u>L</u>HC <u>A</u>pparatu<u>S</u> that describes the arrangement of the outer magnetic field of the detector. A sketch of the ATLAS detector is shown in Figure 2.2.
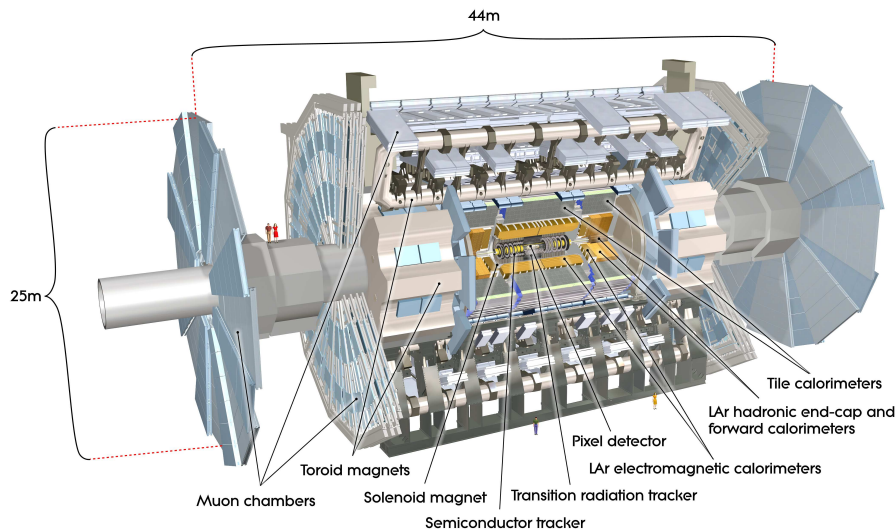
Figure 2.2: *Cut-away view of the ATLAS detector with labeled subdetectors.*

The ATLAS detector is designed to observe and measure a broad spectrum of physics processes [34, 35]. To achieve this task the detector measures properties of the decay products of the particles created in the LHC p-p collisions.

The global coordinate system of ATLAS is as follows:

- The positive X-direction points from the interaction point towards the center of the LHC ring.

- The positive Y-direction points from the interaction point upwards.

- the Z-direction is along the beamline with the positive direction such as to complete the right-handed orthogonal XYZ-coordinate system.

Two angular quantities ϕ and θ are defined as well and denote the azimuthal and polar angle around and towards the beamline. Another important quantity is the pseudorapidity η:

$$\eta = -\ln \tan(\frac{\theta}{2}). \tag{2.3}$$

Distances in η-ϕ-space are measured in ΔR:

$$\Delta\text{R} = \sqrt{\Delta\eta^2 + \Delta\phi^2}. \tag{2.4}$$

The quantities transverse momentum p_T, transverse energy E_T and missing transverse energy E_T^{miss} (i.e. an imbalance in the transverse energy distribution) are defined in the

X-Y plane. Particles created in hadron-hadron collisions are boosted along the beamline and p_T, E_T and E_T^{miss} are invariant under this boost.

One of the biggest challenges for ATLAS is to cope with the luminosity of LHC. At design luminosity the bunch collision rate will be 40 MHz (cf. Table 2.1). The final data-taking rate of ATLAS is approximately 200 Hz. Inbetween lies the trigger system of ATLAS that provides the necessary rejection factor [36, 37]. The trigger system is of paramount importance to efficiently select interesting events and reject the rest. Events that do not pass the trigger system are not written out and are lost for further reconstruction and analysis. The distinction which event is interesting to keep is made according to certain trigger menus that mimic the expected event signatures of the physics processes that ATLAS wants to cover (e.g. searches for the Higgs boson or super symmetry particles, top quark physics) [38].

As stated in Section 1.2.2 the decay products of top quark pairs in the lepton+jets channel are a lepton, its associated neutrino, two light quarks and two b quarks hadronizing into jets. To trigger, to reconstruct and to analyze these events requires all subdetector components of ATLAS. The subdetectors are listed in the following and their importance regarding this physics process is highlighted. A more detailed description of each subdetector is then given below.

- **The magnet system**:

    - Inner Detector solenoid
    - Muon system toroids

    The magnetic system provides magnetic fields that are required to measure the momenta of charged particles. Regarding top quark physics it is important for triggering high p_T muons and for lepton reconstruction in general.

- **The Inner Detector**:

    - Pixel detector
    - SemiConductor Tracker (SCT)
    - Transistion Radiation Tracker (TRT)

    The Inner Detector of ATLAS is closest to the interaction point and is used to measure the momenta of charge particles and to detect and reconstruct secondary vertices from the decays of particles coming from the primary interaction. This information is used for particle identification and in particular in the case of top quark physics also to distinguish b quark jets from light quark jets. The momentum measurement of the Inner Detector is used in the electron and muon reconstruction. The measurement of transition radiation in the TRT is used for electron identification.

- **The calorimeter**:

    - Electromagnetic calorimeters (EM barrel, EMEC, FCal1)
    - Hadronic calorimeters (Tile, HEC, FCal2, FCal3)

All ATLAS calorimeters are sampling calorimeters. The electromagnetic calorimeters identify and measure the energy of electrons and photons. They also measure the electromagnetic components of jets. The hadronic calorimeters measure the hadronic components of jets. The calorimeters also absorb most particles that come from the interaction point and thus act as radiation shielding for the ATLAS components outside of the calorimeter system. Muons interact only minimally in the calorimeters and escape into the outlying Muon system. Neutrinos do not interact in the calorimeters and escape ATLAS undetected. An imbalance in the transverse energy distribution (taking into account the muon measurement from the Muon system) is called missing transverse energy and is an indication for an escaped neutrino. The important features of the calorimeters for top quark physics are electron based triggering, accurate electron and jet reconstruction and determination of E_T^{miss}.

- **The muon system**:

  - Monitored Drift Tubes (MDT)
  - Cathode Strip Chambers (CSC)
  - Resistive Plate Chambers (RPC)
  - Thin Gap Chambers (TGC)

  The purpose of the ATLAS Muon system is twofold: accurate measurement of muon momenta and triggering on high p_T muons. The precision chambers MDT and CSC measure muon momenta, whereas RPC and TGC serve as the muon trigger system. For top quark physics both features (plus the Muon system contribution to the E_T^{miss} measurement) are necessary.

2.2.1 Magnet system

The configuration of the coils of the ATLAS magnets can be seen in Figure 2.3. Enclosing the volume of the Inner Detector is a superconducting solenoid, designed to provide a 2 T axial field parallel to the beamline. In the forward region of the Inner Detector the magnetic field becomes inhomogeneous and is of lower field strength as can be seen in Figure 2.4.

The magnets of the muon system consist of three toroids, a large central barrel toroid and two smaller end-cap toroids one in each forward direction. Each toroid consists of eight superconducting coils and provides a toroidal field around the beam axis. The field configuration of the toroid fields is highly non-uniform. Field strength values vary between 0.15 T - 2.5 T for the barrel toroid and 0.2 T - 3.5 T for the end-cap toroids depending on radial distance to the beamline and ϕ angle.

2.2.2 Inner Detector

A sketch of the Inner Detector of ATLAS can be seen in Figure 2.5. The Inner Detector is enclosed by the solenoid magnet that bends the trajectories of charged particles. The Inner Detector is designed to reconstruct those trajectories and thus to measure the momenta of these particles. It also measures their point of origin to distinguish between particles
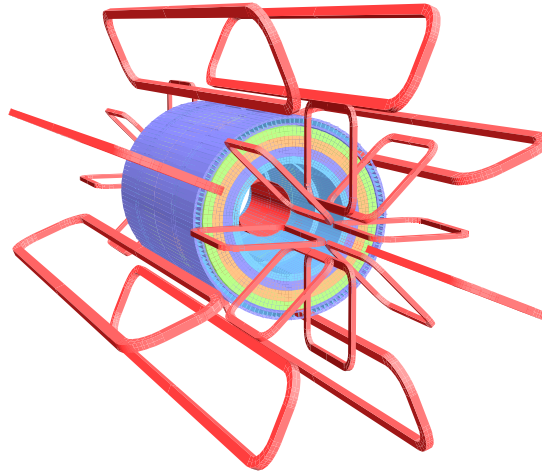
Figure 2.3: *Configuration of the coils of the ATLAS soleoid and toroid magnets. The solenoid iron return yoke in the Tile calorimeter is also shown.*

from the primary hard interaction, from secondary decays, or from additional minimum bias interactions. To achieve this task the Inner Detector is split into three subdetectors, a Pixel detector, a silicon strip detector (SCT), and a straw tube detector (TRT). The Inner Detector measures particles in the rapidity range $|\eta| < 2.5$.

The geometrical configuration and setup of the silicon subdetectors of the Inner Detector, i.e. Pixel and SCT, are outlined below in more detail than the other ATLAS subdetectors. This information will be necessary in Chapter 5 where the alignment of the Pixel and SCT detector is described.

Figure 2.4: *Measurement of the axial and radial components of the ATLAS Inner Detector solenoid field.*

Figure 2.5: *Cut-away view of the ATLAS Inner Detector.*

Pixel

The Pixel detector consists of three cylindrical barrel layers and six end-cap disks, three on each side of the interaction point. The layers and disks are mounted in one rigid frame which is 130 cm long and has 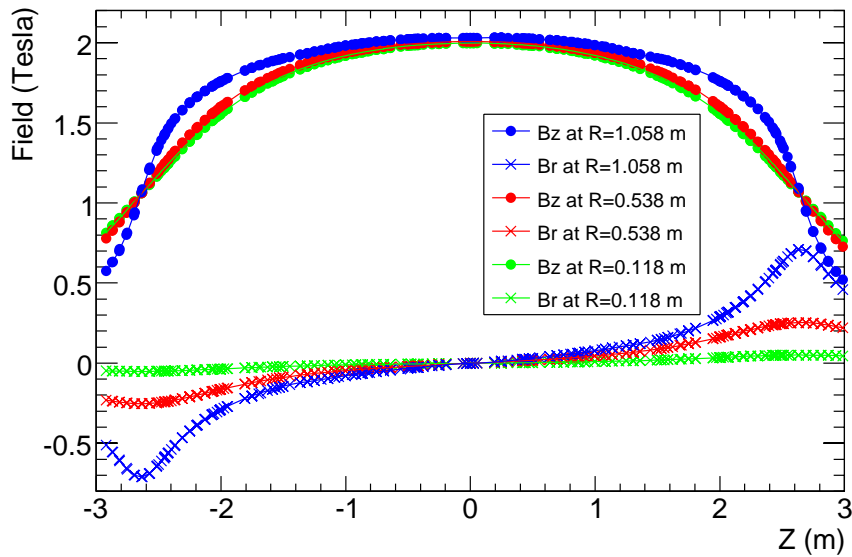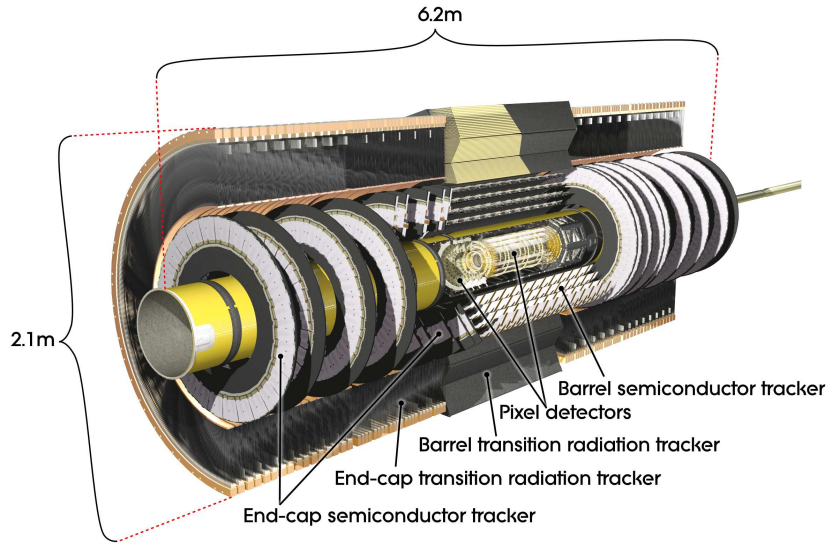an outer radius of 19 cm. The detector elements are 1744 flat silicon modules with identical design. Each module has a size of $19{\times}63\,\mathrm{mm}^2$ and has 47232 readout pixels with a typical pixel size of $50{\times}400\,\mu\mathrm{m}^2$. 1152 of these pixels do not have a separate readout channel but are ganged together with other pixels. Consequently each module has 46080 readout channels. 5284 readout pixels are long pixels with a size of $50{\times}600\,\mu\mathrm{m}^2$. The long pixels lie at the edges of the 16 bump-bonded readout chips of each module.

In the Pixel barrel the modules are mounted on the layers in staves of 13 modules each, along Z. The layer radii, the number of staves and the resulting number of modules per layer are listed in Table 2.2. The staves are tilted by $20°$ with respect to the radial direction from the beamline to overlap with each other (turbine arrangement). In the end-caps there are 48 modules mounted on each disk. The disks are at the Z-positions $|\mathrm{Z}| = \{495\,\mathrm{mm}, 580\,\mathrm{mm}, 650\,\mathrm{mm}\}$.

Pixel barrel configuration			
layer	mean radius	staves	modules
0	50.5 mm	22	286
1	88.5 mm	38	494
2	122.5 mm	52	676

Table 2.2: *Configuration of the Pixel barrel. The mean radius, the number of staves and the number of modules are listed for each of the three Pixel barrel layers.*

The main task of the Pixel detector is to accurately reconstruct the position of primary and secondary vertices.

SCT

The SCT detector consists of a barrel part and two end-caps. The SCT barrel is made up of four layers where in total 2112 SCT barrel modules are mounted. It is 153 cm long. All barrel modules have identical design and a size of $6\times12\,\text{cm}^2$. Each module has two readout sides that are glued back-to-back with a stereo angle of 40 mrad. Each readout side consists of two rectangular silicon sensors with 768 readout strips and a strip pitch of 80 μm. The corresponding readout strips of the two sensors on one side are wire-bonded together so that each side has 768 readout channels. Like in the Pixel barrel, the SCT barrel modules are mounted with a tilt angle to achieve radial overlap. The radii, number of modules and tilt angles for each SCT barrel layer are listed in Table 2.3.

SCT barrel configuration			
layer	mean radius	modules	tilt angle
0	284 mm	384	11.00°
1	355 mm	480	11.00°
2	427 mm	576	11.25°
3	498 mm	672	11.25°

Table 2.3: *Configuration of the SCT barrel. The mean radius, the number of modules and the tilt angle of the modules are listed for the four SCT barrel layers.*

The SCT end-caps consist of nine disks each, where each disk itself consists of up to three rings, an inner, a middle and an outer ring. The SCT end-cap modules reflect this structure as there are different designs for inner, middle and outer modules. The radial coverage of the end-caps requires even four different types of modules with either one silicon sensor (short modules) or two silicon sensors (long module) on each readout side. All inner modules are short modules and all outer modules are long modules. As in the SCT barrel, the readout sides are glued back-to-back with a stereo angle of 40 mrad and 768 readout channels per side. Depending on the radial position the strip pitch varies between 55 μm and 95 μm [39]. The Z-positions, the number of the various module types and the total number of modules for each SCT end-cap disk are listed in Table 2.4.

SCT end-cap configuration					
disk	|Z|	inner modules	middle modules	outer modules	total
0	853.8 mm		40	52	92
1	934.0 mm	40	40	52	132
2	1091.5 mm	40	40	52	132
3	1299.9 mm	40	40	52	132
4	1399.7 mm	40	40	52	132
5	1771.4 mm	40	40	52	132
6	2115.2 mm		40	52	92
7	2505.0 mm		40 *	52	92
8	2720.2 mm			52	52

Table 2.4: *Configuration of the SCT end-caps. The Z-position, the number of the various module types and the total number of modules are listed for the nine SCT end-cap disks. * On disk 7 short middle modules are mounted.*

The SCT provides precision spacepoints for track reconstruction and momentum measurement.

TRT

The outermost of the Inner Detector subdetectors is the TRT. It consists of approximately 300k straw tubes with a diameter of $4\,\mathrm{mm}$ and a hit resolution of $130\,\mu\mathrm{m}$. The strawtubes are filled with a $Xe/CO_2/O_2$ gas mixture and the readout wire anode of each straw is a gold plated tungsten wire. The strawtubes are arranged in 73 layers in the barrel and 160 layers in each end-cap. The layers are interleaved with fibers and foils so that electrons that traverse these emit transition radiation X-rays that are detected by neighboring strawtubes. With the detection of the transition radiation it is possible to discriminate between electrons and hadrons (mostly pions).

A charged particle from the interaction point hits on average 36 strawtubes and so the main task of the TRT is accurate momentum measurement.

Inner Detector readout identifiers

For the alignment of the Pixel and SCT subdetectors described in Chapter 5 it is necessary to unambiguously identify the individual modules and the support structures. This is done via the ATLAS offline readout identifier scheme outlined in [40]. In short, the readout identifier is a number separated by "/" of the following structure:

Identifier = Subsystem / Subdetector / Barrel or Endcap / Layer or Disk / Phi / Eta

The Inner Detector subsystem has the identifier 2. The Pixel subdetector has identifier 1 and the SCT identifier 2. The barrel has the identifier 0, whereas the endcap C has -2 and endcap A has +2. The three Pixel layers and disks are labeled from 0 to 2, the SCT barrel layers are labeled from 0 to 3 and the endcap disks from 0 to 8, with 0 always denoting the innermost layer or disk. The range of the Phi and Eta identifiers depend on the specific barrel layer or endcap disk. To give an example, one of the SCT barrel modules in the third layer (i.e. identifier 2) used for the combined testbeam setup (cf. Section 5.4) has the identifier 2/2/0/2/1/1. On the other hand, the innermost Pixel endcap C disk used for the alignment with cosmic muons (cf. Section 5.5) has the identifier 2/1/-2/0.

2.2.3 Calorimeter

A sketch of the ATLAS calorimeter system can be seen in Figure 2.6. All calorimeters are sampling detectors with a full coverage in ϕ and a coverage of rapidity $|\eta| < 4.9$. The purpose of the calorimeters is the measurement of jet properties, most importantly jet energy, the reconstruction and measurement of electrons and photons and the measurement of an imbalance in transverse energy, namely the measurement of $E_\mathrm{T}^\mathrm{miss}$. To achieve this the calorimeter is split into several subsystems.

The innermost calorimeters are the electromagnetic calorimeters, split into an electromagnetic barrel calorimeter, two electromagnetic end-cap calorimeters (EMEC) and two electromagnetic forward calorimeters (FCal1). They all use liquid argon as active detector
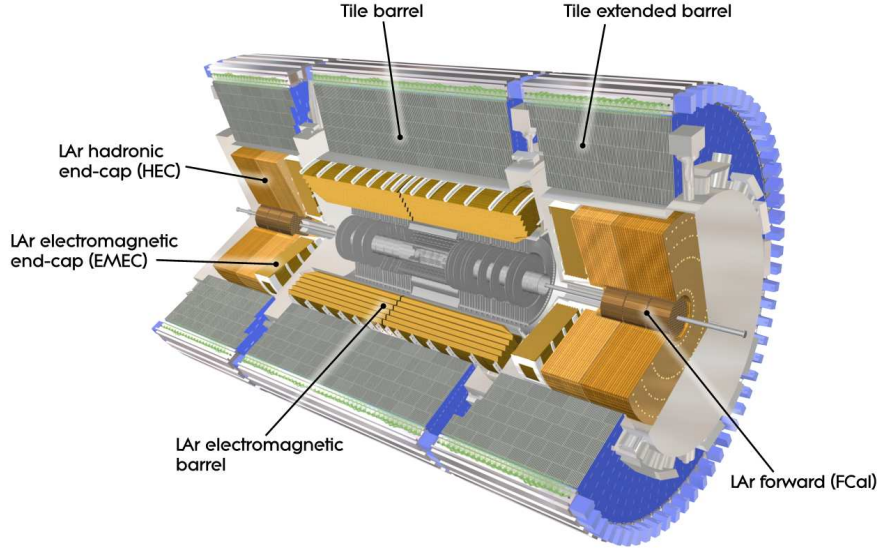
Figure 2.6: *Cut-away view of the ATLAS calorimeter system.*

medium. The electromagnetic barrel calorimeter and the EMEC use accordion-shaped lead absorbers and copper electrodes to achieve full ϕ-coverage without any discontinuities. Their η-coverage is $|\eta| < 3.2$. Within the η-range of the Inner Detector ($|\eta| < 2.5$) the readout cell granularity is $\Delta\eta \times \Delta\phi = 0.025 \times 0.025$ or better to achieve precision measurements of electrons and photons. In the range $2.5 < |\eta| < 3.2$ the cell size is larger ($\Delta\eta \times \Delta\phi = 0.1 \times 0.1$) which is sufficient for jet reconstruction and the measurement of $E_{\mathrm{T}}^{\mathrm{miss}}$. FCal1 uses copper as absorber material and covers an η-range of $3.1 < |\eta| < 4.9$. The FCal1 cell size is $\Delta X \times \Delta Y = 3.0 \times 2.6 \, \mathrm{cm}^2$.

The hadronic calorimeters consist of a Tile barrel, two Tile extended barrel calorimeters, two Hadronic End-cap Calorimeters (HEC) and four hadronic forward calorimeters (FCal2, FCal3). The Tile calorimeters (barrel and extended barrel) cover the range $|\eta| < 1.7$ and use scintillating tiles as active material and steel as absorber. The Tile cell granularity is $\Delta\eta \times \Delta\phi = 0.1 \times 0.1$. The HEC covers the range of $1.5 < |\eta| < 3.2$ with a cell granularity of $\Delta\eta \times \Delta\phi = 0.1 \times 0.1$ for $1.5 < |\eta| < 2.5$ and 0.2×0.2 for $2.5 < |\eta| < 3.2$. The HEC uses liquid argon as active material and copper as absorber material. The hadronic forward calorimeters FCal2 and FCal3 use liquid argon as active and tungsten as absorber material. They cover a range of $3.2 < |\eta| < 4.9$ with cell sizes of $\Delta X \times \Delta Y = 3.3 \times 4.2 \, \mathrm{cm}^2$ for FCal2 and $\Delta X \times \Delta Y = 5.4 \times 4.7 \, \mathrm{cm}^2$ for FCal3.

In total, the calorimeters of ATLAS have approximately 260k readout channels. For the purpose of triggering, these channels are grouped together into 7000 trigger towers with a coarser granularity of $\Delta\eta \times \Delta\phi = 0.1 \times 0.1$ or worse.

2.2.4 Muon system

A sketch of the ATLAS Muon system is shown in Figure 2.7. The Muon system lies furthest from the interaction point and is tightly integrated with the three toroid magnets. The Muon system provides identification of muons because only muons have the penetration

power to pass through the calorimeter without being absorbed. Hadronic leakage from the calorimeter degrades the particle identification slightly. The task of the Muon system is to reconstruct muon tracks and thus to measure muon momenta and to provide muon trigger information. To achieve this the Muon system is split into precision chambers and trigger chambers.
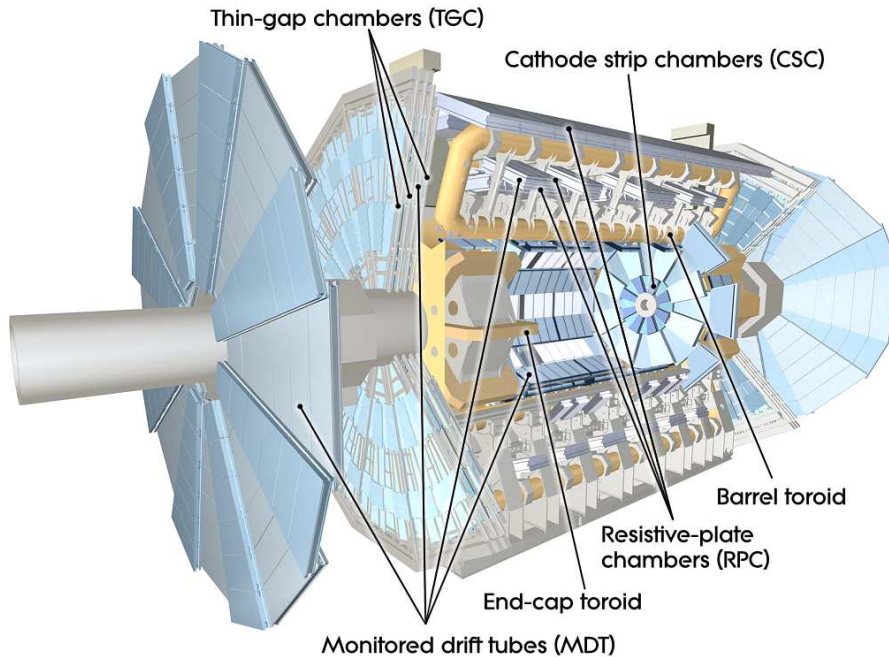

Figure 2.7: *Cut-away view of the ATLAS Muon system.*

The Muon System precision chambers are the MDT and CSC subdetectors. The precision chambers cover the range of $|\eta| < 2.7$. The 1088 MDT chambers and 32 CSC are arranged in three barrel layers and six end-cap wheels, three in each forward direction. The CSC are only used for the innermost ring of the two innermost end-cap wheels ($2.0 < |\eta| < 2.7$). The CSC were designed for counting rates of up to $1000\,\mathrm{Hz/cm^2}$ which will be reached this close to the beam axis. The MDT chambers can only cope with counting rates of up to $150\,\mathrm{Hz/cm^2}$. MDT chambers consist of six or eight layers of drift tubes with a tube diameter of $30\,\mathrm{mm}$. They are filled with a $\mathrm{Ar/CO_2}$ gas mixture and the anode wire is made of tungsten-rhenium. The spatial resolution of each tube is $80\,\mu\mathrm{m}$. The CSC are multiwire proportional chambers where both cathodes are segmented into strips parallel and orthogonal to the anode wires. The cathode strips are used for signal readout whereas the anode wires are not read out. The resolution in the bending plane of muons is $60\,\mu\mathrm{m}$, in the non-bending direction it is $5\,\mathrm{mm}$.

The other part of the Muon system are the trigger chambers RPC and TGC. They are needed to supply the trigger decision logic with fast muon tracking information. RPC are mounted in the barrel part of the Muon system in the range $|\eta| < 1.05$, whereas TGC are used in the end-cap wheels in the range $1.05 < |\eta| < 2.4$. The RPC are mounted directly onto the barrel MDT chambers and together are called a station or superstation. RPCs are gaseous parallel electrode-plate detectors with a gas mixture of $\mathrm{C_2H_2F_4/Iso\text{-}C_4H_{10}/SF_6}$. The TGCs are multiwire proportional chambers with a $\mathrm{CO_2/n\text{-}pentane}$ gas mixture.

Chapter 3

Top quark mass analysis

In the following the details of a top quark mass analysis are outlined. The analysis was performed with the ATLAS software framework Athena release 12.0.6. The analysis software itself can be found in [41]. The analysis was done with Monte Carlo simulated datasets that were produced for a collaboration wide physics performance exercise.

It is a "commissioning style" analysis following a purely cut-based approach [42], ideally suited for the early days of data taking with imperfect detector performance, i.e. no b-tagging of jets is required in this analysis.

3.1 Event signature

The analysis is based on the selection of top quark pairs decaying in the lepton + jets channel (cf. Section 1.2.2). The lepton (i.e. electron or muon) from the leptonic W boson decay is used to trigger the event and is an important selection criterion. The neutrino from this leptonic decay leaves ATLAS undetected and thus gives another event signature: $E_{\mathrm{T}}^{\mathrm{miss}}$. The final event signature used for selection is the jet multiplicity. Both top quarks decay into b quarks and the hadronically decaying W boson into two light quarks. So at least four jets are present in the signal events.

The second step of the analysis is the reconstruction of the top quark mass for the selected events. This is done by using the jets from the hadronically decaying top quark.

3.2 Background processes

The event signature outlined above is mimicked by other physics processes or can be faked by misreconstruction, e.g. due to detector imperfections. Generally, electrons and taus can be reconstructed as jets and thus fake a higher jet multiplicity. Additionally, jets can come from initial state radiation (ISR) or final state radiation (FSR) or from the underlying event, i.e. an additional parton-parton scattering in the same p-p collision. With a small probability ($p_{fake} < 10^{-3}$) calorimeter energy deposits from jets can fake an electron signature and thus jets can be misreconstructed as electrons [43]. $E_{\mathrm{T}}^{\mathrm{miss}}$ can come from semileptonic b or c quark decays or from misreconstruction.

The main background processes are listed below and a short explanation how they can mimic the event signature is given.

- **t$\bar{\text{t}}$ all jets channel**
  These events contain no isolated lepton and no neutrino but have a jet multiplicity of at least six. Jets can fake electrons and $E_{\text{T}}^{\text{miss}}$ can come from semileptonic b quark decays.

- **t$\bar{\text{t}}$ di-lepton channel**
  These events contain two leptons, two neutrinos (so a sizable $E_{\text{T}}^{\text{miss}}$ signature) but have too low jet multiplicity. One of the leptons can fake a jet and an additional jet can come from ISR/FSR or from the underlying event.

- **t$\bar{\text{t}} \to \tau+$ jets**
  In these events the tau can be misreconstructed as an electron or muon. All other signatures are the same as for signal events.

- **Single top: s-channel**
  In the case of a leptonic top quark decay the lepton and $E_{\text{T}}^{\text{miss}}$ signatures are present, but the jet multiplicity of these events is too low. Additional jets can come from ISR/FSR or from the underlying event.

- **Single top: t-channel**
  A leptonic top quark decay can result in the the lepton and $E_{\text{T}}^{\text{miss}}$ signatures but the jet multiplicity is lower than for signal events, but not as low as the jet multiplicity of the s-channel (cf. Figure 1.2). Additional jets can come from ISR/FSR or from the underlying event.

- **Single top: Wt-channel**
  In the case of a leptonic decay of the associated W boson or the W boson from the top quark decay the signature of these events is the same as for signal events, except for a jet multiplicity of only three. An additional jet can come from ISR/FSR or from the underlying event.

- **W+jets production**
  The most prominent background process is W boson production with multiple hard gluon radiation. A leptonic W boson decay gives the lepton and $E_{\text{T}}^{\text{miss}}$ signatures and the jet multiplicity can be high enough.

- **QCD multijet production**
  The background process with the highest cross section. This process can mimic the signal signature if a fake lepton is reconstructed and if $E_{\text{T}}^{\text{miss}}$ is misreconstructed. At the Tevatron experiments this background was not simulated but extracted from collision data, as it is very CPU-intensive to simulate a huge number of events were only a tiny fraction can mimic the signal signature. In ATLAS the same approach is foreseen, so for this analysis there were no simulated datasets available for this background process. Consequently, this process was not taken into account for the studies presented here.

The relative importance of the background processes will be discussed in Section 3.4.

3.3   Monte Carlo datasets

The analysis was performed using Monte Carlo simulated signal and background datasets. The properties of the datasets are outlined in the following and summarized in Table 3.1.

In general Monte Carlo simulation of high-energy particle collisions is split into an evaluation of long-distance pdfs and a simulation of the short-distance hard scattering process followed by parton showering and hadronization. The resulting stable particles are then used as input for the detector simulation, where the detector response to the particles is computed. In addition to the primary hard interaction the underlying event is simulated.

Depending on the dataset the hard interactions were simulated at leading order with the AcerMC [44] or Alpgen [45] software or at next-to-leading order with MC@NLO [46, 47]. For parton showers and hadronization the programs Pythia [48] and Herwig [49] were used. The underlying event was simulated internally within the Pythia program or externally for Herwig with the program Jimmy [50]. The detector simulation for all datasets was done with Geant4 [51]. The detector simulation used for all datasets suffered from a misconfiguration of the response of the liquid argon calorimeters (cf. Section 2.2.3) that resulted in a underestimation of all reconstructed energies. It was decided by the ATLAS collaboration to not redo these centrally produced datasets and to use them for the physics performance exercise. At the time when the misconfiguration was discovered, a reprocessing of the datasets would have resulted in a six month delay of the physics performance exercise. The input parameter of the generator software for top quark mass was $175\,\mathrm{GeV}$ and for the W boson mass $80.419\,\mathrm{GeV}$.

The top quark pair production datasets were generated and simulated without any selection cuts. The single top quark production datasets were simulated with a cut at generator level that forced the W boson from the top quark decay to decay leptonically. For the single top quark Wt-channel either the associated or the decay W boson were forced to decay leptonically. Thus no all jets or di-leptonic decays were simulated for the Wt-channel.

The W+jets datasets were simulated such that in each dataset all events had a fixed number of additional partons. This was achieved by applying the MLM algorithm to match the hard scattering and the parton showering calculations to yield the required number of partons [52]. The matching parameters for partons in the MLM algorithm were $p_{\mathrm{T}} = 20\,\mathrm{GeV}$ and a minimal distance between partons of $\Delta\mathrm{R} = 0.3$. The resulting W+jets datasets were further filtered at Monte Carlo truth level (i.e. before the detector simulation and reconstruction) to contain at least 3 jets with $p_{\mathrm{T}} > 30\,\mathrm{GeV}^*$. This p_{T} requirement is clearly visible in Figures 3.1 and 3.3.

To normalize the cross sections of all simulated datasets to their respective next-to-leading order theoretical cross sections, K-factors are used to scale the simulated leading order cross section to its next-to-leading order value. The details for each dataset, as well as the simulated luminosity, are shown in Table 3.1

---

*Calorimeter clusters from electrons are used in ATLAS jet reconstruction and are included in the input object list for jet algorithms. Also at Monte Carlo truth level electrons contribute to jets.

process	hard scattering	showering hadronization underlying event	σ_{prod} [pb]	K-factor	simulated luminosity [pb^{-1}]
$t\bar{t}$ di-lepton and lepton + jets channel	MC@NLO	Herwig + Jimmy	450	1.0	962
$t\bar{t}$ all jets channel	MC@NLO	Herwig + Jimmy	380	1.0	173
Single top s-channel	AcerMC	Pythia	2.3	1.5	3333
Single top t-channel	AcerMC	Pythia	81.3	0.98	146
Single top Wt-channel	AcerMC	Pythia	25.5	1.14	438
W $\rightarrow e\nu$ + 2 jets	Alpgen	Herwig + Jimmy	214	1.15	89
W $\rightarrow e\nu$ + 3 jets	Alpgen	Herwig + Jimmy	124	1.15	78
W $\rightarrow e\nu$ + 4 jets	Alpgen	Herwig + Jimmy	54	1.15	96
W $\rightarrow e\nu$ + 5 jets	Alpgen	Herwig + Jimmy	22	1.15	195
W $\rightarrow \mu\nu$ + 2 jets	Alpgen	Herwig + Jimmy	16	1.15	176
W $\rightarrow \mu\nu$ + 3 jets	Alpgen	Herwig + Jimmy	65	1.15	154
W $\rightarrow \mu\nu$ + 4 jets	Alpgen	Herwig + Jimmy	36	1.15	77
W $\rightarrow \mu\nu$ + 5 jets	Alpgen	Herwig + Jimmy	20	1.15	206
W $\rightarrow \tau\nu$ + 2 jets	Alpgen	Herwig + Jimmy	88	1.15	203
W $\rightarrow \tau\nu$ + 3 jets	Alpgen	Herwig + Jimmy	87	1.15	129
W $\rightarrow \tau\nu$ + 4 jets	Alpgen	Herwig + Jimmy	46	1.15	94
W $\rightarrow \tau\nu$ + 5 jets	Alpgen	Herwig + Jimmy	21	1.15	0*

Table 3.1: *Monte Carlo datasets used for the top quark mass analysis. For each dataset the simulated physics process and the Monte Carlo program used for simulation are listed. The production cross sections, the K-factors and the simulated luminosities are listed as well. (*)This dataset was missing and not available available for the analysis.*

3.4   Event selection cuts

As stated in Section 3.1 the event selection is based on the presence of an isolated lepton, i.e. an object reconstructed by the electron or muon reconstruction algorithms, E_T^{miss} and jet multiplicity. The exact definition of these high level physics objects is outlined below.

- **Electrons**
  Electron candidates were reconstructed by the egamma algorithm [53] with a tight electron definition and had to fulfill the following criteria:

  - $|\eta| < 2.5$
  - $p_T > 20\,\text{GeV}$

Additionally, electron candidates in the range $1.37 < |\eta| < 1.52$ were vetoed. This is the crack region between the electro-magnetic barrel and end-cap calorimeters. The electron reconstruction efficiency in this η-range suffered from a software defect in Athena release 12.0.6. No isolation criterion was imposed on the electron candidates because of a software defect in the calculation of the isolation energy. These software defects were corrected in later Athena releases. Mainly for reasons of repeatability, the ATLAS collaboration decided to use an unpatched release 12.0.6 for the physics performance exercise and to use workarounds like the veto of certain η-regions to minimize the impact of known software defects. To be able to participate in the physics performance exercise and to produce comparable results this approach was adopted for the analysis presented here. The p_T spectra of the electrons for the signal and background Monte Carlo datasets and the fraction of events where a certain number of electrons fulfill the selection criteria are shown in Figure 3.1.
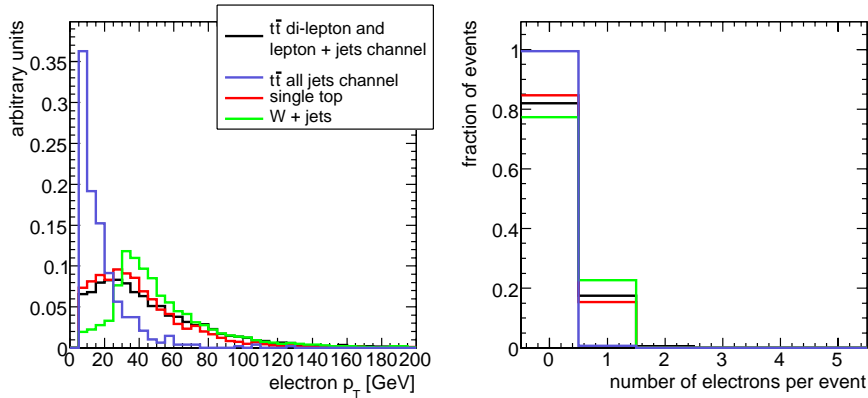

Figure 3.1: *The left Figure shows the transverse momentum of electrons for the different Monte Carlo datasets. The electrons are within $|\eta| < 2.5$ and fulfill the tight electron definition. The right Figure shows the number of electrons per event after the additional p_T cut at 20 GeV.*

The electron p_T spectra from datasets that contain a leptonic W boson decay are harder than the p_T spectrum of the electrons from the $t\bar{t}$ all jets channel. The signal dataset and the single top datasets have comparable p_T spectra. The W+jets datasets have a clearly visible peak at 30 GeV that is a feature of the pre-filtering

of these datasets during simulation. A requirement of one electron per event can clearly discriminate the signal dataset from the $t\bar{t}$ all jets channel dataset. It cannot distinguish between the signal dataset and background datasets that contain a leptonic W boson decay.

- **Muons**
  Muon candidates were reconstructed by the Staco algorithm [54]. This is an algorithm that uses a statistical combination of Inner Detector and Muon System information for the muon reconstruction. Muon candidates had to fulfill the following criteria:

  - $|\eta| < 2.5$
  - $p_\mathrm{T} > 20\,\mathrm{GeV}$

Additionally, the muon candidates had to fulfill an isolation requirement. The sum of all energy deposits in the calorimeter cells in a cone of $\Delta \mathrm{R} < 0.2$ around the muon track had to be less than $6\,\mathrm{GeV}$. The p_T spectra of the muons for the signal and background Monte Carlo datasets and the fraction of events where a certain number of muons fulfill the selection criteria are shown in Figure 3.2.
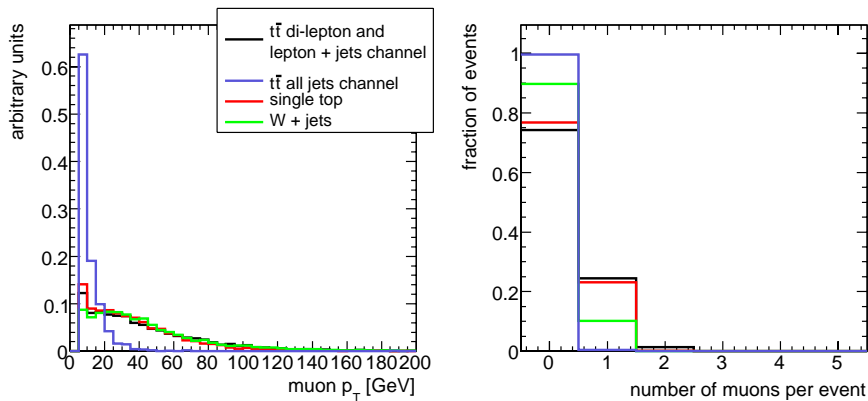

Figure 3.2: *The left Figure shows the transverse momentum of muons for the different Monte Carlo datasets. The muons are within $|\eta| < 2.5$ and fulfill the isolation requirement. The right Figure shows the number of muons per event after the additional p_T cut at $20\,\mathrm{GeV}$.*

The muon p_T spectra from the signal dataset and from the single top and W+jets datasets are very similar, as can be expected because the muons all come from W boson decays. The muon p_T spectrum from the W+jets datasets shows no peak structure like the electron p_T distribution, because in the pre-filtering of these datasets muons were not counted towards the filter requirement. A requirement of one muon per event can clearly discriminate the signal dataset from the $t\bar{t}$ all jets channel dataset. It cannot distinguish between the signal dataset and background datasets that contain a leptonic W boson decay.

- **Jets**
  Jet candidates were reconstructed from topological calorimeter clusters [55] with an iterative, seeded, fixed-size cone algorithm with $\mathrm{R_{cone}} = 0.4$ [56]. The hadronic

calibration of the jet candidates was done with a cell signal weighting procedure called H1-weighting [57]. Jet candidates had to fulfill the following criteria:

- $|\eta| < 2.5$
- $p_\mathrm{T} > 40\,\mathrm{GeV}$

Additionally, jet candidates were removed if the jet was closer to a lepton (as defined above) than $\Delta\mathrm{R} < 0.4$. The reason for this is that electron and jet reconstruction are not exclusive. The energy deposits in the electromagnetic calorimeter are used for electron reconstruction and for jet building. So jets were removed to avoid double-counting of the same energy deposit. The jets too close to muons were also removed to treat both lepton flavors on an equal footing. The p_T spectra of the jets for the signal and background Monte Carlo datasets and the fraction of events where a certain number of jets fulfill the selection criteria are shown in Figure 3.3.
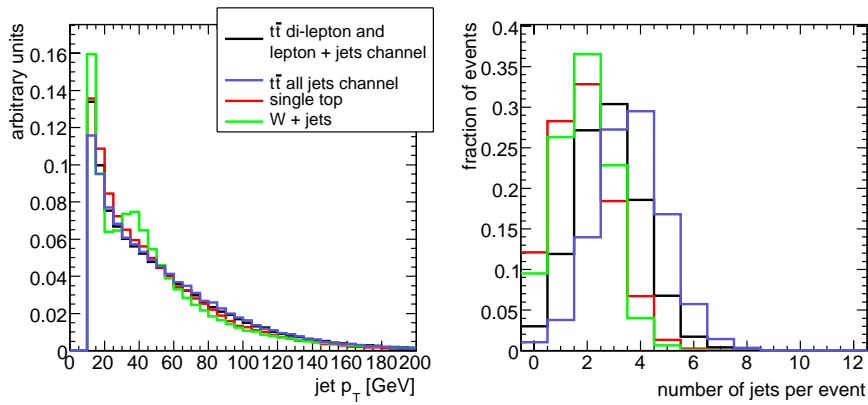

Figure 3.3: *The left Figure shows the transverse momentum of jets for the different Monte Carlo datasets. The jets are within $|\eta| < 2.5$. The right Figure shows the number of jets per event after the additional p_T cut at $40\,\mathrm{GeV}$.*

The peak that is visible in the jet p_T spectrum of the W+jets datasets is a feature of the pre-filtering of these datasets. It is apparent that a required jet multiplicity of at least four jets per event can discriminate between the signal dataset and the $t\bar{t}$ all jets channel dataset on the one hand and the single top and W+jets datasets on the other hand.

- $\mathbf{E}_\mathrm{T}^\mathrm{miss}$
  Missing transverse energy was calculated as the vector sum of the transverse energy coming from calorimeter cells, muons and correction factors for energy loss in material in front of the calorimeter. The result of this calculation is made available in the standard ATLAS reconstruction variable MET_EtMissRefFinal [58].

  The $E_\mathrm{T}^\mathrm{miss}$ spectra for the signal and background Monte Carlo datasets and the fraction of events that fulfill a cut of $E_\mathrm{T}^\mathrm{miss} > 20\,\mathrm{GeV}$ are shown in Figure 3.4.

The signal dataset has the hardest $E_\mathrm{T}^\mathrm{miss}$ spectrum because it contains the $t\bar{t}$ di-lepton channel as well as the $t\bar{t}$ lepton + jets channels. In the di-lepton channel events two neutrinos from the leptonic W boson decays escape ATLAS undetected and thus produce
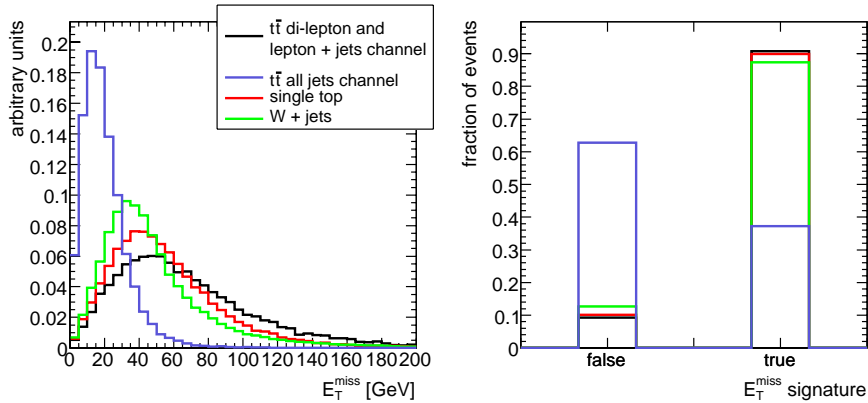
Figure 3.4: *The left Figure shows E_T^{miss} for the different Monte Carlo datasets. The right Figure shows the fraction of events that fulfill the requirement $E_T^{miss} > 20$ GeV.*

a sizable E_T^{miss} signature. The requirement of an E_T^{miss} signature can distinguish between datasets with leptonic W boson decays and datasets without.

In the following it is implicit that all high level physics objects meet the selection criteria outlined above. For event selection the following cuts are imposed on the high level physics objects:

- exactly one lepton

- at least 4 jets.

- $E_T^{miss} > 20$ GeV

A detailed cut-flow is shown in Table 3.2 for the signal processes separated into the electron and muon channel and the different background processes. The number of initial events and the number of events after subsequent application of the selection cuts outlined above are shown.

Scaled to an integrated luminosity of $1\,\text{fb}^{-1}$, the signal dataset (cf. Section 3.3) contains 450k events, 119.5k events each for the three lepton + jets channels and 91.5k di-lepton events. With the selection cuts outlined above a total of 10456 e + jets events and 16945 μ + jets events are selected, corresponding to a selection efficiency of $\epsilon_e = 8.7\%$ for the e + jets channel and of $\epsilon_\mu = 14.2\%$ for the μ + jets channel.

The background processes without a lepton signature, i.e. the $t\bar{t}$ all jets channel and the $W \rightarrow \tau\nu$ + jets process are suppressed very efficiently with these selection cuts. A significant background contribution comes from the $t\bar{t}$ τ + jets channel. In the next Section the selected events will be used to measure the hadronic top quark mass. As the hadronic top quark decay in the $t\bar{t}$ τ + jets channel is similar to the other two $t\bar{t}$ lepton + jets channels, these events can still yield a correct estimate of the top quark mass. The selected $t\bar{t}$ di-lepton and single top t-channel events on the other hand do not have a hadronic top quark decay, so they are a true background for the top quark mass measurement. Some of the single top Wt-channel events have a leptonic decay of the associated W boson and thus a hadronic top quark decay. These events can still yield a correct estimate of the top quark mass.

| process | number of events | | | | selection |
	initial	lepton cut	jet cut	$E_\mathrm{T}^\mathrm{miss}$ cut	rate
$t\bar{t}$ e + jets channel	119500	54306	11550	10456	8.7%
$t\bar{t}$ μ + jets channel	119500	84083	18741	16945	14.2%
$t\bar{t}$ τ + jets channel	119500	12108	2590	2396	2.0%
$t\bar{t}$ di-lepton channel	91500	58412	4165	3941	4.3%
$t\bar{t}$ all jets channel	380000	4103	1427	716	0.2%
Single top s-channel	3450	1230	17	15	0.4%
Single top t-channel	79670	30613	1110	1022	1.3%
Single top Wt-channel	29070	12533	948	823	2.8%
W $\rightarrow$ $e\nu$ + jets	476099	181179	2527	2433	0.5%
W $\rightarrow$ $\mu\nu$ + jets	157568	85869	4450	4055	2.6%
W $\rightarrow$ $\tau\nu$ + jets	254149	15792	241	205	0.1%

Table 3.2: *Event selection cut-flow for the signal and background processes. All event numbers are scaled to correspond to 1 fb^{-1} of integrated luminosity. The cuts are applied sequentially, so that the numbers of events need to be read from left to right. For each process the column "$E_\mathrm{T}^\mathrm{miss}$ cut" corresponds to the final number of events that pass all selection cuts. The last column lists the selection rate for each process.*

3.5　Hadronic top quark mass reconstrucion

For each of the selected events a reconstruction of the hadronic top quark is attempted. From the jet list those three jets are selected whose added 4-vectors yield the highest transverse momentum p_T. The 4-vector sum of these three jets is then interpreted as the 4-vector of the hadronically decaying top quark. The invariant mass spectrum of the top quark candidates reconstructed in this fashion is shown in Figure 3.5.

In this Monte Carlo study the datasets described in Section 3.3 were used and their contributions to the invariant mass spectrum weighted according to production cross sections and K-factors. The luminosity corresponds to 1 fb^{-1}.

From the invariant mass spectrum the top quark mass is extracted in the following manner: The sum of a Gaussian and a polynomial function of 4th degree is fitted to the distribution. The polynomial function describes the background from wrong jet combinations and from physics background processes [42] and is parameterized via Chebychev polynomials [59]. The mean value of the Gaussian is interpreted as the reconstructed top quark mass. The fit error of the mean value is interpreted as the statistical uncertainty of the top quark mass. For this study the fit range and the starting parameters of the fit were chosen as follows

- Normalization factor of Gaussian: maximum bin content of signal+background histogram

- Mean of Gaussian: bin center of bin with maximum content in signal+background histogram
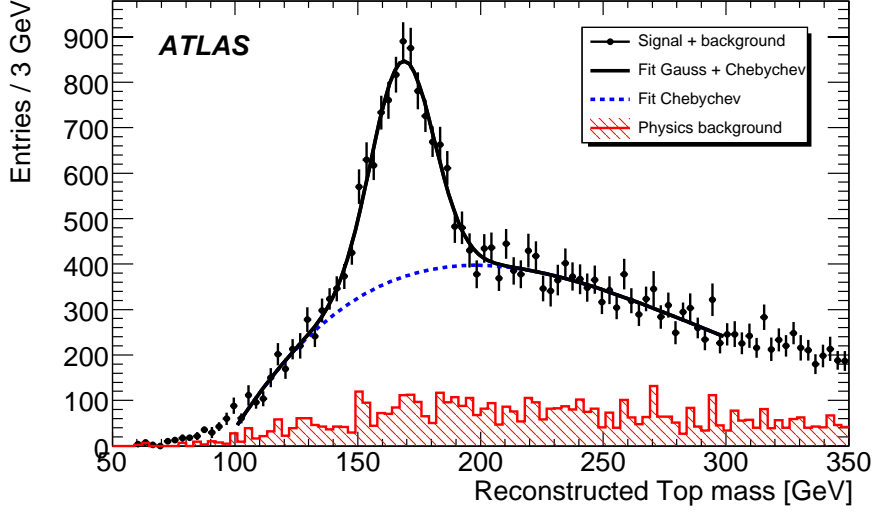
- Width of Gaussian: 12 GeV

Figure 3.5: *Invariant tri-jet mass as an estimate of the hadronically decaying top quark mass in the selected events. The luminosity used corresponds to $1\,fb^{-1}$ of signal and background events. The datapoints for signal and background events are shown in black. The distribution coming from background datasets only is shown in red.*

- Chebychev polynomial: constant function at $0.5 \times$ maximum bin content of signal+background histogram

- Fit range: $(100 - 300)\,\mathrm{GeV}$

The Gaussian fit functions was parameterized as follows [59]:

$$f_{Gauss}(x) = c \cdot e^{-0.5 \cdot \left(\frac{x-\mu}{\sigma}\right)^2} \tag{3.1}$$

The Chebychev polynomial fit functions was parameterized as follows [59]:

$$f_{Chebychev}(x) = \sum_{n=0}^{4} a_n \cdot T_n(x) \tag{3.2}$$

where $T_n(x)$ denotes a Chebychev polynomial of degree n defined as

$$\begin{aligned}
T_0(x) &= 1, \\
T_1(x) &= t(x), \\
T_n(x) &= 2 \cdot t(x) \cdot T_{n-1}(x) - T_{n-2}(x),
\end{aligned}$$

$$\begin{aligned}
\text{with} \quad t(x) &= a \cdot x - b, \\
\text{with} \quad a &= 2/(\text{fit range}_{\max} - \text{fit range}_{\min}) \\
\text{and} \quad b &= 1 - a \cdot \text{fit range}_{\max} \tag{3.3}
\end{aligned}$$

The starting parameters for the fit and the final fit values are listed in Tables 3.3 and 3.4 for the Gaussian and the Chebychev polynomial function respectively. The fit results are discussed in Section 3.8.

	Gaussian fit function		
	μ	σ	c
starting parameters	168.5	12	889.916
final fit parameters	168.23 ± 0.54	12.77 ± 0.64	475 ± 20

Table 3.3: *Fit parameters for the Gaussian fit function. Listed are the starting parameters and the final fit parameters.*

	Chebychev polynomial fit function				
	a_0	a_1	a_2	a_3	a_4
starting parameters	444.958	0	0	0	0
final fit parameters	268 ± 5.0	73.4 ± 5.7	-129.1 ± 6.9	27.6 ± 7.5	-0.86 ± 5.8

Table 3.4: *Fit parameters for the Chebychev polynomial fit function. Listed are the starting parameters and the final fit parameters.*

3.6   W boson mass reconstruction

Two of the three jets comprising the top quark should come from light quarks that come from the hadronic W boson decay. By assigning the correct two jets among the three the W boson can be reconstructed. In the absence of b-tagging it is a priori not clear which of the three possible di-jet combinations is the correct one. Within the scope of this study three methods were used for W boson reconstruction:

- Selecting the two jets that are closest in ΔR. (**ΔR method**)

- Selecting the two jets that yield the highest p_T object. (**highest p_T method**)

- Selecting the two jets whose invariant mass is closest to the the PDG-value of $m_W = 80.398\,\text{GeV}$ [27]. (**Δm method**)

The invariant mass spectra of the W boson candidates reconstructed with these three methods can be seen in Figures 3.6 - 3.8, respectively. From these spectra the W boson mass can be determined the same way as the top quark mass by fitting a Gaussian and a Chebychev polynomial function of 4th degree. The choice of start parameters for the fit were obtained in the same manner as for the top quark mass. The fit ranges were set to (50 - 150) GeV. The fit results are shown in Table 3.6.

With the information from the reconstructed W boson a purification of the top quark candidates can be done to reduce the presence of combinatorial and physics background. Only those top quark candidates are retained where the reconstructed W boson mass is within a mass window of $\pm\,20\,\text{GeV}$ around the PDG value [27]. The invariant mass spectra of the refined selection of top quark candidates are shown in Figures 3.9 - 3.11 for the three methods of W boson mass reconstruction, respectively. The fit results for the top quark masses extracted from these spectra are shown in Table 3.6 as well.
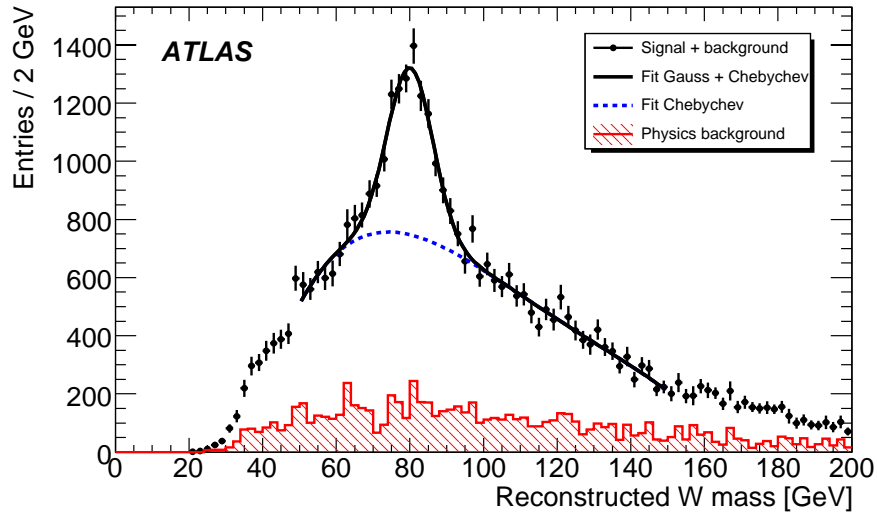
Figure 3.6: *Invariant di-jet mass as an estimate of the hadronically decaying W boson mass in the selected events. The two jets were selected with the ΔR method. The datapoints for signal and background events are shown in black. The distribution coming from background datasets only is shown in red.*
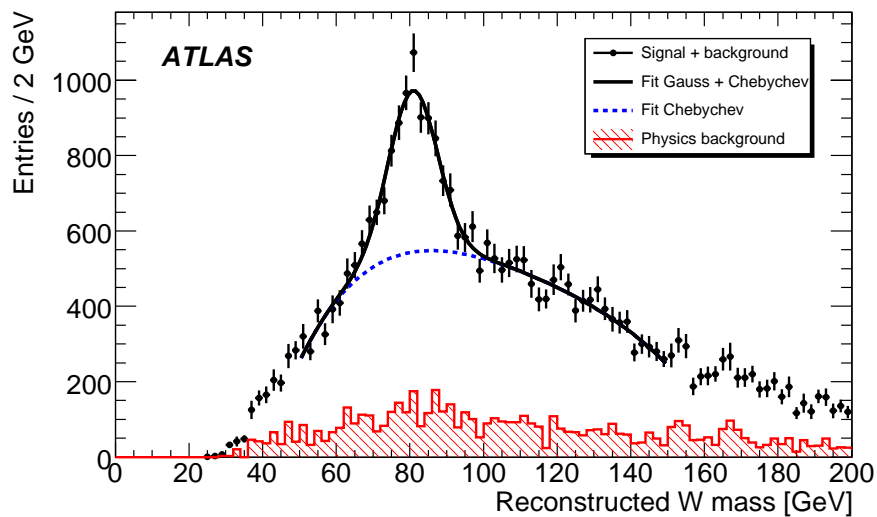

Figure 3.7: *Same as Figure 3.6, but the two jets were selected with the highest p_T method.*
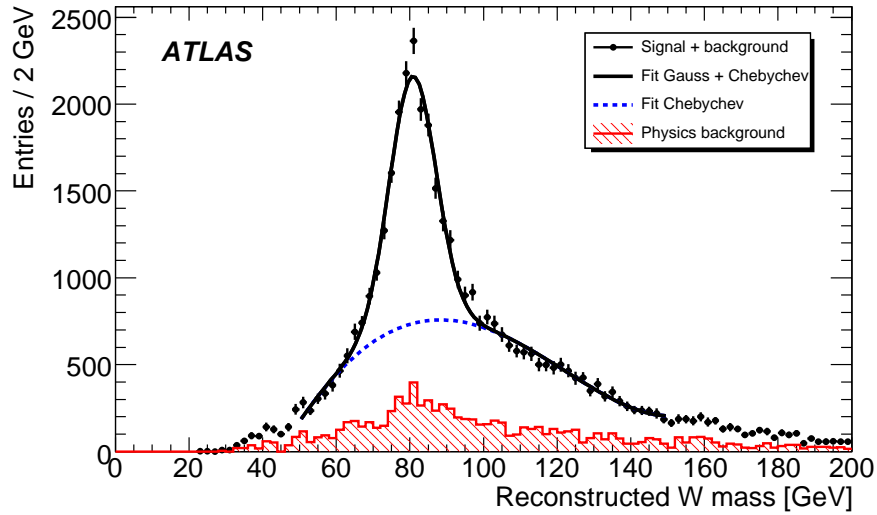
Figure 3.8: *Same as Figure 3.6, but the two jets were selected with the Δm method.*
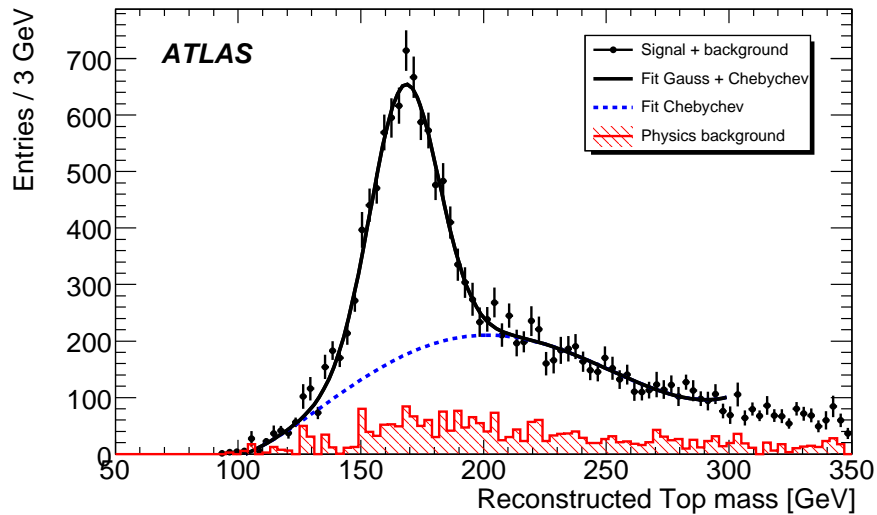

Figure 3.9: *Same as Figure 3.5 for those events that fulfill the requirement $|m_W(\text{reconstructed}) - \text{m}_W(\text{PDG})| < 20\,\text{GeV}$. The W boson candidates are selected with the ΔR method.*
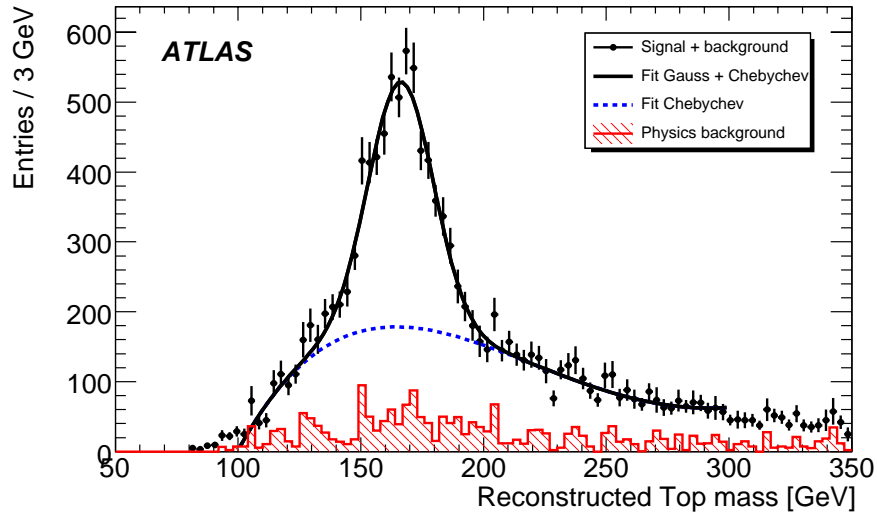
Figure 3.10: *Same as Figure 3.9, but with the highest p_{T} method used for W boson reconstruction.*
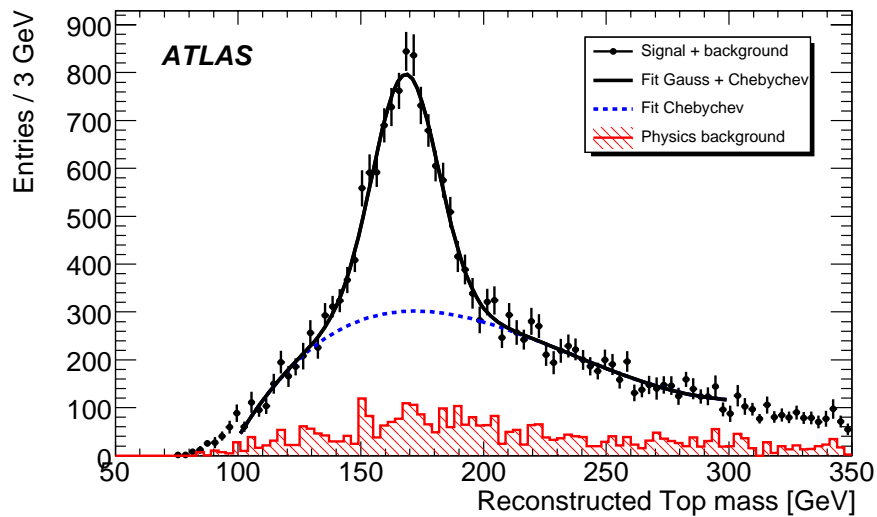

Figure 3.11: *Same as Figure 3.9, but with the Δm method used for W boson reconstruction.*

3.7   Top quark selection purity

To quantify the purity of the top quark selection the number of correctly reconstructed events and the number of wrongly reconstructed events needs to be estimated. The number of events under the fitted Gaussian is interpreted as the number of correctly reconstructed events, whereas the number of events under the Chebychev polynomial function is interpreted as the number of wrongly reconstructed events, stemming from physics background and wrong jet association. For the top quarks reconstructed without any W boson mass requirement the number of events under the Gaussian in a range of $\mu \pm \sigma$ (cf. Table 3.3) is 10369, whereas the number of events under the Chebychev polynomial function in the same range is 9426. This results in a purity of $\frac{S}{S+B} = 52\%$. For the top quarks reconstructed with a W boson mass requirement the purity rises up to 70% for the ΔR method.

The overall number of selected events from physics background processes is only 22% of the number of selected signal events. In the region around the mass peak where the signal events accumulate, but the physics background stays flat, this number drops to 12%. The purity and physics background contamination numbers are summarized in Table 3.5.

	Purity $\frac{S}{S+B}$	background contamination	
		total	signal region
Top without m_W requirement	52%	22%	12%
Top with m_W req. (ΔR method)	70%	18%	10%
Top with m_W req. (highest p_T method)	63%	19%	12%
Top with m_W req. (Δm method)	58%	19%	12%

Table 3.5: *Purity and physics background contamination of the top quark mass analysis with and without a W boson mass requirement.*

3.8   Results of hadronic top quark mass analysis

The results of the "commissioning style" top quark mass analysis described in the previous Sections are presented here. The fit results of the hadronic top quark and W boson mass reconstruction as described in Sections 3.5 and 3.6 are listed in Table 3.6. The mean values of the fitted Gaussians are interpreted as the reconstructed masses. As stated in Section 3.3, the input top quark mass of the simulated datasets was 175 GeV and the input W boson mass was 80.419 GeV.

The reconstructed W boson mass compares very well with the input W boson mass. This in turn means that the main systematic for data events, i.e. the light jet energy scale, is well calibrated for the Monte Carlo datasets that were used. This is not surprising, considering that exactly this light jet energy scale is calibrated in the H1 weighting procedure. On the other hand the reconstructed top quark mass is systematically lower than the input top quark mass. This is an indication that the b jet energy scale is too low. The reconstructed top quark mass is only 96% of the input mass. Under the assumption that this effect comes in equal parts from the light jet and the b jet energy scale and using a perfect light jet energy scale, the b jet energy scale is around 92%.

The light jet energy scale can be measured and calibrated, e.g. with the known W boson mass. Independent measurements of the b jet energy scale and the top quark mass are

| | fit parameters of Gaussian [GeV] | |
	mean(μ) $\pm$ fit error	width(σ) $\pm$ fit error
m_t without m_W requirement	168.23 $\pm$ 0.54	12.77 $\pm$ 0.64
m_t with m_W req. (ΔR method)	167.82 $\pm$ 0.42	13.82 $\pm$ 0.50
m_t with m_W req. (highest p_T method)	166.37 $\pm$ 0.54	13.20 $\pm$ 0.66
m_t with m_W req. (Δm method)	168.26 $\pm$ 0.50	13.39 $\pm$ 0.60
m_W (ΔR method)	80.09 $\pm$ 0.34	6.13 $\pm$ 0.50
m_W (highest p_T method)	80.80 $\pm$ 0.44	6.70 $\pm$ 0.66
m_W (Δm method)	80.74 $\pm$ 0.17	6.36 $\pm$ 0.25

Table 3.6: *Fit results of the mass analyses for the W boson mass and the top quark mass with and without a W boson mass cut.*

difficult and have not been attempted so far at the Tevatron experiments. An independent measurement of m_t and the b jet energy scale is proposed in [60] but this would require very good b-tagging performance, something which is not feasible for a commissioning style top quark mass measurement at ATLAS.

Already with this commissioning style analysis it is possible to efficiently suppress the $t\bar{t}$ τ + jets, di-lepton and all jets channels and the single top and the W + jets processes. The real background rates can only be estimated with data, especially for QCD multi-jet production which was not considered in this analysis. QCD multijet production can become a major source of background if the rate of fake lepton reconstruction is high ($p_{fake} > 10^{-3}$). It is likely that this will be the case during the commissioning phase of ATLAS, i.e. during the early data taking. Unfortunately the initial detector performance cannot be reliably estimated with simulated data but needs to be quantified with collision data.

With the present set of physics background processes considered, the biggest background for the top quark mass determination comes from the signal dataset itself, namely from the wrong assignment of jets. The rate of wrong jet assignment can be greatly suppressed with b-tagging. The background from other physics processes can be suppressed with b-tagging as well.

Chapter 4

Systematic effects

In the following Chapter, the robustness and behavior of the analysis described in Chapter 3 under different systematic variations is investigated. Firstly the kinematics of the jet selection is studied and the impact on the hadronic mass fits is evaluated. Secondly the impact of the underlying jet definition is examined. To quantify this effect two distinct types of jet finding algorithms and a wide range of steering parameters were used to produce alternative lists of jet candidates as input for the analysis. Finally the impact of the most dominant systematic uncertainty, namely the jet energy scale uncertainty, is evaluated for the different hadronic mass fits and jet definitions.

4.1 Jet selection cuts

The selection cuts to identify jet candidates as presented in Section 3.4 directly restrict the kinematic phase space of the reconstructed hadronic top quarks. To study the effects of different jet selection cuts on the reconstructed hadronic top quark mass the analysis was repeated with two different sets of jet selection cuts.

The first set of alternative cuts is very similar to the original set of cuts and requires at least four jets with $p_\mathrm{T} > 40\,\mathrm{GeV}$. All additional jets in an event only need to fulfill a looser p_T requirement, namely $p_\mathrm{T} > 20\,\mathrm{GeV}$. This set of alternative cuts results in exactly the same event selection but the three jets selected in each event to reconstruct the hadronic top quark can be different. This alternative set of cuts is called **selection Set 1**. The invariant mass spectrum of the top quark candidates reconstructed in this fashion is shown in Figure 4.1. The corresponding invariant mass spectrum of the W boson candidates reconstructed with the ΔR method can be seen in Figure 4.2. The fit results of all hadronic masses reconstructed with selection Set 1 are listed in Table 4.1. The corresponding signal purities and background contaminations (as defined in Section 3.7) are listed in Table 4.2.

The standard analysis and the analysis with selection Set 1 select 43k events. With selection Set 1 in 12171 of these events one of the three top quark jets is replaced with a jet of $p_\mathrm{T} < 40\,\mathrm{GeV}$ and in 560 events even two jets are replaced. In no event all three jets are replaced.
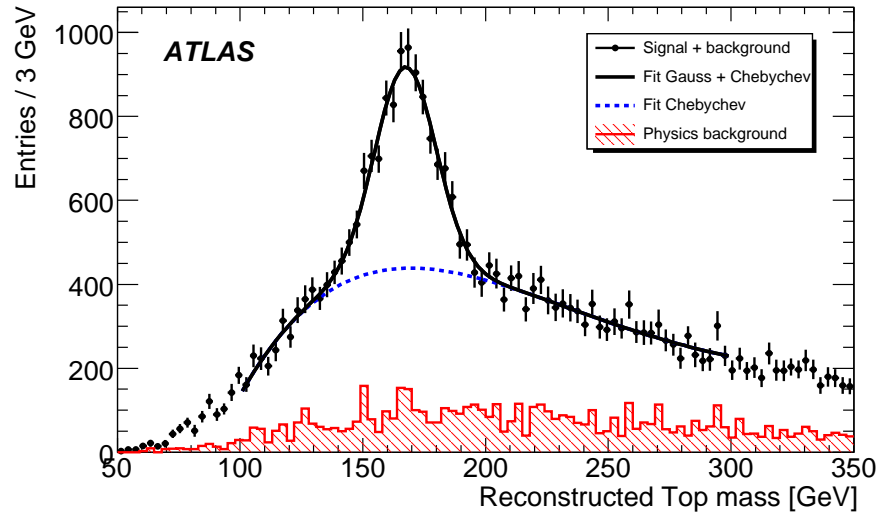
Figure 4.1: *Same as Figure 3.5, but for those events that fulfill selection Set 1.*
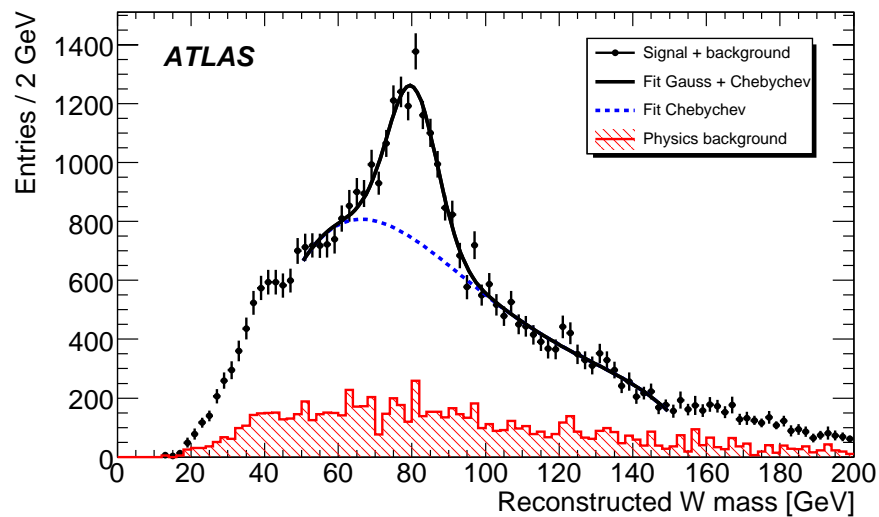

Figure 4.2: *Same as Figure 3.6, but for those events that fulfill selection Set 1.*

	fit parameters of Gaussian [GeV]	
	mean(μ) $\pm$ fit error	width(σ) $\pm$ fit error
m_t without m_W requirement	167.40 $\pm$ 0.56	12.40 $\pm$ 0.71
m_t with m_W req. (ΔR method)	166.87 $\pm$ 0.49	14.62 $\pm$ 0.63
m_t with m_W req. (highest p_T method)	165.90 $\pm$ 0.63	12.75 $\pm$ 0.77
m_t with m_W req. (Δm method)	167.30 $\pm$ 0.54	13.66 $\pm$ 0.69
m_W (ΔR method)	80.18 $\pm$ 0.42	6.65 $\pm$ 0.64
m_W (highest p_T method)	81.09 $\pm$ 0.45	6.79 $\pm$ 0.67
m_W (Δm method)	80.58 $\pm$ 0.17	6.47 $\pm$ 0.25

Table 4.1: *Fit results of the mass analysis for the top quark and the W boson mass. The events were selected with selection Set 1.*

	Purity	background contamination	
	$\frac{S}{S+B}$	total	signal region
Top without m_W requirement	48%	23%	13%
Top with m_W req. (ΔR method)	68%	18%	9%
Top with m_W req. (highest p_T method)	56%	19%	11%
Top with m_W req. (Δm method)	56%	20%	12%

Table 4.2: *Purity and physics background contamination of the top quark mass analysis. The events were selected with selection Set 1.*

The other set of cuts requires only three jets with $p_\mathrm{T} > 40\,\mathrm{GeV}$ and at least one additional jet with $p_\mathrm{T} > 20\,\mathrm{GeV}$. This set of softer cuts is called **selection Set 2**. It selects the same events as the standard analysis plus additional events that now pass the softer jet requirement. In addition, for the identical events the three jets selected to reconstruct the hadronic top quark can be different. The invariant mass spectrum of the top quark candidates reconstructed in this fashion is shown in Figure 4.3. The corresponding invariant mass spectrum of the W boson candidates reconstructed with the ΔR method can be seen in Figure 4.4. The fit results of all hadronic masses reconstructed with selection Set 2 are listed in Table 4.3. The corresponding signal purities and background contaminations are listed in Table 4.4.

The analysis with selection Set 2 selects 55k additional events. The invariant mass spectrum of the top quark candidates reconstructed with these additional events is shown in Figure 4.5. The fit procedure yields $\mu = 161.14\,\mathrm{GeV}$, $\sigma = 12.92\,\mathrm{GeV}$ and purity $\frac{S}{S+B} = 34\%$.

By comparing the fit results listed in Tables 3.6, 4.1 and 4.3 it is evident that the manner of selecting jets and events has an impact on the reconstructed top quark and W boson masses. Selection Set 1 results in lower reconstructed top quark masses than the standard analysis for all four different methods of hadronic top quark mass reconstruction. Selection Set 2 results in even lower values for all reconstructed hadronic masses for top quarks or W bosons. Additionally, the fit errors on the hadronic masses become larger and the width of the mass peaks becomes broader.

Also, by comparing the results listed in Tables 3.5, 4.2 and 4.4 it is apparent that selection Sets 1 and 2 result in lower signal purities and higher background contaminations. A priori no selection is preferred and finally the bias of the reconstructed top quark mass

has to be determined from Monte Carlo datasets with different input top quark masses. The differences of these methods may serve as an estimate of the systematic uncertainty stemming from this source.
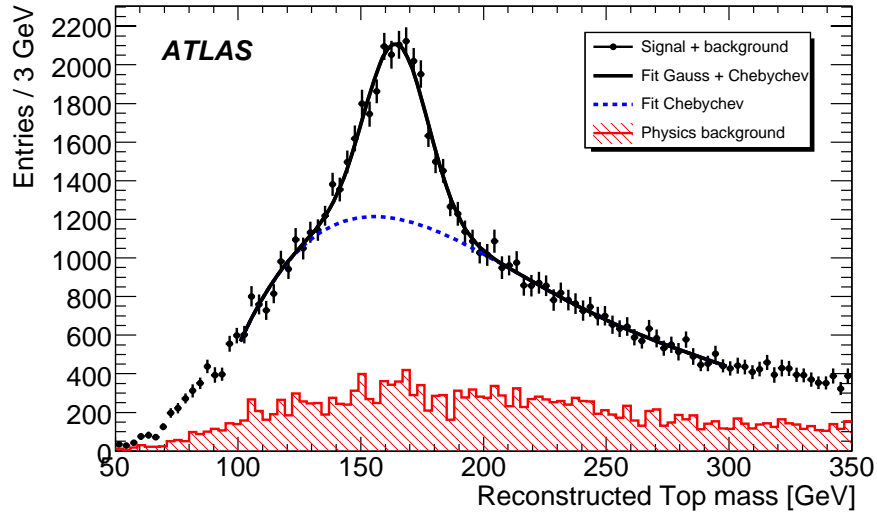

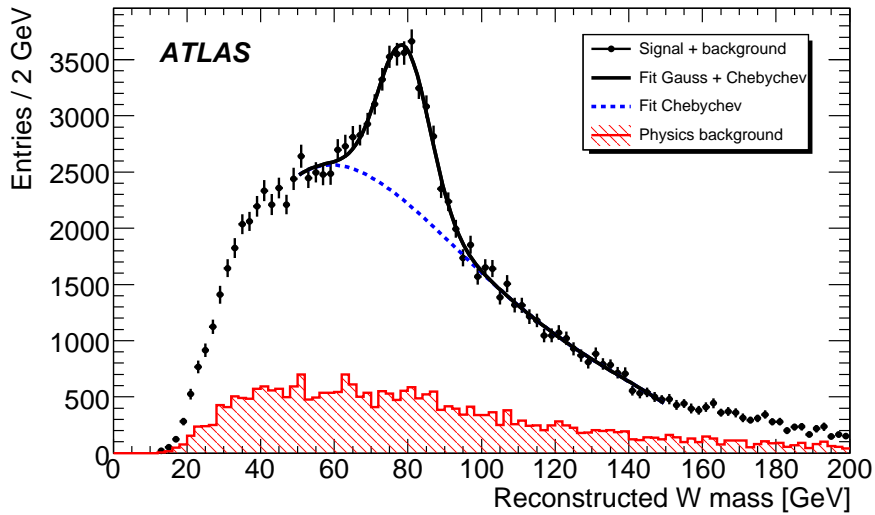Figure 4.3: *Same as Figure 3.5, but for those events that fulfill selection Set 2.*

Figure 4.4: *Same as Figure 3.6, but for those events that fulfill selection Set 2.*

	fit parameters of Gaussian [GeV]	
	mean(μ) $\pm$ fit error	width(σ) $\pm$ fit error
m_t without m_W requirement	164.43 $\pm$ 0.55	12.81 $\pm$ 0.70
m_t with m_W req. (ΔR method)	163.68 $\pm$ 0.49	15.72 $\pm$ 0.64
m_t with m_W req. (highest p_T method)	162.42 $\pm$ 0.72	13.52 $\pm$ 0.83
m_t with m_W req. (Δm method)	163.69 $\pm$ 0.53	14.75 $\pm$ 0.68
m_W (ΔR method)	79.09 $\pm$ 0.35	6.95 $\pm$ 0.50
m_W (highest p_T method)	79.91 $\pm$ 0.36	6.80 $\pm$ 0.48
m_W (Δm method)	80.22 $\pm$ 0.11	6.71 $\pm$ 0.16

Table 4.3: *Fit results of the mass analysis for the top quark and the W boson mass. The events were selected with selection Set 2.*

	Purity	background contamination	
	$\frac{S}{S+B}$	total	signal region
Top without m_W requirement	39%	32%	20%
Top with m_W req. (ΔR method)	59%	25%	15%
Top with m_W req. (highest p_T method)	43%	25%	17%
Top with m_W req. (Δm method)	49%	29%	18%

Table 4.4: *Purity and physics background contamination of the top quark mass analysis. The events were selected with selection Set 2.*
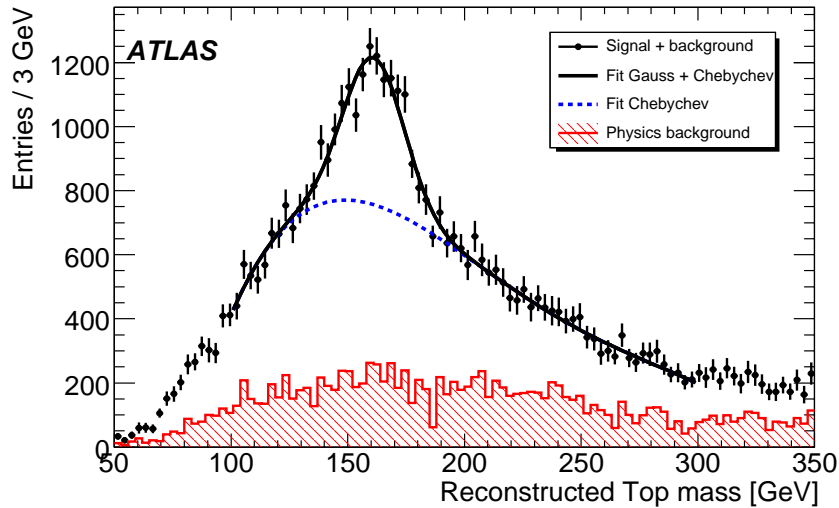

Figure 4.5: *Same as Figure 3.5, but for those events that fulfill selection Set 2 and not the standard analysis selection.*

4.2   Jet algorithms

Since the jet selection has a profound impact on the reconstructed top quark and W boson masses, the underlying jet definition is expected to have an impact as well. To quantify this, the analysis was repeated for different jet definitions, i.e. with different jet algorithms and steering parameters. Different jet definitions are necessary because there is no universal jet finding algorithm for the hadronic final states. Jet finding algorithms are used to connect the hadronic final state with the original partons that are invisible because of the confinement of colored objects (cf. Section 1.1.1).

All jets were reconstructed from topological clusters that are defined as a group of neighboring calorimeter cells formed around a seed cell [55]. The 3-dimensional shape of the topological cluster represents the shower created by the incident particle.

To calibrate the calorimeter response correctly for electromagnetic and hadronic showers two different schemes were used and compared. Firstly the cell signal weighting procedure called H1-weighting [57] discussed in Section 3.4 was used, and secondly the application of the local hadron calibration at the level of topological clusters [61]. The constants used for the local hadron calibration did not have all corrections applied yet and thus resulted in a underestimation of the hadronic energy scale by about 8% [62].

For the purpose of jet reconstruction the topological clusters are treated as massless pseudo-particles that are added up to form jets by 4-momentum addition. The 4-momentum $(E, \vec{p})$ of each cluster is constructed from the (calibrated) energy measurement of the calorimeter cells and the η-ϕ-direction of the energy-weighted barycenter of the cluster.

The jet algorithms used fall into two categories, cone algorithms and k_T algorithms.

4.2.1   Cone jet algorithm

The cone jet algorithm used for jet finding can be described as a seeded fixed size cone algorithm with a split/merge procedure implemented. Only a brief summary is given here, the algorithm is described in detail in [56].

1. The jet finding starts from seeds, i.e. topological clusters above a threshold of $p_\mathrm{T} > 1$ GeV. The first jet is built around the seed with the highest p_T.

2. Neighboring clusters are added to the jet if they are within $\Delta\mathrm{R} < \mathrm{R_{cone}}$ of the seed.

3. The new jet direction is then calculated from the 4-momentum sum.

4. New clusters are added to the jet, or old ones taken out again, depending on wether they pass or fail the $\Delta\mathrm{R} < \mathrm{R_{cone}}$ requirement with respect to the new jet direction.

5. Steps 3 and 4 are repeated until a stable configuration for this jet is found. The jet is then written into the output jet list. All clusters remain in the input cluster list, i.e. they can be assigned to jets more than once.

6. The algorithm starts again at step 1 with the next highest p_T seed. This is repeated until all seeds were used.

It is likely that topological clusters are now shared between jets that were found with this algorithm. A split/merge procedure is implemented to rectify this.

- Two jets are merged into one jet if the clusters they share make up more than 50% of the p_T of the less energetic jet.

- If the p_T-fraction of the sum of the shared clusters is less than 50% of the p_T of the less energetic jet, then each of the shared clusters is uniquely assigned to one of the jets. Each cluster is assigned to the jet that is closest in ΔR and removed from the other jet.

This jet definition is not stable in the presence of soft or collinear radiation from the original partons. This is a direct consequence of the seeding to start jet finding.

For the purpose of this study two values of the R_{cone}-parameter were used, namely $R_{cone} = \{0.4, 0.7\}$.

4.2.2 k_T jet algorithm

The other type of algorithm for jet finding used in this study was a k_T algorithm [63] following the computationally efficient implementation from [64]. The algorithm is described here in brief. The algorithm works on an input list of protojets that is initially populated with the topological clusters. Protojets are clustered together according to their proximity in k_T-space defined by the two distance measures d_{ij} and d_i for all protojets i, j:

$$d_{i,j} = min(p_{T,i}^2, p_{T,j}^2) \cdot \frac{\Delta R_{i,j}^2}{\mathbf{R}^2} \tag{4.1}$$

$$d_i = p_{T,i}^2 \tag{4.2}$$

d_{ij} denotes the relative p_T^2 between two jets i, j weighted by $1/\mathbf{R}^2$, where the parameter $\mathbf{R}$ determines the final size of the jets. d_i denotes the relative p_T^2 between jet i and the beam axis.

The k_T algorithm has two main execution modes, an inclusive and an exclusive way of jet finding. The inclusive mode is defined as follows:

1. The algorithm computes d_{ij} and d_i for all protojets in the input list. It then finds the smallest distance measure d_{ij}, d_i among all protojets.

2. If the smallest distance is d_{ij} then the algorithm merges the protojets i, j into a new protojet k. It then removes i, j from and adds k to the protojet list.

3. If the smallest distance is d_i then the algorithm considers the protojet i as a final jet, adds it to the final jet list and removes it from the protojet list.

4. The algorithm starts again at step 1 with the updated protojet list. This is repeated until the protojet list is empty.

The exclusive mode is defined as follows:

1. The algorithm computes d_{ij} and d_i for all protojets in the input list. It then finds the smallest distance measure d_{ij}, d_i among all protojets.

2. If the smallest distance $d_{min} > \mathbf{D_{cut}}$ then the algorithm moves all remaining protojets to the final jet list and terminates.

3. If the smallest distance is d_{ij} then the algorithm merges the protojets i, j into a new protojet k. It then removes i, j from and adds k to the protojet list.

4. If the smallest distance is d_i then the algorithm considers the protojet i as a beamjet, i.e. as a part of the proton remnant from the collision and removes it from the protojet list and discards it.

5. The algorithm starts again at step 1 with the updated protojet list.

Alternatively the exclusive mode can be run without step 2 but with a parameter $\mathbf{N}$ that terminates the algorithm once the number of protojets is equal to $\mathbf{N}$. This forces the event topology to the desired number of final jets.

The jets found with the k_T algorithm do not share clusters by definition, so no split/merge procedure is necessary.

The k_T algorithm is inherently stable against infrared and collinear radiation as it does not use seeds to start jet finding. However, this feature can be spoiled by seeded preclustering as it is the case for the finding and building of topological clusters.

The steering parameter of the inclusive k_T algorithm is the R-parameter. In this study it was set to R = {0.3, 0.4, 0.5, 0.6, 0.7, 0.8}. For the exclusive k_T algorithm the R-parameter was set to 1.0 but the $\mathrm{D_{cut}}$- or N-parameter were varied: $\mathrm{D_{cut}} = \{(10\,\mathrm{GeV})^2,$ $(15\,\mathrm{GeV})^2, (20\,\mathrm{GeV})^2, (25\,\mathrm{GeV})^2, (30\,\mathrm{GeV})^2, (35\,\mathrm{GeV})^2, (40\,\mathrm{GeV})^2\}$ or N = {4, 5}.

4.2.3   Influence of different jet algorithms on the analysis

As stated above, the analysis was repeated with all different jet definitions outlined in Sections 4.2.1 and 4.2.2. The fit results for all seven hadronic mass fits for the different jet definitions are listed in Tables 4.5 - 4.11. Finally, Figure 4.6 shows a summary of all hadronic fit values for the jet definitions under consideration.

The fit results from failed hadronic mass fits are marked as "not converged" in the tables and are not shown in Figure 4.6. The invariant mass spectrum of such a failed fit attempt (W boson reconstruction with the highest p_T method, exclusive k_T jet algorithm with $\mathrm{D_{cut}}$ = $(10\,\mathrm{GeV})^2$) can be seen in Figure 4.7.

It is important to note that the absolute mass value for a certain jet algorithm is not a relevant measure of the performance of this algorithm, since the jet energy calibration is not final yet. The width, the purity and the relative mass with respect to the mass values from other jet algorithms are relevant quantities. Another important quality criterion is the stability of the fit for all hadronic reconstruction methods. Finally, the fit results should be stable under small variations, e.g. of the jet parameters or of the jet energy scale (cf. Section 4.3).

Top quark mass						
algorithm type	jet parameter	name	H1	fit parameters of Gaussian [GeV]		Purity $\frac{S}{S+B}$
				mean(μ) $\pm$ error	width(σ) $\pm$ error	
Cone	$R_{cone} = 0.4$	Cone4*	✓	168.23 $\pm$ 0.54	12.77 $\pm$ 0.64	52%
	$R_{cone} = 0.7$	Cone7*	✓	184.45 $\pm$ 1.08	13.48 $\pm$ 1.38	36%
k_{T} inclusive	R = 0.4	Kt4*	✓	170.52 $\pm$ 0.58	12.91 $\pm$ 0.74	49%
	R = 0.6	Kt6*	✓	178.25 $\pm$ 0.58	12.11 $\pm$ 0.74	43%
	R = 0.3	Kt3		150.58 $\pm$ 0.92	13.01 $\pm$ 1.36	48%
	R = 0.4	Kt4		155.65 $\pm$ 0.69	11.06 $\pm$ 0.83	45%
	R = 0.5	Kt5		158.40 $\pm$ 0.64	11.82 $\pm$ 0.74	49%
	R = 0.6	Kt6		161.33 $\pm$ 0.73	13.07 $\pm$ 0.94	48%
	R = 0.7	Kt7		163.33 $\pm$ 0.79	13.83 $\pm$ 1.05	50%
	R = 0.8	Kt8		166.13 $\pm$ 1.23	15.38 $\pm$ 1.72	44%
k_{T} exclusive	$D_{cut} = (10\,\mathrm{GeV})^2$	D=10^2		166.15 $\pm$ 2.11	17.51 $\pm$ 2.97	24%
	$D_{cut} = (15\,\mathrm{GeV})^2$	D=15^2		168.53 $\pm$ 1.23	18.92 $\pm$ 1.93	41%
	$D_{cut} = (20\,\mathrm{GeV})^2$	D=20^2		170.54 $\pm$ 1.00	16.43 $\pm$ 1.39	40%
	$D_{cut} = (25\,\mathrm{GeV})^2$	D=25^2		171.36 $\pm$ 0.99	17.00 $\pm$ 1.40	42%
	$D_{cut} = (30\,\mathrm{GeV})^2$	D=30^2		172.39 $\pm$ 0.99	16.33 $\pm$ 1.22	43%
	$D_{cut} = (35\,\mathrm{GeV})^2$	D=35^2		172.80 $\pm$ 1.02	17.19 $\pm$ 1.32	47%
	$D_{cut} = (40\,\mathrm{GeV})^2$	D=40^2		172.59 $\pm$ 1.07	15.39 $\pm$ 1.27	46%
	N = 4	N=4		169.71 $\pm$ 1.74	14.81 $\pm$ 2.43	37%
	N = 5	N=5		169.99 $\pm$ 1.26	15.54 $\pm$ 1.79	37%

Table 4.5: *Fit results of the top quark masses for the 19 jet definitions under consideration. The "name" column lists the abbreviated jet algorithm and jet parameter names that denote the jet algorithms in Figure 4.6. The "H1" column shows if the jets were reconstructed from topological clusters with H1-style cell weights (ticked box) or if local hadron calibrated topological clusters were used as input (empty box).*

Top quark mass with W boson mass requirement (ΔR method)						
algorithm type	jet parameter	name	H1	fit parameters of Gaussian [GeV]		Purity $\frac{S}{S+B}$
				mean(μ) ± error	width(σ) ± error	
Cone	$R_{cone} = 0.4$	Cone4*	✓	167.82 ± 0.42	13.82 ± 0.50	70%
	$R_{cone} = 0.7$	Cone7*	✓	180.42 ± 0.78	16.13 ± 1.24	55%
k_{T} inclusive	R = 0.4	Kt4*	✓	169.86 ± 0.45	13.77 ± 0.57	67%
	R = 0.6	Kt6*	✓	176.78 ± 0.50	14.36 ± 0.70	59%
	R = 0.3	Kt3		152.94 ± 0.52	12.15 ± 0.62	69%
	R = 0.4	Kt4		156.75 ± 0.49	13.13 ± 0.60	70%
	R = 0.5	Kt5		159.40 ± 0.53	13.50 ± 0.59	69%
	R = 0.6	Kt6		161.57 ± 0.58	14.15 ± 0.67	67%
	R = 0.7	Kt7		164.69 ± 0.65	14.78 ± 0.78	67%
	R = 0.8	Kt8		167.43 ± 0.91	17.16 ± 1.15	65%
k_{T} exclusive	$D_{cut} = (10\,\text{GeV})^2$	D=10^2		165.71 ± 0.82	16.03 ± 1.07	54%
	$D_{cut} = (15\,\text{GeV})^2$	D=15^2		167.90 ± 0.70	15.86 ± 0.89	58%
	$D_{cut} = (20\,\text{GeV})^2$	D=20^2		169.30 ± 0.70	16.33 ± 0.89	59%
	$D_{cut} = (25\,\text{GeV})^2$	D=25^2		170.11 ± 0.68	16.40 ± 0.82	60%
	$D_{cut} = (30\,\text{GeV})^2$	D=30^2		170.42 ± 0.66	16.20 ± 0.72	62%
	$D_{cut} = (35\,\text{GeV})^2$	D=35^2		170.23 ± 0.66	15.90 ± 0.75	63%
	$D_{cut} = (40\,\text{GeV})^2$	D=40^2		170.37 ± 0.69	15.83 ± 0.75	63%
	N = 4	N=4		170.29 ± 0.99	15.05 ± 1.14	58%
	N = 5	N=5		169.47 ± 0.78	15.35 ± 0.91	56%

Table 4.6: *Same as Table 4.5 but for the top quark mass fits with a W boson mass requirement and using the ΔR method as defined in Section 3.6.*

Top quark mass with W boson mass requirement (highest p_T method)						
algorithm type	jet parameter	name	H1	fit parameters of Gaussian [GeV]		Purity $\frac{S}{S+B}$
				mean(μ) $\pm$ error	width(σ) $\pm$ error	
Cone	$R_{cone} = 0.4$	Cone4*	✓	166.37 $\pm$ 0.54	13.20 $\pm$ 0.66	63%
	$R_{cone} = 0.7$	Cone7*	✓	not converged		
k_T inclusive	R = 0.4	Kt4*	✓	168.71 $\pm$ 0.58	12.40 $\pm$ 0.64	58%
	R = 0.6	Kt6*	✓	175.79 $\pm$ 0.61	13.79 $\pm$ 0.75	56%
	R = 0.3	Kt3		149.03 $\pm$ 0.78	12.47 $\pm$ 1.05	59%
	R = 0.4	Kt4		153.72 $\pm$ 0.65	11.70 $\pm$ 0.74	58%
	R = 0.5	Kt5		156.64 $\pm$ 0.62	12.76 $\pm$ 0.76	62%
	R = 0.6	Kt6		158.81 $\pm$ 0.67	13.92 $\pm$ 0.87	63%
	R = 0.7	Kt7		162.45 $\pm$ 0.69	15.70 $\pm$ 1.02	69%
	R = 0.8	Kt8		not converged		
k_T exclusive	$D_{cut} = (10\,\text{GeV})^2$	D=10^2		166.37 $\pm$ 1.18	13.19 $\pm$ 1.39	37%
	$D_{cut} = (15\,\text{GeV})^2$	D=15^2		167.29 $\pm$ 1.00	15.07 $\pm$ 1.30	45%
	$D_{cut} = (20\,\text{GeV})^2$	D=20^2		167.88 $\pm$ 0.91	15.79 $\pm$ 1.17	50%
	$D_{cut} = (25\,\text{GeV})^2$	D=25^2		168.03 $\pm$ 0.86	17.18 $\pm$ 1.10	56%
	$D_{cut} = (30\,\text{GeV})^2$	D=30^2		168.43 $\pm$ 0.78	17.58 $\pm$ 0.99	63%
	$D_{cut} = (35\,\text{GeV})^2$	D=35^2		168.12 $\pm$ 0.73	17.92 $\pm$ 0.95	68%
	$D_{cut} = (40\,\text{GeV})^2$	D=40^2		168.46 $\pm$ 0.70	17.56 $\pm$ 0.83	72%
	N = 4	N=4		169.32 $\pm$ 0.91	16.86 $\pm$ 1.39	61%
	N = 5	N=5		168.02 $\pm$ 0.95	16.05 $\pm$ 1.26	54%

Table 4.7: *Same as Table 4.6 but for the highest p_T method.*

Top quark mass with W boson mass requirement (Δm method)						
algorithm type	jet parameter	name	H1	fit parameters of Gaussian [GeV]		Purity $\frac{S}{S+B}$
				mean(μ) $\pm$ error	width(σ) $\pm$ error	
Cone	$R_{cone} = 0.4$	Cone4*	✓	168.26 ± 0.50	13.39 ± 0.60	58%
	$R_{cone} = 0.7$	Cone7*	✓	183.03 ± 0.76	15.12 ± 1.17	51%
k_{T} inclusive	$R = 0.4$	Kt4*	✓	169.99 ± 0.56	13.54 ± 0.70	56%
	$R = 0.6$	Kt6*	✓	178.07 ± 0.51	13.31 ± 0.71	52%
	$R = 0.3$	Kt3		150.62 ± 0.68	12.51 ± 0.99	55%
	$R = 0.4$	Kt4		155.58 ± 0.62	11.90 ± 0.77	52%
	$R = 0.5$	Kt5		158.24 ± 0.60	12.61 ± 0.68	55%
	$R = 0.6$	Kt6		161.25 ± 0.67	13.78 ± 0.87	54%
	$R = 0.7$	Kt7		164.44 ± 0.75	16.05 ± 1.11	60%
	$R = 0.8$	Kt8		167.98 ± 1.00	18.65 ± 1.47	60%
k_{T} exclusive	$D_{cut} = (10\,\mathrm{GeV})^2$	D=10²		158.96 ± 2.66	19.18 ± 2.94	30%
	$D_{cut} = (15\,\mathrm{GeV})^2$	D=15²		166.03 ± 1.26	19.22 ± 1.69	47%
	$D_{cut} = (20\,\mathrm{GeV})^2$	D=20²		169.78 ± 0.93	17.80 ± 1.24	48%
	$D_{cut} = (25\,\mathrm{GeV})^2$	D=25²		170.90 ± 0.82	17.94 ± 1.09	52%
	$D_{cut} = (30\,\mathrm{GeV})^2$	D=30²		172.08 ± 0.74	17.22 ± 0.92	55%
	$D_{cut} = (35\,\mathrm{GeV})^2$	D=35²		172.37 ± 0.73	17.56 ± 0.94	58%
	$D_{cut} = (40\,\mathrm{GeV})^2$	D=40²		172.89 ± 0.73	16.48 ± 0.86	58%
	$N = 4$	N=4		171.50 ± 1.25	18.78 ± 1.78	54%
	$N = 5$	N=5		169.47 ± 1.02	17.19 ± 1.39	47%

Table 4.8: *Same as Table 4.6 but for the Δm method.*

W boson mass (ΔR method)						
algorithm type	jet parameter	name	H1	fit parameters of Gaussian [GeV]		Purity $\frac{S}{S+B}$
				mean(μ) $\pm$ error	width(σ) $\pm$ error	
Cone	$R_{cone} = 0.4$	Cone4*	✓	80.09 ± 0.34	6.13 ± 0.50	39%
	$R_{cone} = 0.7$	Cone7*	✓	85.87 ± 0.67	9.36 ± 0.96	37%
k_T inclusive	R = 0.4	Kt4*	✓	81.13 ± 0.43	7.08 ± 0.63	39%
	R = 0.6	Kt6*	✓	85.75 ± 0.42	7.77 ± 0.59	37%
	R = 0.3	Kt3		71.43 ± 0.56	8.60 ± 1.02	54%
	R = 0.4	Kt4		73.89 ± 0.57	7.46 ± 1.38	39%
	R = 0.5	Kt5		74.41 ± 0.79	9.69 ± 1.46	57%
	R = 0.6	Kt6		76.27 ± 0.60	8.11 ± 1.10	42%
	R = 0.7	Kt7		76.30 ± 0.60	8.28 ± 1.15	41%
	R = 0.8	Kt8		77.18 ± 1.40	10.17 ± 2.39	36%
k_T exclusive	$D_{cut} = (10\,\text{GeV})^2$	D=10^2		not converged		
	$D_{cut} = (15\,\text{GeV})^2$	D=15^2		81.01 ± 1.98	12.32 ± 2.57	38%
	$D_{cut} = (20\,\text{GeV})^2$	D=20^2		80.08 ± 1.68	11.92 ± 2.18	41%
	$D_{cut} = (25\,\text{GeV})^2$	D=25^2		80.32 ± 1.32	10.80 ± 1.79	35%
	$D_{cut} = (30\,\text{GeV})^2$	D=30^2		79.78 ± 1.43	11.23 ± 1.87	38%
	$D_{cut} = (35\,\text{GeV})^2$	D=35^2		81.05 ± 0.95	10.07 ± 1.48	34%
	$D_{cut} = (40\,\text{GeV})^2$	D=40^2		80.75 ± 1.03	11.72 ± 1.58	45%
	N = 4	N=4		81.00 ± 2.23	12.10 ± 2.83	39%
	N = 5	N=5		81.16 ± 1.22	10.66 ± 1.78	34%

Table 4.9: *Same as Table 4.5 but for the W boson mass fits and using the ΔR method as defined in Section 3.6.*

W boson mass (highest p_T method)						
algorithm type	jet parameter	name	H1	fit parameters of Gaussian [GeV]		Purity $\frac{S}{S+B}$
				mean(μ) $\pm$ error	width(σ) $\pm$ error	
Cone	$R_{cone} = 0.4$	Cone4*	✓	80.80 ± 0.44	6.70 ± 0.66	40%
	$R_{cone} = 0.7$	Cone7*	✓	not converged		
k_T inclusive	$R = 0.4$	Kt4*	✓	82.12 ± 0.47	7.10 ± 0.69	40%
	$R = 0.6$	Kt6*	✓	86.57 ± 0.54	7.88 ± 0.74	35%
	$R = 0.3$	Kt3		not converged		
	$R = 0.4$	Kt4		not converged		
	$R = 0.5$	Kt5		76.98 ± 0.55	6.67 ± 0.81	38%
	$R = 0.6$	Kt6		77.75 ± 0.52	6.43 ± 0.71	36%
	$R = 0.7$	Kt7		77.32 ± 0.59	7.74 ± 1.03	43%
	$R = 0.8$	Kt8		78.84 ± 0.88	8.08 ± 1.36	34%
k_T exclusive	$D_{cut} = (10\,\text{GeV})^2$	D=10^2		not converged		
	$D_{cut} = (15\,\text{GeV})^2$	D=15^2		82.44 ± 0.92	8.00 ± 1.37	24%
	$D_{cut} = (20\,\text{GeV})^2$	D=20^2		82.82 ± 0.83	8.35 ± 1.16	28%
	$D_{cut} = (25\,\text{GeV})^2$	D=25^2		82.86 ± 0.78	8.40 ± 1.07	30%
	$D_{cut} = (30\,\text{GeV})^2$	D=30^2		82.26 ± 0.84	9.47 ± 1.32	35%
	$D_{cut} = (35\,\text{GeV})^2$	D=35^2		82.26 ± 0.69	8.56 ± 1.09	35%
	$D_{cut} = (40\,\text{GeV})^2$	D=40^2		82.53 ± 0.68	9.27 ± 1.01	40%
	$N = 4$	N=4		82.54 ± 1.13	10.57 ± 1.89	44%
	$N = 5$	N=5		82.29 ± 1.00	9.53 ± 1.83	34%

Table 4.10: *Same as Table 4.9 but for the highest p_T method.*

W boson mass (Δm method)						
algorithm type	jet parameter	name	H1	fit parameters of Gaussian [GeV]		Purity $\frac{S}{S+B}$
				mean(μ) $\pm$ error	width(σ) $\pm$ error	
Cone	$R_{cone} = 0.4$	Cone4*	✓	80.74 ± 0.17	6.36 ± 0.25	62%
	$R_{cone} = 0.7$	Cone7*	✓	84.37 ± 0.34	7.62 ± 0.42	51%
k_T inclusive	R = 0.4	Kt4*	✓	81.51 ± 0.18	6.82 ± 0.28	60%
	R = 0.6	Kt6*	✓	83.87 ± 0.22	8.30 ± 0.30	62%
	R = 0.3	Kt3		77.19 ± 0.32	7.74 ± 0.49	55%
	R = 0.4	Kt4		78.33 ± 0.25	6.95 ± 0.41	55%
	R = 0.5	Kt5		78.68 ± 0.22	6.93 ± 0.34	60%
	R = 0.6	Kt6		79.29 ± 0.22	7.07 ± 0.33	61%
	R = 0.7	Kt7		79.32 ± 0.25	7.54 ± 0.39	62%
	R = 0.8	Kt8		80.58 ± 0.32	7.56 ± 0.48	54%
k_T exclusive	$D_{cut} = (10\,\mathrm{GeV})^2$	D=10^2		80.62 ± 0.28	7.81 ± 0.53	50%
	$D_{cut} = (15\,\mathrm{GeV})^2$	D=15^2		81.37 ± 0.28	8.27 ± 0.52	53%
	$D_{cut} = (20\,\mathrm{GeV})^2$	D=20^2		81.45 ± 0.27	8.43 ± 0.46	55%
	$D_{cut} = (25\,\mathrm{GeV})^2$	D=25^2		81.49 ± 0.27	8.09 ± 0.40	54%
	$D_{cut} = (30\,\mathrm{GeV})^2$	D=30^2		81.43 ± 0.25	8.11 ± 0.37	56%
	$D_{cut} = (35\,\mathrm{GeV})^2$	D=35^2		81.49 ± 0.26	7.63 ± 0.36	55%
	$D_{cut} = (40\,\mathrm{GeV})^2$	D=40^2		81.76 ± 0.27	7.77 ± 0.37	56%
	N = 4	N=4		81.88 ± 0.48	9.36 ± 0.82	56%
	N = 5	N=5		81.59 ± 0.32	7.99 ± 0.54	51%

Table 4.11: *Same as Table 4.9 but for the Δm method.*
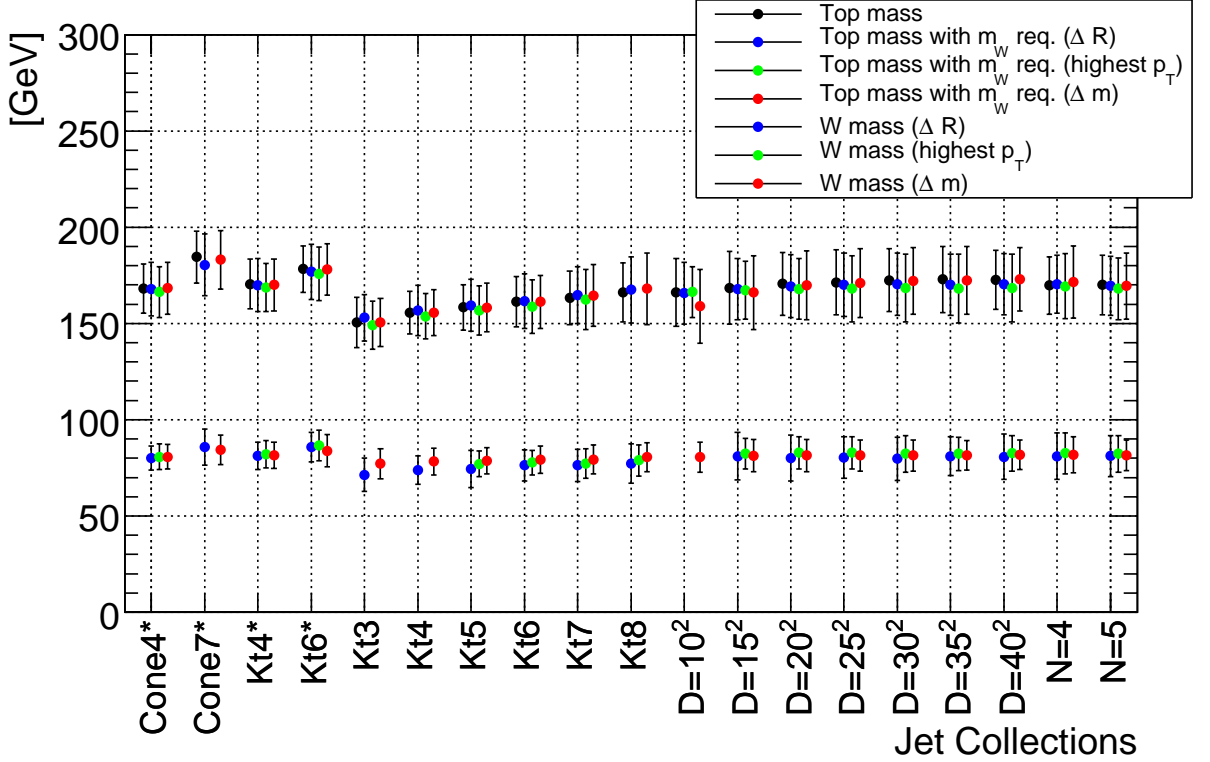
Figure 4.6: *For each of the 19 jet definitions all seven hadronic mass fits are shown. The mean values of the mass fits are shown as colored dots with the corresponding width indicated by the error bars. The top quark masses with a W boson mass cut and the corresponding W boson masses reconstructed with the same method are plotted in the same color. The (*) in the names of certain jet algorithms denotes that the jets were reconstructed from topological clusters with H1-style cell weights. All other jets were reconstructed with local hadron calibrated topological clusters. The mass values for failed fit attempts are not shown.*

By comparing the various fit results some general conclusions about the performance of the different jet algorithms can be drawn. It is apparent that among the H1-weighted jets the Cone (R = 0.4) algorithm has the smallest fit error and the highest signal purity. This is unsurprising as the H1-style cell weights were tailored to this jet definition. Nonetheless the k_T (R = 0.4) algorithm shows comparable performance.

The fit results from local hadron calibrated jets show mass values that are significantly below the original input masses. This is because of the present incompleteness of this calibration and the resulting offset in jet energy scale. Among the local hadron calibrated jets, those found with an inclusive k_T algorithm and R-parameters between 0.4 and 0.6 show the best performance.

Across all jet definitions and input calibrations a clear dependence of the fitted masses on the size of the jets is visible. Larger cone radii or larger inclusive k_T R-parameters or larger exclusive k_T D_{cut}-parameters yield higher hadronic mass fit values. Among the local hadron calibrated jets this mass dependence is most significant for the inclusive k_T jets. The effect is less pronounced for the family of exclusive k_T jets.

It is also apparent that the inclusive k_T jets yield better fit qualities, i.e. smaller fit errors than the exclusive k_T jets. Also, the fit results from local hadron calibrated jets of the inclusive and exclusive k_T mode appear to be on two different energy scales, with the inclusive scale significantly below the exclusive scale.

Some specific remarks about certain individual fit results are in order. In Table 4.9 it can be seen that the hadronic W boson mass fit with the ΔR method fails for exclusive k_T ($D_\mathrm{cut} = (10\,\mathrm{GeV})^2$) jets. The hadronic W boson mass fit with the highest p_T method fails for this jet algorithm as well, as can be seen in Table 4.10. Altogether, this method of W boson reconstruction fails for 5 of the 19 jet definitions. For the W boson mass fits it fails for H1-weighted Cone (R = 0.7) jets and for local hadron calibrated inclusive k_T (R = 0.3) and (R = 0.4) and exclusive k_T ($D_\mathrm{cut} = (10\,\mathrm{GeV})^2$) jets. For the hadronic top quark mass fits with a W boson mass cut this method fails for H1-weighted Cone (R = 0.7) jets and local hadron calibrated inclusive k_T (R = 0.8) jets, as can be seen in Table 4.7. This high failure rate is an indication of the volatility of this fit method under systematic changes of the underlying jet definition.
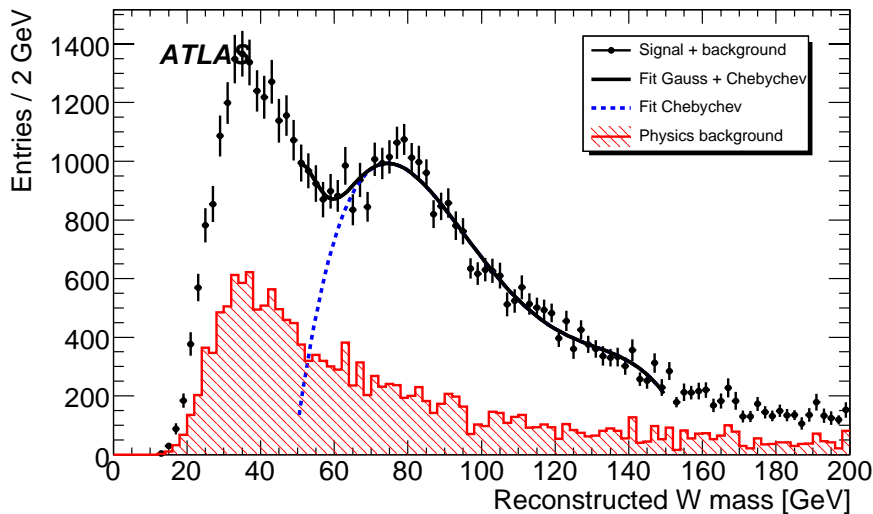
Figure 4.7: *Same as Figure 3.7 but for jets reconstructed with the exclusive k_T algorithm with $D_\mathrm{cut} = (10\,\mathrm{GeV})^2$. The attempt to fit the hadronic W boson mass from this invariant mass spectrum failed, i.e. the Gaussian part of the fit function cannot be interpreted as the W boson mass peak. In this Figure the Gaussian is centered at 40 GeV, outside of the fit range of (50 - 150) GeV.*

4.3 Jet energy scale

The experience from top quark mass measurements at the Tevatron experiments shows that the jet energy scale uncertainty is the dominant systematic uncertainty. In the light of this the impact of a variation of the jet energy scale on the analysis was studied. Furthermore the robustness of the different jet algorithms studied in Section 4.2 with respect to jet and event selection and the stability of the various hadronic mass fits was investigated.

The procedure to change the jet energy scale was as follows. The jets were reconstructed from topological clusters as described in Section 4.2. Subsequently all jet energies were rescaled with a certain universal scaling factor. Since b-tagging is not used in the analysis no attempt has been made to separate the light quark jet energy scale from the one for b-quark jets. These rescaled jets were then used as input for the analysis. This results in a migration of jets with p_T close to the cut value of 40 GeV. A jet with an original $p_T = 41$ GeV will not pass the cut if the jet energy scale is set to 95%. Conversely, a jet with $p_T = 39$ GeV will be selected if the jet energy scale is set to 105%.

The invariant mass spectra of the top quark candidates and the W boson candidates reconstructed with the ΔR method can be seen in Figures 4.8 and 4.9. In this case a scaling factor of 0.95 was used. This corresponds to a jet energy scale of 95% which means that the energy of a reconstructed jet is 5% below the original jet energy.
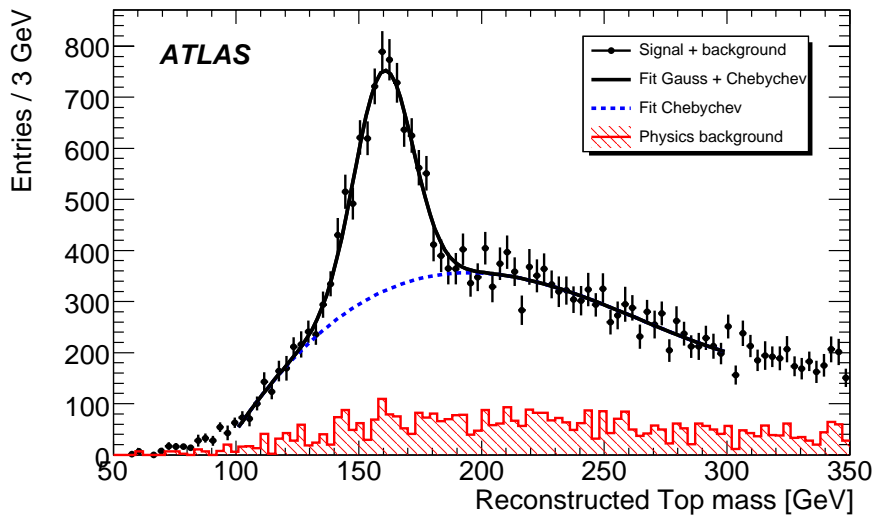
Figure 4.8: *Same as Figure 3.5, but with the jet energies rescaled to 95% of their original value.*

Figure 4.10 shows a summary of all hadronic mass fits for the different jet algorithms discussed in Section 4.2. By comparing Figures 4.6 and 4.10 it is apparent that the fitted hadronic mass is lower in the case of a jet energy scale of 95%. Also the W boson mass fits for the ΔR and highest p_T method fail over a wide range of inclusive k_T jet parameters if the calibrated topological clusters were used as input. It is also apparent that the Δm method of W boson reconstruction does not suffer from this effect but at the price of introducing a strong bias towards the input W boson mass.
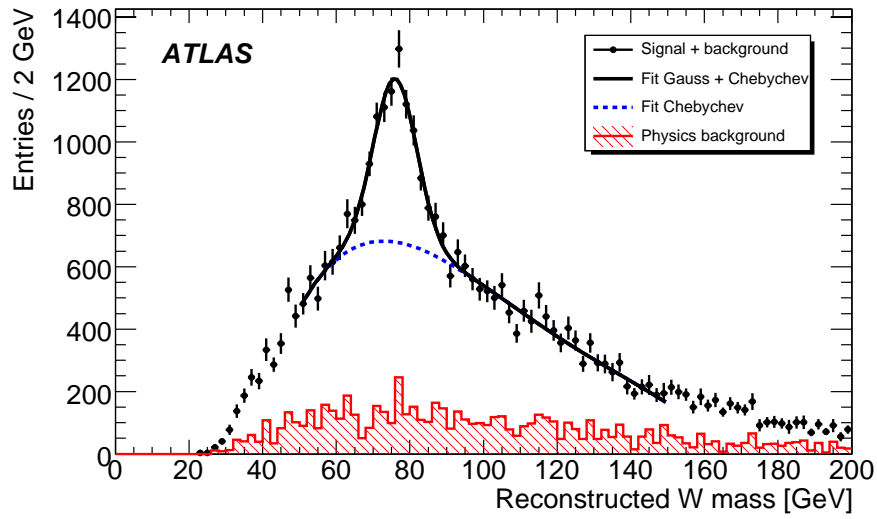
Figure 4.9: *Same as Figure 3.6, but with the jet energies rescaled to 95% of their original value.*
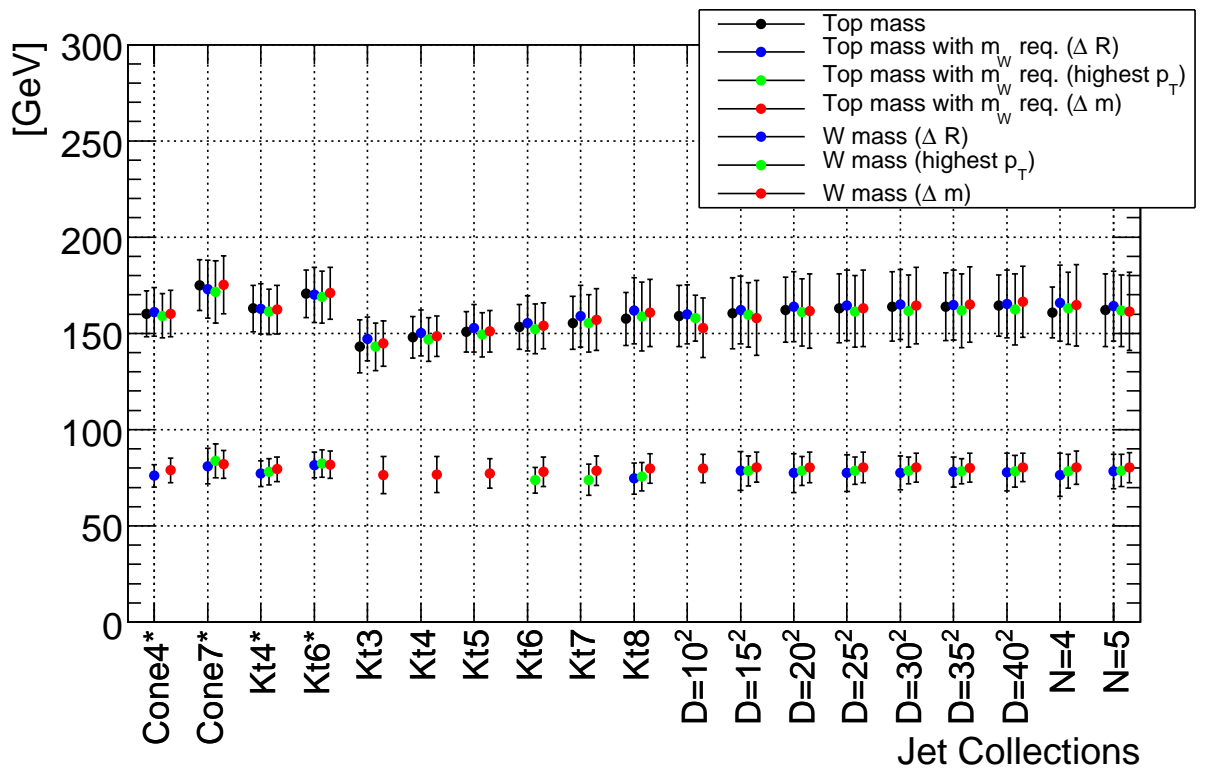
Figure 4.10: *Same as Figure 4.6, but with the jet energies rescaled to 95% of their original value.*

Figures 4.11 and 4.12 show the invariant mass spectra of the top quark candidates and the W boson candidates reconstructed with the ∆R method for a jet energy scale of 105%.
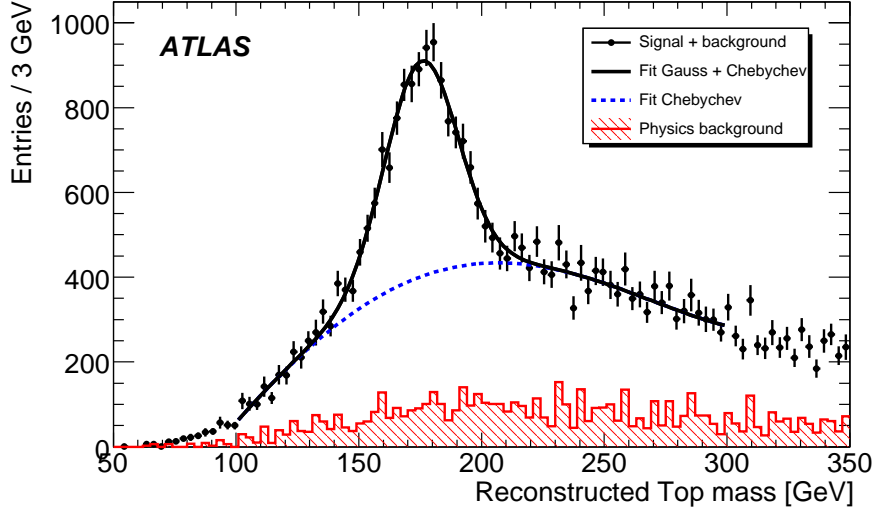
Figure 4.11: *Same as Figure 3.5, but with the jet energies rescaled to 105% of their original value.*
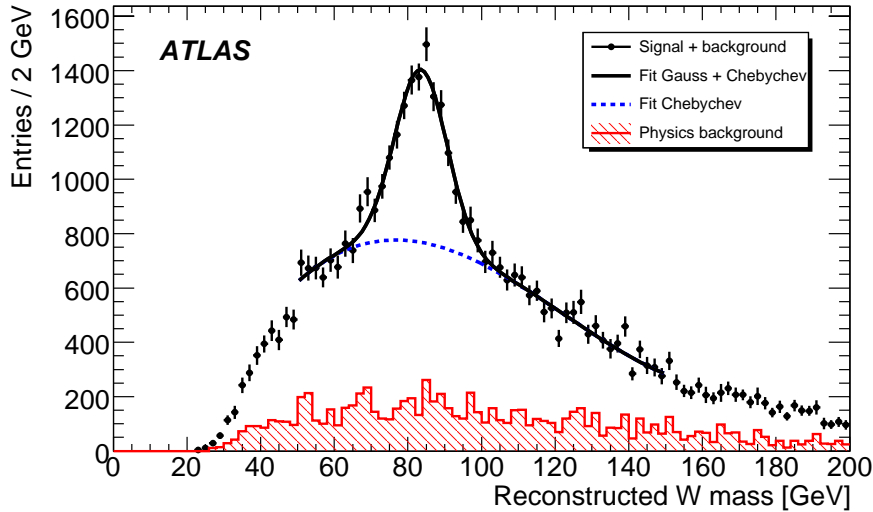
Figure 4.12: *Same as Figure 3.6, but with the jet energies rescaled to 95% of their original value.*

Figure 4.13 again shows a summary of all hadronic mass fits for a jet energy scale of 105%. By comparing Figures 4.6, 4.10 and 4.13 it is apparent that the width of the mass peaks (indicated by the error bars) becomes broader and that the problem of fit instabilities for the ∆R and highest p_T method of W boson reconstruction have disappeared for a jet energy scale of 105%. By comparing the fit results for the exclusive k_T jets the bias of the ∆m method for W boson reconstruction is clearly visible.
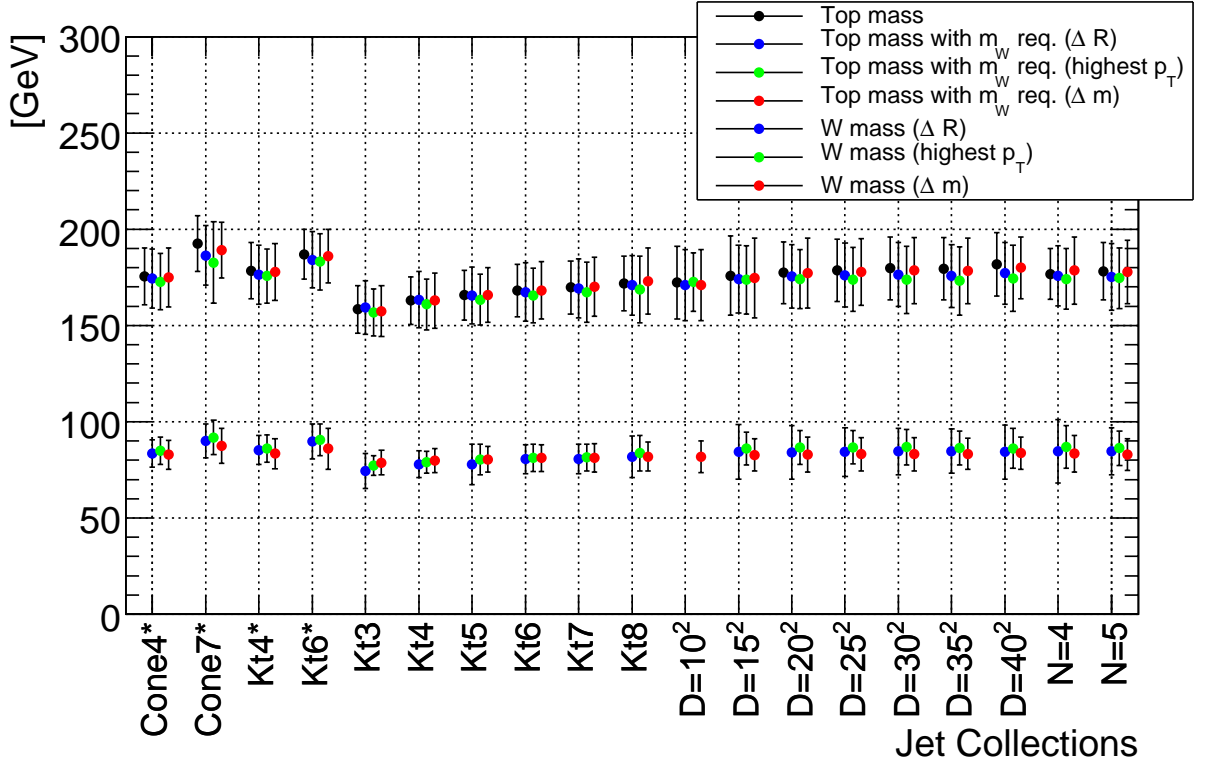
Figure 4.13: *Same as Figure 4.6, but with the jet energies rescaled to 105% of their original value.*

To estimate the component of the systematic uncertainty of the fitted hadronic masses coming from the jet energy scale uncertainty the standard analysis without a W boson mass requirement was performed with jet energy scales of 95%, 99%, 100%, 101% and 105%. A straight line was then fitted to the five corresponding mass values of each hadronic fit. The fit errors of the mass values were taken as the uncertainty of each mass point for the straight line fit. To decorrelate the five mass points a pairwise disjoint subset of 20% of the available events from the input datasets was used to fit the mass values for each jet energy scale.

The slopes of these straight line fits are then interpreted as the shifts of the hadronic mass peak for a jet energy scale uncertainty of 1%. The systematic uncertainties of the top quark mass reconstruction for the standard analysis, originating from jet energy scale variations are listed in Table 4.12 for a selected set of jet algorithms. Due to the reduced statistics (only 20% of the available events were used for each mass point), the number of mass points where the fitting procedure fails rises substantially. All the jet algorithms are listed for which all five jet energy scales yielded stable fit results.

In Table 4.12 it can be seen that the smallest jet energy scale uncertainty of the top quark mass for H1-weighted jets is achieved for the Cone (R = 0.4) algorithm. However, it needs to be noted that these systematic uncertainties obtained for different jet algorithms are correlated because the identical events were used as input. None of the fit values appears to be an outlier and as a general trend it can be observed that an uncertainty of the jet energy scale of 1% results in an 0.6% - 0.9% uncertainty of m_t.

Uncertainty of m_t from 1% ΔJES	
algorithm name	$\Delta m_\text{t} \pm$ fit error [GeV]
Cone4*	1.28 +/- 0.18
Kt4*	1.39 +/- 0.18
Kt6*	1.61 +/- 0.16
Kt4	1.29 +/- 0.20
Kt5	1.00 +/- 0.18
Kt6	1.05 +/- 0.19
D=20^2	1.05 +/- 0.26

Table 4.12: *Systematic uncertainty of the hadronic top quark mass from jet energy scale variations for selected jet algorithms. The "algorithm name" column lists the abbreviated jet algorithm name introduced in Table 4.5.*

4.4 Conclusions on systematic effects

As shown in Section 4.1 the kinematics of jet selection have an impact on the reconstructed hadronic masses. Softer jet selection cuts yield lower reconstructed hadronic mass values, whereas harder cuts yield higher mass values. In a final analysis this effect will need to be corrected for. Using a softer jet selection degrades the quality of the hadronic mass fits, decreases the signal purity and increases the background contamination. All three effects are undesirable and so the use of softer jet selection cuts is not advisable.

From the results shown in Section 4.2 it is clear that with fully calibrated input both, Cone and inclusive k_T jet algorithms with a R-parameter of 0.4 perform equally well and yield good results. It is also apparent that steering parameters that yield too small jets or too large jets lead to degraded fit results and are not suited for the event topology of top-antitop pair decays.

Another observations from the results in Section 4.2 is that inclusive and exclusive k_T jet definitions yield inherently different hadronic mass fit results. Two very different sets of jet calibration constants will be necessary for these two execution modes of the k_T algorithm. It is probably even necessary to have two different sets of analysis selection cuts depending on the underlying jet definition.

From the findings in Sections 4.2 and 4.3 it becomes apparent that each of the three methods employed for W boson mass reconstruction has shortcomings. The ΔR and the highest p_T method show instabilities under the variation of the jet energy scale. Also, the fit failure of the highest p_T method for various jet algorithms underlines this volatile behavior. On the other hand the Δm method provides very stable and robust results for most systematic variations that were studied. This robustness comes at the price of introducing a strong bias on the fitted W boson mass values.

Consequently, applying a W boson mass requirement for the top quark mass reconstruction implicitly introduces the same shortcomings into the top quark mass fits. The ΔR and the highest p_T method introduce volatility into the fit results and the Δm method introduces a bias. This bias is apparent by comparing the background contaminations listed in Tables 3.5, 4.2 and 4.4 for the top quark reconstruction with W boson mass cuts. The

Δm method always has the highest background contamination among the three methods. This is understandable because, due to the bias, background events that should have been rejected, suddenly pass the W boson mass cut. Due to this, the W boson mass cut with the Δm method looses some of its usefulness.

Also, reconstruction of the top quark with the help of a W boson mass requirement does not yield improved fit results, i.e. smaller fit errors compared to the top quark reconstruction without a W boson mass cut. Consequently, this cut is not necessary or even advisable for a top quark mass analysis with early LHC collision data. The cut may be useful for top quark analyses that need a high signal purity (e.g. cross-section analyses), but application of this cut will need careful scrutiny.

Chapter 5

Alignment of the ATLAS Inner Detector

A high quality alignment of the ATLAS Inner Detector is important for ATLAS in general to reach its full physics potential. In the context of the commissioning style top quark mass analysis presented here, it is especially important for the event selection. The top quark mass analysis depends on electron and muon reconstruction for event selection. Both lepton reconstruction algorithms, egamma [53] for electrons and Staco [54] for muons, use Inner Detector tracks to reconstruct and calculate the lepton 4-momenta. The egamma algorithm uses the Inner Detector track of the electron to determine the electron direction and the Staco algorithm combines the Inner Detector and the muon system information to perform a global track fit for muons. The performance of both lepton reconstruction algorithms and thus the quality of the event selection of the analysis directly depends on the quality of the alignment of the ATLAS Inner Detector. Also, any refinement of the analysis that will involve b-tagging needs high quality alignment. One important ingredient in b-tagging is secondary vertex reconstruction and the quality of this is directly affected by residual Pixel misalignment.

In the following an alignment procedure for the Pixel and SCT subdetectors is described, the *Local* χ^2 alignment approach [65, 66]. In the first part of this Chapter track-based alignment and the *Local* χ^2 alignment approach are introduced. Then the performance of the *Local* χ^2 approach for combined testbeam (CTB) data from 2004 is described and the results are compared to other alignment approaches that are in use for the ATLAS Inner Detector. Finally the *Local* χ^2 approach is applied to data from the ATLAS cosmic runs taken in fall 2008.

5.1   Track-based alignment

The goal of alignment is to determine the actual positions and orientations of the active detector elements. The deviation of the actual detector position from the nominal detector position is taken into account during track reconstruction. This happens in the form of six alignment parameters per Pixel or SCT module, namely the six degrees of freedom of a rigid body. The alignment parameters are three translations (x, y, z) along the local

coordinate axes of a module and three rotations (α, β, γ) around the local coordinate axes, following the ATLAS convention established in [67].

Track-based alignment derives alignment parameters $\mathbf{a} = $ (x, y, z, α, β, γ) by minimizing track residuals r. The residual is defined as the distance between the hit recorded in the detector element and the fitted particle track. More rigorously

$$r_i \equiv (\vec{m}_i(\mathbf{a}) - \vec{t}_i(\boldsymbol{\pi})) \cdot \hat{e}_i \tag{5.1}$$

where i is the index denoting the i-th residual of a given track. The vector $\vec{m}_i$ denotes the position of the hit and depends on the alignment parameters, $\vec{t}_i$ denotes a point on the extrapolated track and depends on the track parameters $\boldsymbol{\pi} = (d_0, z_0, \phi_0, \theta_0, q/p)$ [68] and $\hat{e}_i$ denotes the unit vector of the measurement direction. A pixel hit always has two residuals with $\hat{e}_i = \hat{e}_x$ (perpendicular to the long Pixel coordinate) and $\hat{e}_i = \hat{e}_y$ (perpendicular to the short pixel coordinate). A hit in one plane of an SCT module has only one residual with the measurement direction $\hat{e}_i = \hat{e}_x$ (perpendicular to the strip coordinate).

The definition in Equation 5.1 contains ambiguities, namely which point $\vec{e}_i$ to choose along the track and how exactly the measurement direction $\hat{k}_i$ is defined especially for the fan geometry of the strips in SCT endcap modules. Among the ATLAS Inner Detector alignment approaches three different residual definitions are in use, namely a linear in-plane residual, an angular in-plane residual and a distance of closest approach (DOCA) residual.

The linear and angular in-plane residuals use as track extrapolation point $\vec{e}_i$ the intersection point of the track with the detector plane and differ in the definition of the measurement direction $\hat{k}_i$, as can be seen in Figure 5.1. The DOCA residual uses a different extrapolation point $\vec{e}_i$, namely the point where the distance between track and detector hit is minimal and it uses yet another measurement direction $\hat{k}_i$ namely a measurement direction that points out of the detector plane to the extrapolation point. This is depicted in Figure 5.1 as well.

The explicit dependence of the residual on the alignment parameters $\mathbf{a}$ via hit positions and the implicit dependence via track parameters $\boldsymbol{\pi}$ allows the extraction of alignment parameters from accumulated track residual information.

5.2 The Local χ^2 alignment approach

Each of the ATLAS Inner Detector alignment approaches uses a unique method to extract alignment parameters. The *Local χ^2* alignment approach is based on a linear least squares minimization:

$$\chi^2(\mathbf{a}, \boldsymbol{\pi}_1, \ldots, \boldsymbol{\pi}_t) = \sum_{i \, \in \, tracks} \mathbf{r}_i{}^T V_i^{-1} \mathbf{r}_i \ . \tag{5.2}$$

Here, $\mathbf{r}_i = \mathbf{r}_i(\mathbf{a}, \boldsymbol{\pi}_i)$ is the vector of residuals measured for the fitted track i and V_i is the covariance matrix of these residual measurements. The generic solution for the alignment corrections is shown in Equation 5.3. A rigorous derivation can be found in [70].
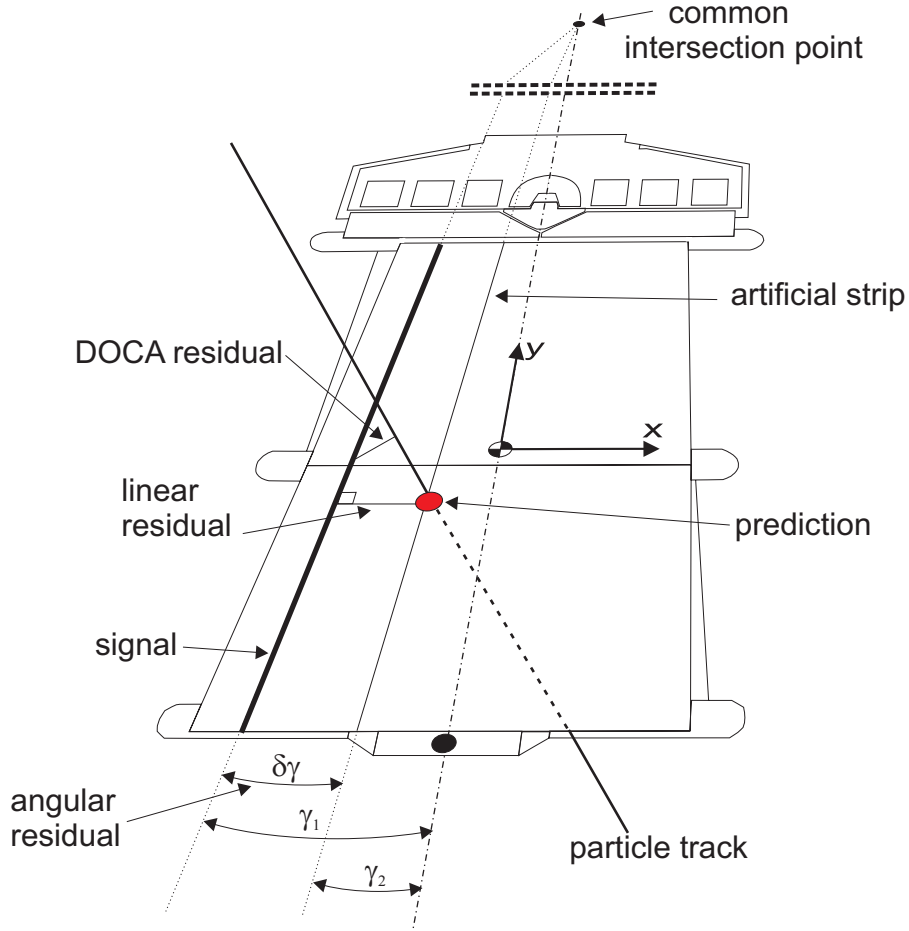
Figure 5.1: *Various residual definition used for SCT endcap module hits: Shown are the linear and angular in-plane residuals, and the distance of closest approach (DOCA) residual [69].*

$$\delta\mathbf{a} = -\left(\sum_{i\,\in\,tracks}\left(\frac{d\mathbf{r}_i}{d\mathbf{a}}\right)^T V^{-1}\left(\frac{d\mathbf{r}_i}{d\mathbf{a}}\right)\right)^{-1}\sum_{i\,\in\,tracks}\left(\frac{d\mathbf{r}_i}{d\mathbf{a}}\right)^T V^{-1}\mathbf{r}_i$$

$$= -A^{-1}\sum_{i\,\in\,tracks}\left(\frac{d\mathbf{r}_i}{d\mathbf{a}}\right)^T V^{-1}\mathbf{r}_i \qquad (5.3)$$

Here, A^{-1} is the covariance matrix of the alignment corrections. For the *Local* χ^2 alignment approach the covariance matrix V in Equation 5.2 is assumed to be diagonal and the diagonal elements σ_i^2 correspond to the measurement uncertainties squared of the residuals $\mathbf{r}_i$. This approximation neglects correlated residual errors, e.g. from multiple scattering. The alignment corrections are calculated for each module separately. This neglects correlations between modules, hence the name *Local* χ^2. Thus, to obtain alignment corrections the *Local* χ^2 alignment algorithm calculates the solution of six coupled linear equations for each module (because of the six degrees of freedom per module). Detailed discussions about the approximations that enter into the *Local* χ^2 solution of Equation 5.2 can be

found in [65, 66, 70].

The *Local* χ^2 alignment approach uses the distance of closest approach residual as defined above. The algorithm is executed iteratively to bring correlations between modules into play through updated track parameters from the track fitting. That is, alignment corrections are derived and used to update the existing alignment parameters. Using these updated parameters new tracks are fitted and new residuals are calculated and a new set of alignment corrections is calculated. This is repeated until a stable set of alignment corrections is obtained.

5.3   Track reconstruction

The input for track-based alignment are tracks found and fitted by track reconstruction algorithms. For the *Local* χ^2 alignment presented here the track reconstruction was done by the CTBTracking algorithm [71].

The pattern recognition part of CTBTracking was developed specifically for the combined testbeam (CTB) detector setup outlined below. It was later extended to recognize the hit patterns of cosmic muons going through the ATLAS Inner Detector. Track candidates are found by looping through combinations of space points in different modules, and that combination is selected for which a fast track fit yields the smallest χ^2. This procedure is tailored to the CTB case of single track events and useable for cosmic events as well, where the track multiplicity is low. It would be too CPU intensive for LHC collision events where the track multiplicity is very high.

In contrast, the track fitting part of the CTBTracking algorithm, which is based on a global χ^2 minimization technique is in use for track reconstruction of collision events as well. For runs without magnetic field straight line tracks are fitted and for runs with magnetic field a helical particle trajectory is fitted. In both cases scattering planes at every silicon detector layer are incorporated into the fit to describe multiple scattering and energy loss of particles.

The CTBTracking algorithm has a few features and options that are directly useful for track-based alignment approaches. In the fit the charge/momentum track parameter q/p can be constrained to a fixed value, e.g. in the CTB case to the signed momentum of the incident particles as delivered by the beam test facility. Also the option is used to remove ganged pixels from the track finding and fitting procedures. This eliminates a source of ambiguities for the alignment approaches.

The hit error used for track fitting and alignment is calculated as $\frac{pitch}{\sqrt{12}}$, where *pitch* denotes the size of the readout element, i.e. the SCT readout strip width or the readout pixel length or width. For the Pixel detector it is possible to refine the hit error estimate, especially for large pixel clusters. This is done for the track reconstruction of the cosmic muons but not for the CTB runs. In the CTB case the necessary calibration constants are not available. The $\frac{pitch}{\sqrt{12}}$ estimate is an upper bound of the true uncertainty and the only effect on the alignment is a slower convergence.

5.4 Combined testbeam alignment

In 2004 almost all ATLAS subdetectors participated in a combined testbeam (CTB) run at the CERN H8 beam-test facility. The ATLAS subdetector components chosen represented a wedge of the ATLAS detector at pseudorapidity $\eta = 0$.

In this Section the alignment of the Inner Detector silicon part of the ATLAS CTB setup is presented. The detector setup and the *Local* χ^2 alignment strategy are outlined. Then the performance of the *Local* χ^2 alignment is presented and compared to three other alignment approaches, namely the *Robust* [72], the *Valencia* [73] and the *Global* χ^2 [74] approach.

5.4.1 Combined testbeam detector setup

The Inner Detector part of the ATLAS CTB setup consisted of six Pixel modules, eight SCT endcap outer modules and two TRT barrel modules. The Pixel and SCT modules were located within a dipole magnet that produced a maximum magnetic field strenght of 1.4 T. The TRT modules were placed outside of the magnet due to spatial constraints. A sketch of the CTB Inner Detector geometry and the relative placement of the Pixel, SCT and TRT detectors and the dipole magnet is shown in Figure 5.2.

Figure 5.2: *Schematic representation of the ID components and the magnet at the CTB.*

A detailed drawing of the silicon module positions is shown in Figure 5.3. The six Pixel modules were arrayed in three layers labeled (0, 1, 2) and two phi sectors (0, 1). As for the ATLAS detector, each Pixel module was tilted with respect to the incident beam by 20° with the long pixel coordinate as rotation axis. Two Pixel modules in the same layer had an overlap of about 200 μm. The eight SCT modules were arrayed in four layers (0, 1, 2, 3) and two phi sectors (0, 1), with a 4 mm overlap perpendicular to the strip direction for modules in the same layer.

Figure 5.3: *Configuration of the six Pixel and eight SCT modules in the CTB Inner Detector setup.*

5.4.2   Combined testbeam data samples used for alignment

The data taking was divided into five different periods that are characterized by different material distribution and detector positioning. The material distribution in the Inner Detector volume was modified by the addition or removal of the aluminium plates that are shown in Figure 5.2. For the CTB alignment the datasets of that period were used where no extra material layers were present. During this period runs with e^+ and π^+ beams with different momenta were recorded, both with and without magnetic field. In Table 5.1 the run numbers and run properties are listed for the datasets used by the alignment approaches to obtain or to validate alignment parameters. Typically, 10k events from each run are used.

Run Number	Particle Type	Energy (GeV)	magnetic field
2102355	π^+	100	Off
2102439	e^+	20	On
2102400	e^+	50	On
2102452	e^+	80	On
2102399	e^+	100	On
2102463	e^+	180	On
2102442	π^+	20	On
2102365	π^+	100	On

Table 5.1: List of runs selected to obtain or validate the alignment results.

Due to the beam profile and the scintillator trigger acceptance window the Pixel and SCT detectors were not illuminated homogeneously. Only an area of $3 \times 3\,\mathrm{cm}^2$ (the acceptance window size) in the overlap region of the modules was illuminated uniformly by the beam. This can be seen in Figure 5.4 where the hit maps of a Pixel and a SCT module are shown. It is apparent that for Pixel modules the illumination covered the entire length of the precision coordinate. For SCT modules only about a third of the readout strips of a module were illuminated.
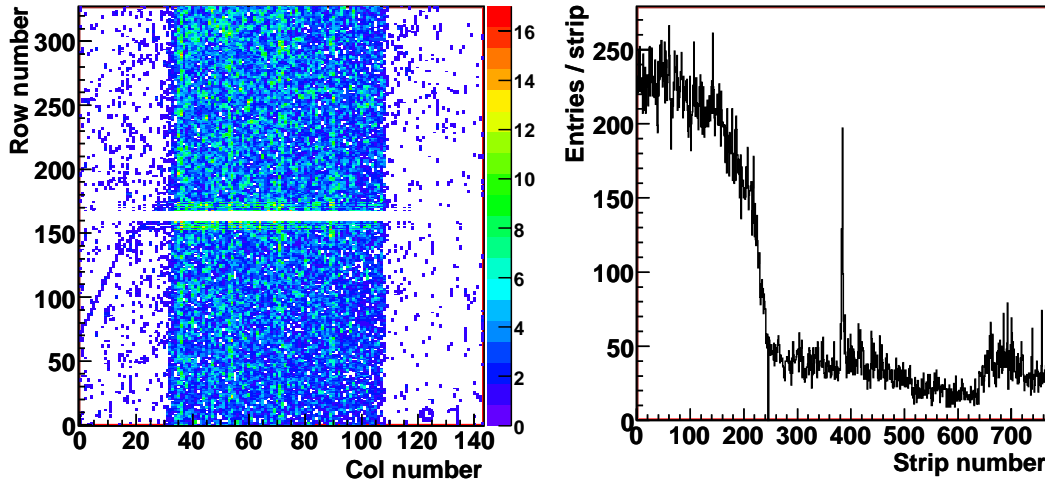
Figure 5.4: *Left: Pixel hit map for a 100 GeV pion run. The horizontal axis denotes the global Z-coordinate of the CTB setup (i.e. the long Pixel readout coordinate) and the vertical axis the global Y-coordinate (i.e. the short Pixel readout coordinate). Right: SCT hit map for the same run.*

5.4.3   The local χ^2 alignment strategy

The CTB detector setup and beam configuration is a degenerate setup for track-based alignment, e.g. modules are not fully illuminated and particles always come with the same incident angle. Therefore, additional steps are necessary to ensure that the *Local χ^2* alignment approach yields a stable set of alignment parameters. These steps are a momentum constraint, stabilization terms in the matrix A from Equation 5.3, and an enrichment of overlap hits with respect to non-overlap hits.

The momentum of the incident particles provided by the beam test facility is more precise than the intrinsic momentum resolution of the CTB Inner Detector setup. Consequently, this information is used as an external information during track fitting to constrain the track curvature.

The stabilization terms are added to the diagonal elements of the matrix A from Equation 5.3 and act like additional measurements with zero residual, full sensitivity in the corresponding degrees of freedom and uncertainties of $\sigma_{stability}$ [75]. They constrain the alignment correction to be within $\sigma_{stability}$ per iteration. This prevents that large initial misalignments spoil the convergence behavior of the alignment parameters. The stability terms were set to (10 μm, 10 μm, 100μm) for the (x, y, z) coordinates of the Pixel modules and to 100 μm for the (x, y, z) coordinates of the SCT modules. For all rotational degrees of freedom $\sigma_{stability}$ was set to 1 mrad. The changes of the alignment parameters are smaller than the respective $\sigma_{stability}$ after about 20 iterations.

Overlap hits, i.e. hits lying in the overlap region of the two modules in the same layer have a profound impact on the alignment parameters as they constrain the relative positions of modules within a layer. Also the residual calculation is more precise for overlap hits than for non-overlap hits. Overlap and non-overlap hits systematically constrain different

alignment degrees of freedom and a combination of both types of hits as input for the alignment gives the best result. Non-overlap hits for example are necessary for a stable alignment of the CTB detector setup, because overlap hits are collected on only one side of every module. To enhance the impact of overlap hits (more precisely, to not wash out the alignment information of a few hundred overlap hits with thousands of non-overlap hits), residuals from non-overlaps hits were rejected once a certain quota was reached. Empirically it was found that this goal can be reached with a quota of 400 for the number of non-overlap hits per module.

10k events from each of the the three pion runs listed in Table 5.1 (20 GeV and 100 GeV momentum with magnetic field and 100 GeV momentum without magnetic field) were used as input for the *Local* χ^2 alignment approach with the proper momentum applied as a constraint during track fitting. For the 100 GeV run without magnetic field the momentum constraint during track fitting is needed for the correct calculation of the material corrections during track fitting.

5.4.4   Alignment results and comparison

The *Local* χ^2 alignment approach was iterated 60 times on the event sample described above. The flow of the six alignment parameters through the iterations is shown in Figure 5.5 for each of the six Pixel modules. In Figure 5.6 the same is shown for the eight SCT modules. It can be seen that after ten iterations nearly all degrees of freedom of all modules have converged to stable values. Only the alignment parameters of the local y-coordinate of the Pixel and SCT modules converge much slower. Apparently there is a large initial misalignment for this coordinate for the SCT modules and this coordinate runs parallel to the SCT readout strips, so these alignment parameters are only loosely constrained. Because of correlations the alignment parameters of the local y-coordinate of the Pixel modules converge with the same speed.

Apart from the convergence behavior the track parameter resolution is an indicator for the achieved alignment quality. For the CTB setup the track curvature, i.e. the momentum reconstruction is the most sensitive indicator. This measurement is not distorted by global transformations which the alignment approaches are insensitive to, and the initial momentum of the particles is precisely known. Figure 5.7 shows the recovery of the momentum resolution for the 100 GeV pion run with the alignment corrections from the *Local* χ^2 alignment. Without alignment corrections the momentum measurement is highly degraded.

It is difficult to compare the sets of alignment parameters obtained by the different alignment approaches with each other. Every approach used different constraints to become insensitive to global transformations. Also, every approach aligned a different number of degrees of freedom of each module (e.g. the *Robust* approach aligned only two degrees of freedom) and a different number of modules (e.g. the *Global* χ^2 approach did not align the first Pixel module and the last SCT module but used them as anchor points to remove global transformations). The *Local* χ^2 alignment approach used data from runs with and without magnetic field, whereas the other approaches only used runs without magnetic field. Only the *Local* χ^2 alignment approach aligned all six degrees of freedom of all six Pixel and eight SCT modules, however, by using the constrains as detailed above.
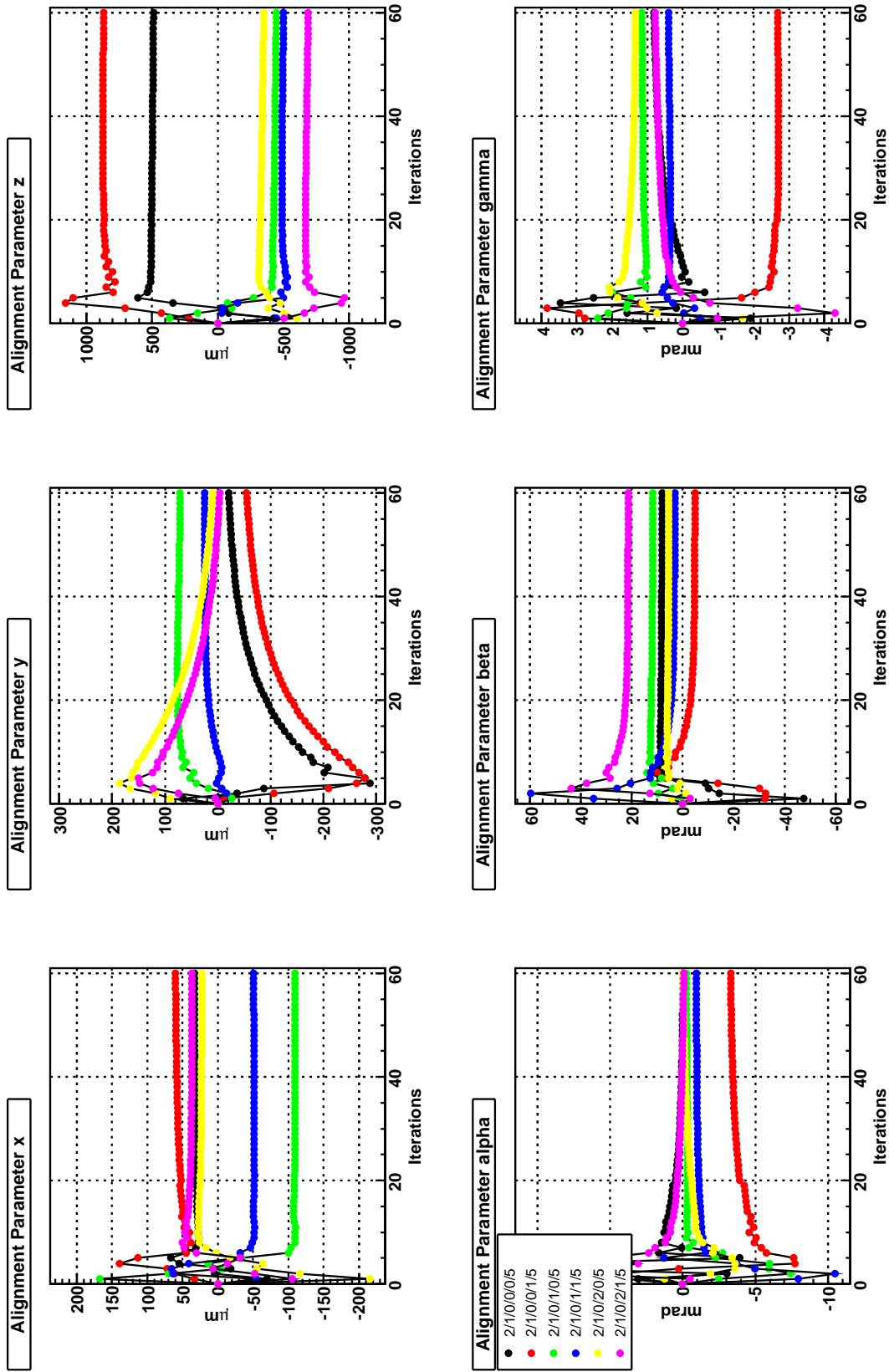
Figure 5.5: *Flow of the alignment parameters of the six Pixel modules through the iterations of the Local χ^2 alignment algorithm. The labelling of the modules follows the convention of the ATLAS readout identifiers [40] also described in short in Section 2.2.2.*
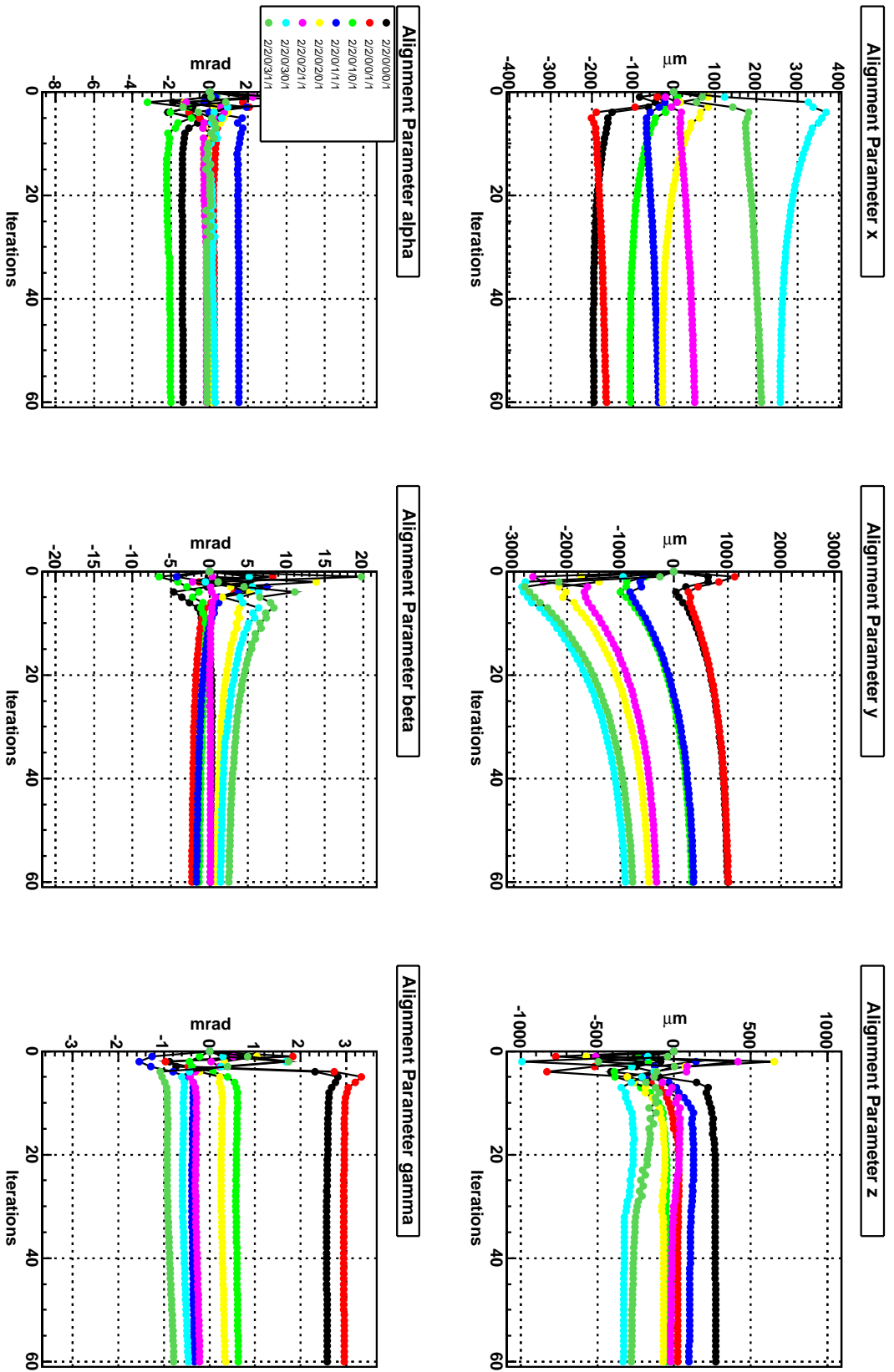
Figure 5.6: *Same as Figure 5.5, but for the eight SCT modules.*
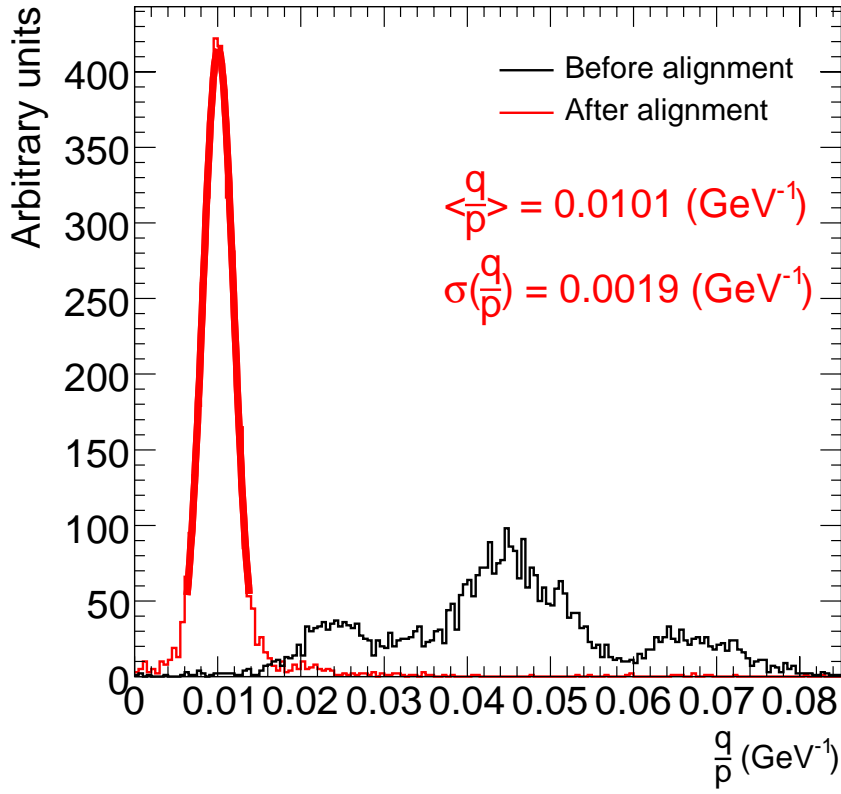
Figure 5.7: *Momentum resolution of the Pixel and SCT detectors for a 100 GeV pion run with magnetic field with and without alignment corrections.*

In addition, there exists no survey data for the CTB Inner Detector setup to which the derived alignment parameters can be compared. So a direct comparison or even validation of the alignment parameters is not possible. Instead the quality of the different sets of alignment parameters is compared. Figure 5.8 shows one comparison of the alignment approaches with each other and with simulation. The momentum resolution obtained for electrons and pions with different momenta is depicted for simulated particle tracks as well as for tracks reconstructed with all four sets of alignment parameters. The momentum resolutions obtained with the *Local* χ^2, the *Global* χ^2 and the *Valencia* approaches are consistent with the simulation results that are obtained with a nominal CTB Inner Detector setup. The momentum resolution achievable with the alignment parameter set obtained with the *Robust* approach is significantly worse, especially at high momenta. This is because of remaining misalignments in the degrees of freedom that were not aligned in this approach.

For other track parameters or track properties (e.g. hit multiplicities) the results are similar. Agreement of the four approaches with each other and with simulation is good. Also here the largest deviations are present for the *Robust* alignment approach, as expected for the reasons discussed above.
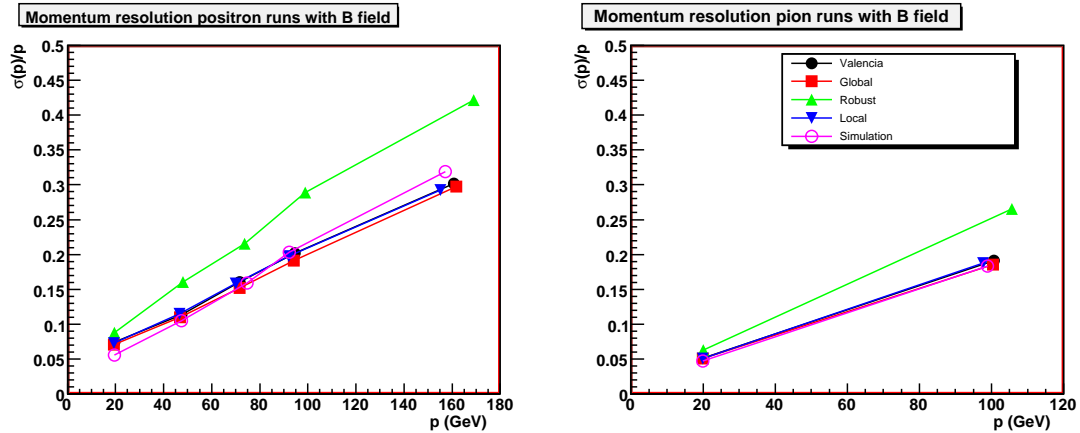
Figure 5.8: *Momentum resolution for various particle momenta reconstructed with different alignment parameter sets. For comparison the momentum resolution without misalignment derived from simulation is shown as well. Left: positron runs. Right: π^+ runs.*

5.5   Alignment with data from cosmic radiation

In fall 2008 the whole ATLAS detector was used for a six-week period of cosmic data taking. The primary cosmic rays [76] that hit the earth's atmosphere interact with the nuclei of the atmosphere and create secondary particles that in turn interact with other nuclei. A particle cascade called an air shower develops [77]. The electrons, photons and muons of these showers reach the surface of the earth, but only the muons have the penetration power to also reach the ATLAS detector in the cavern below ground.

In this Section the performance of the *Local* χ^2 alignment approach for the cosmic muon data is presented. First the detector configuration and the data processing are outlined, then the properties of the cosmic muon tracks used for alignment are discussed and the alignment strategy is explained. Finally the results, i.e. the convergence of the alignment parameters, the improvements on the residual distributions and the improvements on the track parameter resolution are shown.

5.5.1   Detector configuration

During the six weeks of cosmic data taking the whole ATLAS detector was operated and among other things the interplay between various detector components was tested. During most of the time both ATLAS magnet systems, namely the toroid and the solenoid magnets, were operated with nominal field strength, so that most of the data taking runs are with magnetic field. For test purposes and consistency checks, but also because of unscheduled magnet system shutdowns, a fraction of the runs was performed without magnetic field.

A schematic view of the cosmic data taking detector setup is shown in Figure 5.9. It shows the ATLAS detector in the cavern, the rock and concrete formations above and the surface area at ground level. All the structures above ATLAS act as shielding that slows and stops the cosmic muons before reaching the detector. The two access shafts provide pathways

for the muons with a minimal amount of material in the way. The access shafts and their different diameters result in a non homogeneous illumination of the ATLAS detector with cosmic muons. The resulting properties of the reconstructed cosmic muon tracks will be discussed in Section 5.5.3.
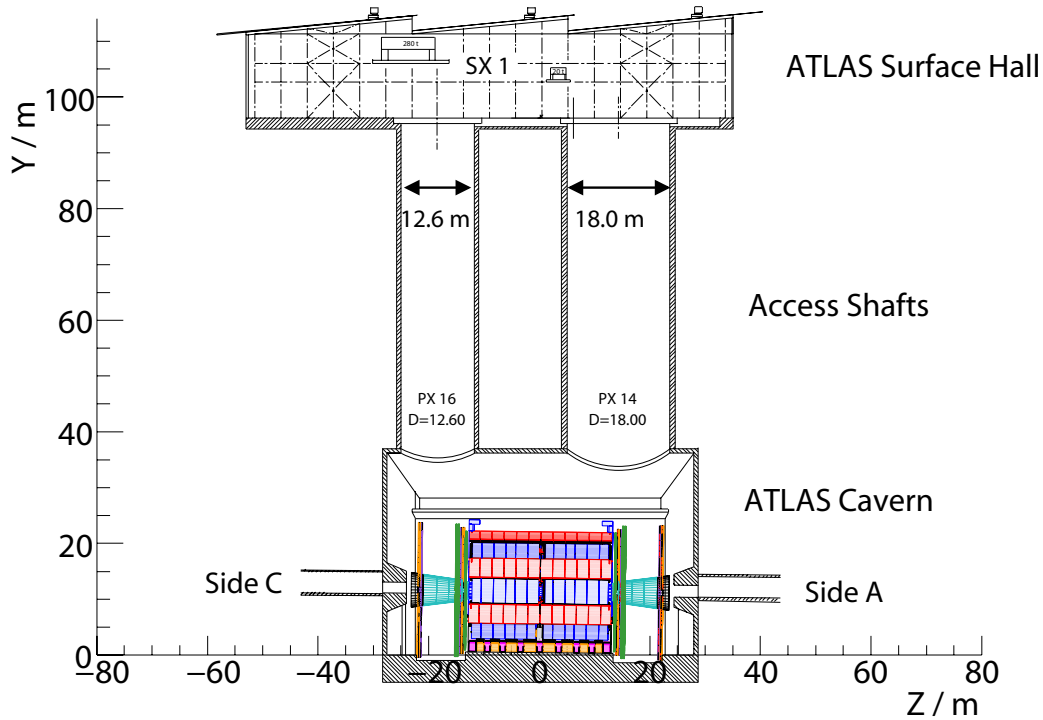
Figure 5.9: *Schematic drawing of the ATLAS detector in the cavern together with the access shafts through the rock, the concrete above the cavern and the surface building [78].*

5.5.2 Data processing

The trigger system of ATLAS was modified to recognize the signatures of cosmic muons going through the detector. For the cosmic data taking the main trigger came from the muon trigger system, namely from the RPC and TGC subdetectors (cf. Section 2.2.4). For the track-based alignment of the Pixel and SCT detectors the events from the IDCosmics trigger output stream are used. This stream contains a subset of the recorded events with at least one track obtained by the fast track reconstruction algorithms [79, 80] of the Inner Detector.

This event preselection is further refined by the offline processing of the data where the Inner Detector tracks are reconstructed with the CTBTracking algorithm [71] as outlined in Section 5.3. Only events where at least one Inner Detector track is reconstructed with this algorithm are used as input for the *Local* χ^2 alignment [81].

The online and offline data processing that provided the input for the alignment was done with the ATLAS software framework release Athena 14.2.22 with various bugfix software patches applied during the six weeks of data taking. Consequently, the data quality in

the later runs is significantly improved compared to earlier runs. The alignment itself was done with Athena 14.5.0 with all the bugfixes in place already. Apart from the pattern recognition the Inner Detector track reconstruction was redone so that the data quality of the alignment input should be the same for all runs.

5.5.3   Properties of cosmic muon tracks

For the *Local* χ^2 alignment 141k tracks from runs without magnetic field and 658k tracks from runs with magnetic field were used. The tracks without magnetic field are not curved and are fitted as straight lines. These tracks act as a reference in the curvature reconstruction for tracks with infinite momentum. This provides valuable information for the alignment because it helps to correct misalignments that distort the curvature reconstruction.

The distributions of the four perigee track parameters d_0, z_0, ϕ and θ for the runs without magnetic field are shown in Figure 5.10.

The d_0 distribution (Figure 5.10a) shows the geometric acceptance of the Pixel and SCT detectors (cf. Section 2.2.2). From the z_0 distribution (Figure 5.10b) it becomes evident that the barrel parts of these detectors yielded much more reconstructed tracks than the endcap parts. This is understandable by looking at the angular ϕ and θ distributions (Figures 5.10c and d) that depict the track directions. The tracks are downward going with the main peak of the azimuth angle distributions at $-\frac{\pi}{2}$, i.e. along the negative y-direction. The two smaller peaks in the ϕ distribution can be attributed to trigger effects. The θ spectrum shows a steep inclination angle as well, which means that tracks going through the endcap volumes generally do not hit enough readout modules to be reconstructable. Consequently the illumination of the Pixel and SCT barrel modules with reconstructed tracks is much higher than for the endcap modules.

The effect of the two access shafts with different diameter is clearly visible in the distribution of the polar angle θ. The large peak comes from tracks that arrive through the big access shaft, whereas the smaller peak comes from tracks that arrive through the smaller access shaft.

As there is no momentum measurement for these tracks, there is also no momentum cut-off in place, apart from the implicit cut-off that these muons were triggered and had the penetration power to reach the Inner Detector. This means that soft tracks with a momentum of less than $1\,\mathrm{GeV}$ dominate in this track sample.

The distributions of the five perigee track parameters d_0, z_0, ϕ, θ and q/p as well as the track momentum p for runs with magnetic field are shown in Figure 5.11. The d_0, z_0, ϕ and θ distributions (Figures 5.11a-d) for these runs show the same structures as the distributions for the runs without magnetic field.

The q/p curvature spectrum (Figure 5.11e) shows tracks with momenta down to $5\,\mathrm{GeV}$ and the momentum distribution (Figure 5.11f) shows tracks with momenta up to $10\,\mathrm{GeV}$, so the whole momentum range is visible. The pronounced peaks in the momentum distributions at $4\,\mathrm{GeV}$ come from primary tracks, i.e. such tracks that triggered an event. The $4\,\mathrm{GeV}$ muon momentum coincides with the PDG value of the mean energy of cosmic muons [27]. The peaks at $0.5\,\mathrm{GeV}$ are mainly from additional tracks that are found in these events.
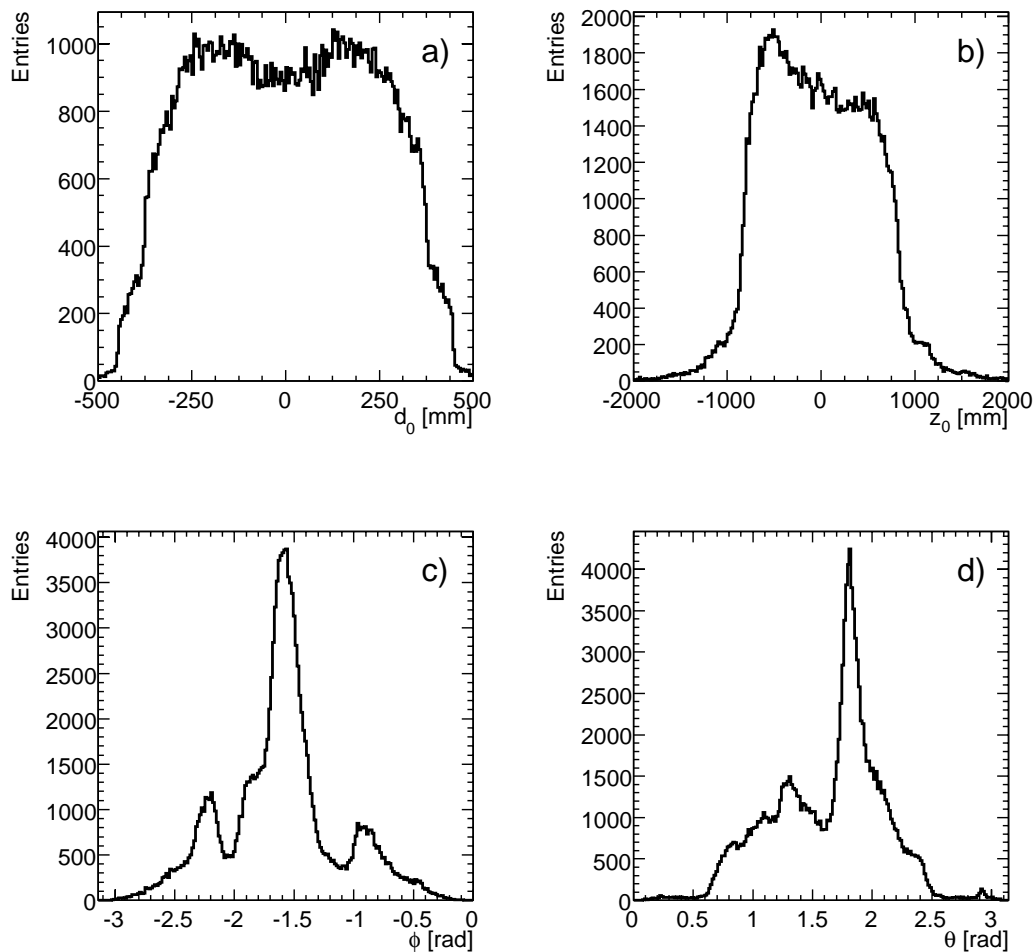
Figure 5.10: *Distributions of track parameters of cosmic muon tracks reconstructed without magnetic field. Shown are a) the d_0 distribution, b) the z_0 distribution, c) the ϕ distribution and d) the θ distribution.*

Another feature is clearly visible in the curvature and momentum distributions, namely the μ^+/μ^- charge asymmetry in cosmic air showers. From the distributions one can determine a raw charge ratio $N_{\mu^+}/N_{\mu^-} = 1.37$. For the momentum range of the cosmic muons detected by ATLAS the charge ratio N_{μ^+}/N_{μ^-} was measured by the LEP L3 collaboration to be 1.285 ± 0.003 (stat.) ± 0.019 (sys.) [82]. No attempt has been made to correct the raw charge ratio measured by ATLAS for systematic effects like the detector acceptance.
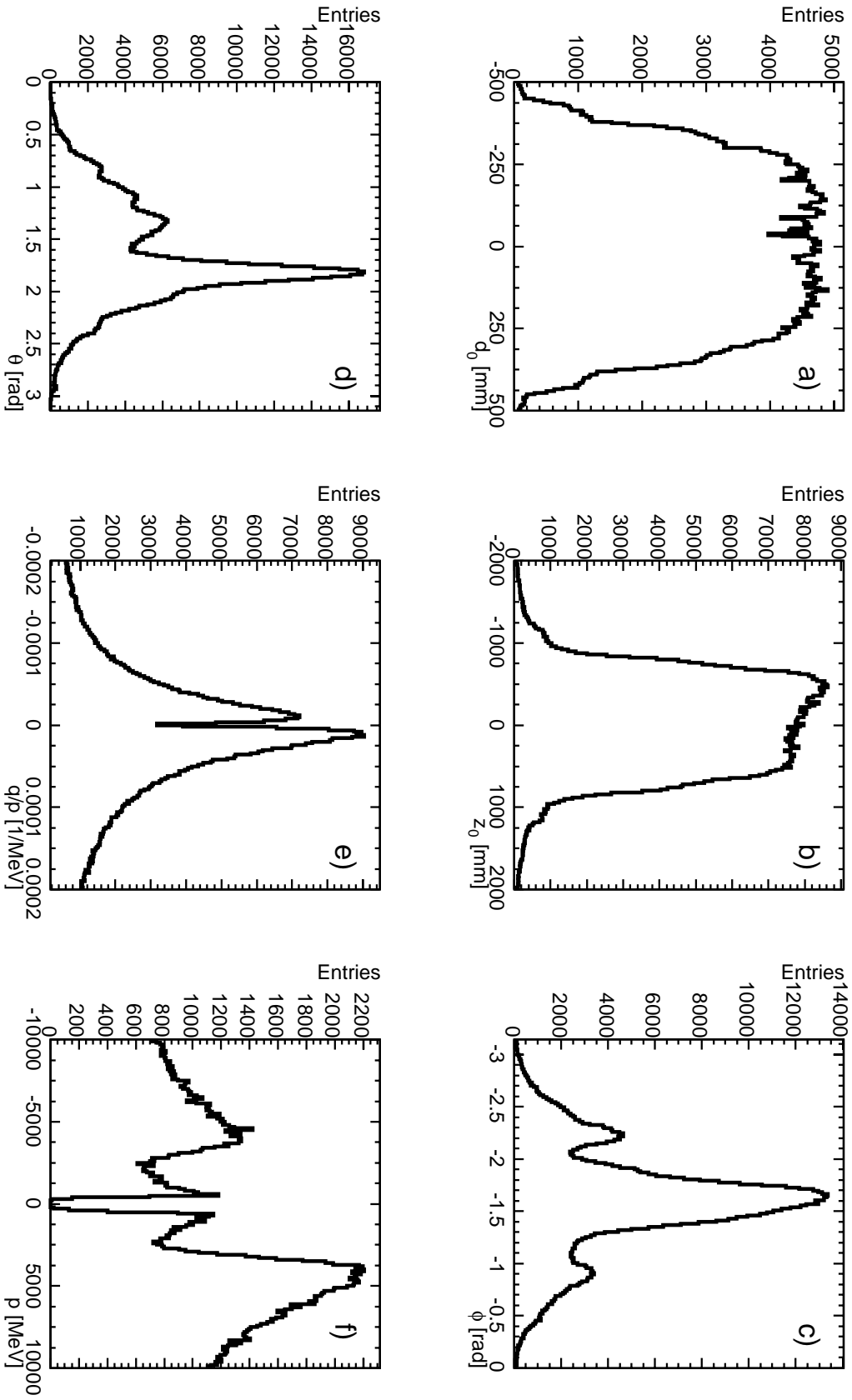
Figure 5.11: *Distributions of track parameters of cosmic muon tracks reconstructed with magnetic field. Shown are a) the d_0 distribution, b) the z_0 distribution, c) the ϕ distribution, d) the θ distribution, e) the q/p distribution and f) the p/q distribution.*

5.5.4   Alignment at different levels of granularity

The goal of the *Local χ^2* alignment of the Pixel and SCT detectors is to provide alignment corrections for all six degrees of freedom of each individual module. This is only possible if every module has enough hits to be properly aligned. Empirically it was found that 100 hits on a module are enough to achieve this.

As discussed in the previous section, for the cosmic data the Pixel and SCT endcap modules do not fulfill this requirement. Consequently, coarser levels of alignment granularity are necessary, i.e. to align endcap disks and barrel layers or even whole subdetectors as rigid bodies with only six degrees of freedom. To achieve this, the alignment of the ATLAS Inner Detector is organized in hierarchical levels, namely level 1, 2 and 3 alignment.

Alignment at level 1 deals with 4 rigid bodies, namely the whole Pixel detector, the SCT barrel and the two SCT endcaps. Alignment at level 2 has 31 rigid bodies, namely all the endcap disks and barrel layers of the Pixel and SCT detectors. Finally, level 3 alignment treats all 5832 modules individually.

For the *Local χ^2* alignment with cosmic muons four iterations were done at level 1, followed by ten iterations at level 2, which in turn were followed by eleven iterations at level 3. The iterations at level 3 were only performed for the Pixel and SCT barrel modules, i.e. the alignment of the endcaps was not updated during these iterations. With the available statistics of cosmic muon tracks all operational Pixel and SCT barrel modules had enough hits and could be aligned successfully at level 3. Finally, 25 iterations on top of the level 3 alignment were performed at level 2, to match the endcap and the barrel alignment.

It must be noted that the "local" alignment coordinates xyz for the level 1 and level 2 structures coincide with the ATLAS global coordinate frame XYZ.

5.5.5   Alignment results

In the following, the results of the *Local χ^2* alignment with cosmic muons are presented and discussed. First the flow and the convergence of the alignment parameters through the iterations is shown. Then residual distributions for the different levels of alignment granularity are evaluated and compared. Finally, the improvement of the track parameter resolution by the alignment is presented.

Alignment parameter flow

The flows of the six alignment parameters of each alignable object through the four level 1, ten preliminary level 2 and 25 final level 2 iterations are shown in Figures 5.12 - 5.14. The flows of the level 2 alignment corrections start at the positions where the corresponding level 1 structures converged to. For some degrees of freedom there is a discontinuity in the alignment parameter flow visible at iteration 35. This is an artifact and comes from an instability in the execution of the *Local χ^2* alignment at iteration 35. The *Local χ^2* alignment was run such that every luminosity block of recorded data (about 10k events) was processed in a different job, for a total of 750 parallel jobs. In some iterations one job failed, mostly due to database access or network problems. During iteration 35 three jobs failed.
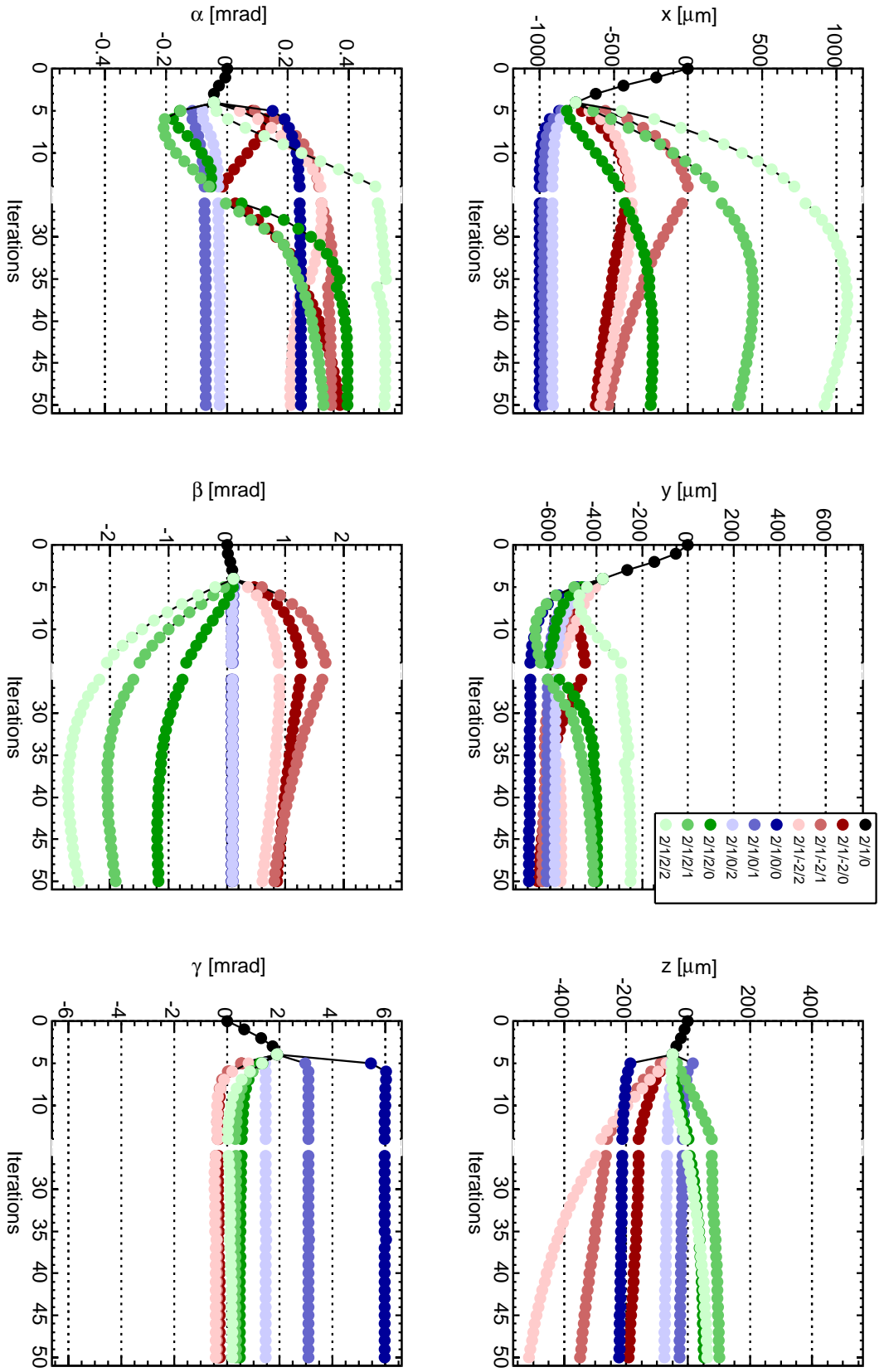
Figure 5.12: *Flow of the alignment parameters of the Pixel detector and the Pixel barrel layers and endcap disks through the iterations of the Local χ^2 alignment algorithm. From left to right and top to bottom the x, y, z, α, β and γ coordinates are shown. The labeling of the level 1 and level 2 structures follows the convention of the ATLAS readout identifiers [40] also described in short in Section 2.2.2.*
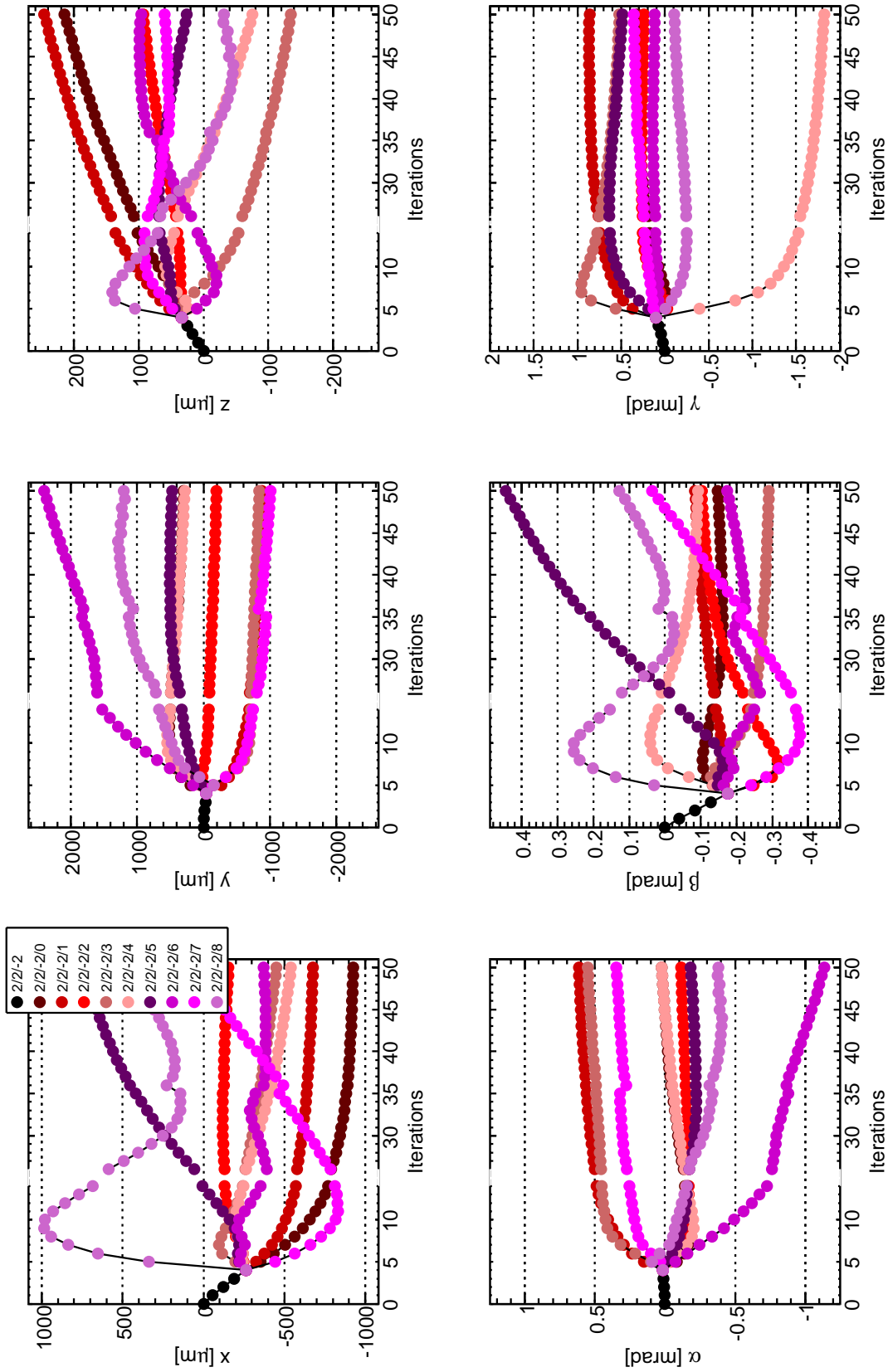
Figure 5.13: *Same as Figure 5.12, but for the SCT endcap C as well as the individual endcap C disks.*
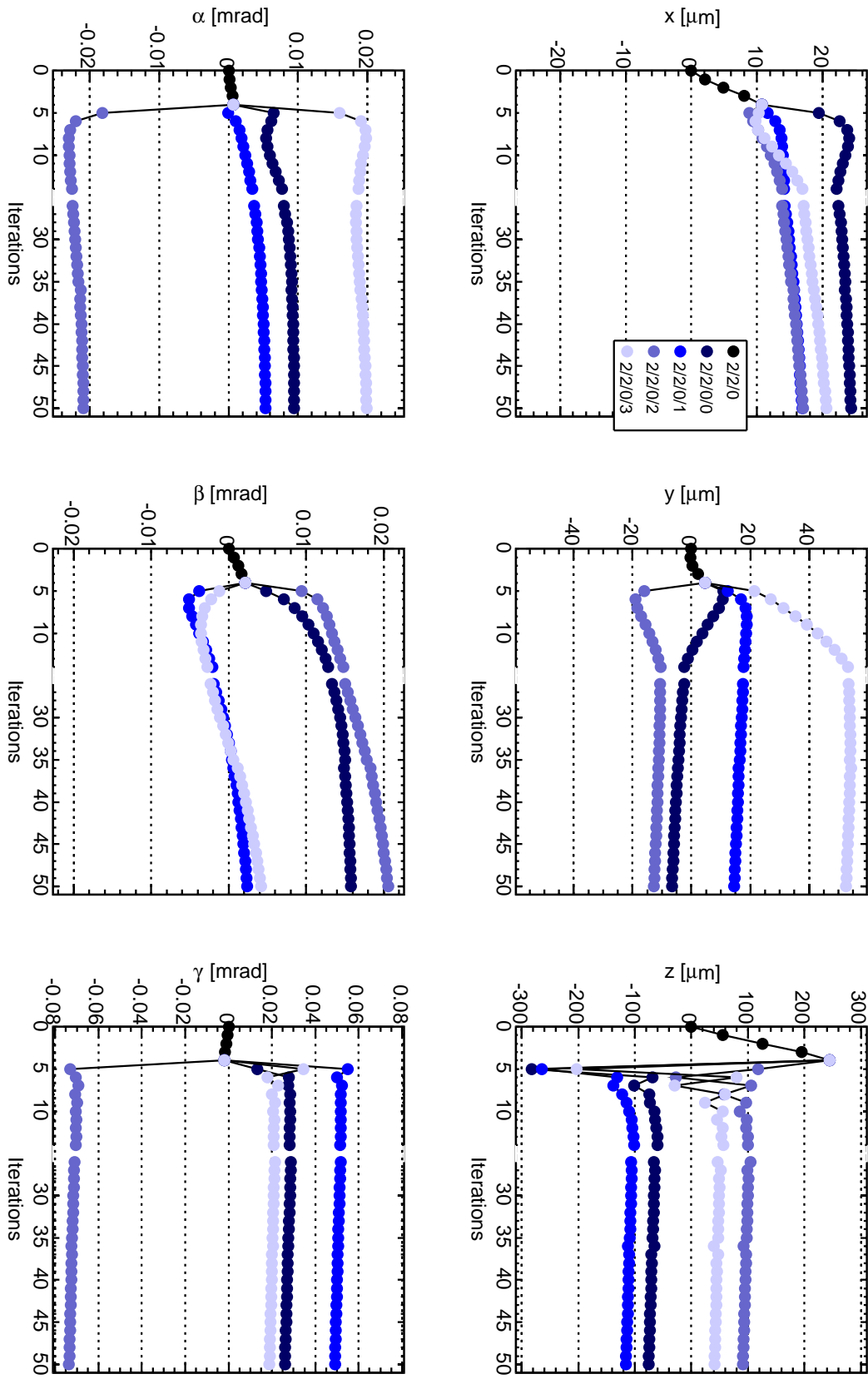
Figure 5.14: *Same as Figure 5.12, but for the SCT barrel as well as the individual barrel layers.*
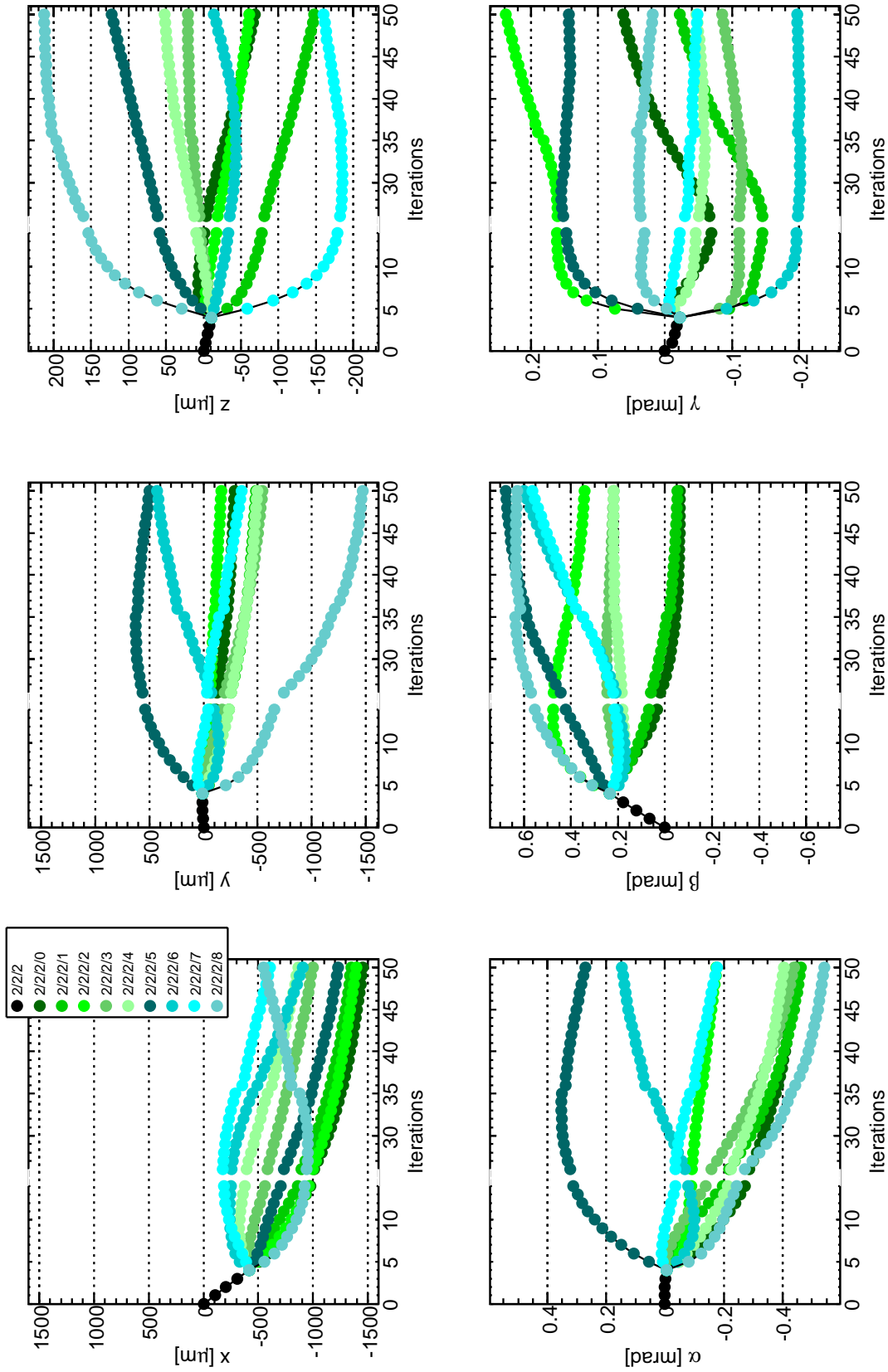
Figure 5.15: *Same as Figure 5.12, but for the SCT endcap A as well as the individual endcap A disks.*

Figure 5.12 shows the flow of the alignment parameters for the Pixel detector. It is apparent that the Pixel detector is initially very misaligned and that the Pixel barrel converges to stable alignment corrections for all degrees of freedom. The convergence of the Pixel endcap disks only happens during the final level 2 iterations. For the endcap disks it needs to be noted that x and β as well as y and α are highly correlated degrees of freedom. The rotation angles are defined in the global ATLAS coordinate frame centered at (0,0,0) and consequently even small rotations result in observable shifts due to the lever arm, i.e. the $|Z|$-position of an endcap disk. A more detailed investigation reveals that the endcap disk movements in x and y just offset the displacements stemming from the β and α rotations. The net effect of this is that the disks stay in place and are just slightly tilted, which is the desired alignment correction. The alignment corrections of the disks of Pixel endcap C are not fully convergent. The disks drift away in the global Z-direction.

In Figure 5.13 the flow of the alignment parameters for the SCT endcap C is shown. The same statement as for the Pixel endcap disks holds true for the SCT endcaps: x and β as well as y and α are correlated degrees of freedom due to the off-center rotations. Disk 6 is a special case, because, as will be discussed below, it had a noisy module that was not masked in the readout and contributed during the track reconstruction of the first 14 iterations. During the last 25 iterations the noisy module was not included in the track fitting. This is visible in the convergence behavior of the y and β alignment corrections of disk 6. Unfortunately, the noisy module still contributed to the pattern recognition and thus resulted in a increased number of fake tracks. This is likely the cause for the not-convergent behavior of the x and α alignment corrections of the adjacent disks 5 and 7. Also, disks 0, 1 and 3 drift away in the global Z-direction. For the other disks and the other degrees of freedom the alignment corrections are converging.

Figure 5.14 shows the flow of the alignment parameters of the SCT barrel. The alignment corrections for all degrees of freedom have converged to a degree where the level 2 structures only move by a few microns from iteration to iteration. It is unclear, why in the z-coordinate the *Local* χ^2 alignment at level 1 yields a positive alignment correction that is then offset by negative level 2 alignment corrections of the individual barrel layers. The not-convergent behavior of the y alignment correction of barrel layer 3 during the first 14 iterations is clearly gone during the final 25 iterations. This indicates that the not-convergent behavior was caused by the misalignment of individual modules which was corrected at level 3.

In Figure 5.15 the flow of the alignment parameters for the SCT endcap A is shown. All degrees of freedom for all nine endcap disks show a convergent behavior. It is very likely that the apparent drift of some degrees of freedom - like the global movement of endcap A in the X-direction (all disks but disk 8 move along the negative X-direction) - is caused by the misalignment of individual modules. The required level 3 alignment simply cannot be done with the available statistics of cosmic muons.

In general, the flow of the alignment parameters for the level 2 structures shows the convergence of the *Local* χ^2 alignment iterations. Only one endcap disk with a noisy SCT module and the two adjacent disks show a non-convergent behavior.

Residual distributions

Residual distributions of a perfectly aligned detector are centered at zero and have a width corresponding to the resolution of the specific readout coordinate and detector type. For Pixel x-residuals this would be a width of $14\,\mu$m, for y-residuals $115\,\mu$m and for SCT residuals $23\,\mu$m. Consequently, a necessary condition for a set of final alignment corrections is to produce centered and narrow residual distributions.

All of the following residual distributions were fitted with a Double-Gaussian, i.e. the sum of two Gaussians (cf. Equation 3.1). The Double-Gaussian was chosen to account for a superposition of a narrow core distribution of residuals from aligned modules and properly reconstructed tracks, and a broader tail distribution from outliers, noise hits, misreconstruction and not corrected misalignment.

The x- and y-residual distributions of the Pixel endcap disks and barrel layers without alignment corrections and with level 1 alignment corrections are shown in Figures 5.16 and 5.17, respectively. It is apparent that the residual distributions become centered but are still broad.

Even without alignment corrections applied, the SCT detector is prealigned. Level 1 alignment corrections for the SCT endcaps and level 1 and level 2 alignment corrections for the SCT barrel were obtained through survey measurements and previous cosmic runs and are already incorporated into the detector description of the SCT detector in the software framework Athena [83]. Consequently, the residual distributions of the SCT endcap disks and barrel layers with level 1 alignment corrections applied are not improved with respect to the distributions without alignment corrections. The residual distributions for the SCT endcap C and the SCT barrel are shown in Figures 5.18 and Figures 5.19. For the sake of brevity the corresponding Figure for endcap A is omitted. The distorted residual distribution of SCT endcap C disk 6 comes from a noisy module that was not masked in the readout or during track reconstruction.

In Tables 5.2 and 5.3 the fit results for the Pixel and SCT residual distributions with level 1 alignment corrections are listed. Because of the noisy module the fit results for SCT endcap C disk 6 are omitted in Table 5.3. For the Pixel detector the means of the fitted Gaussians are not centered, manifestly so for the barrel residual distributions. This means that the interpretation of the Double-Gaussian as a narrow core plus broad tails is not valid here. The fitted Gaussians for the SCT residual distributions are centered but much broader than the detector resolution. The broad residual distributions come from remaining misalignments that need to be corrected at alignment level 2 and level 3.
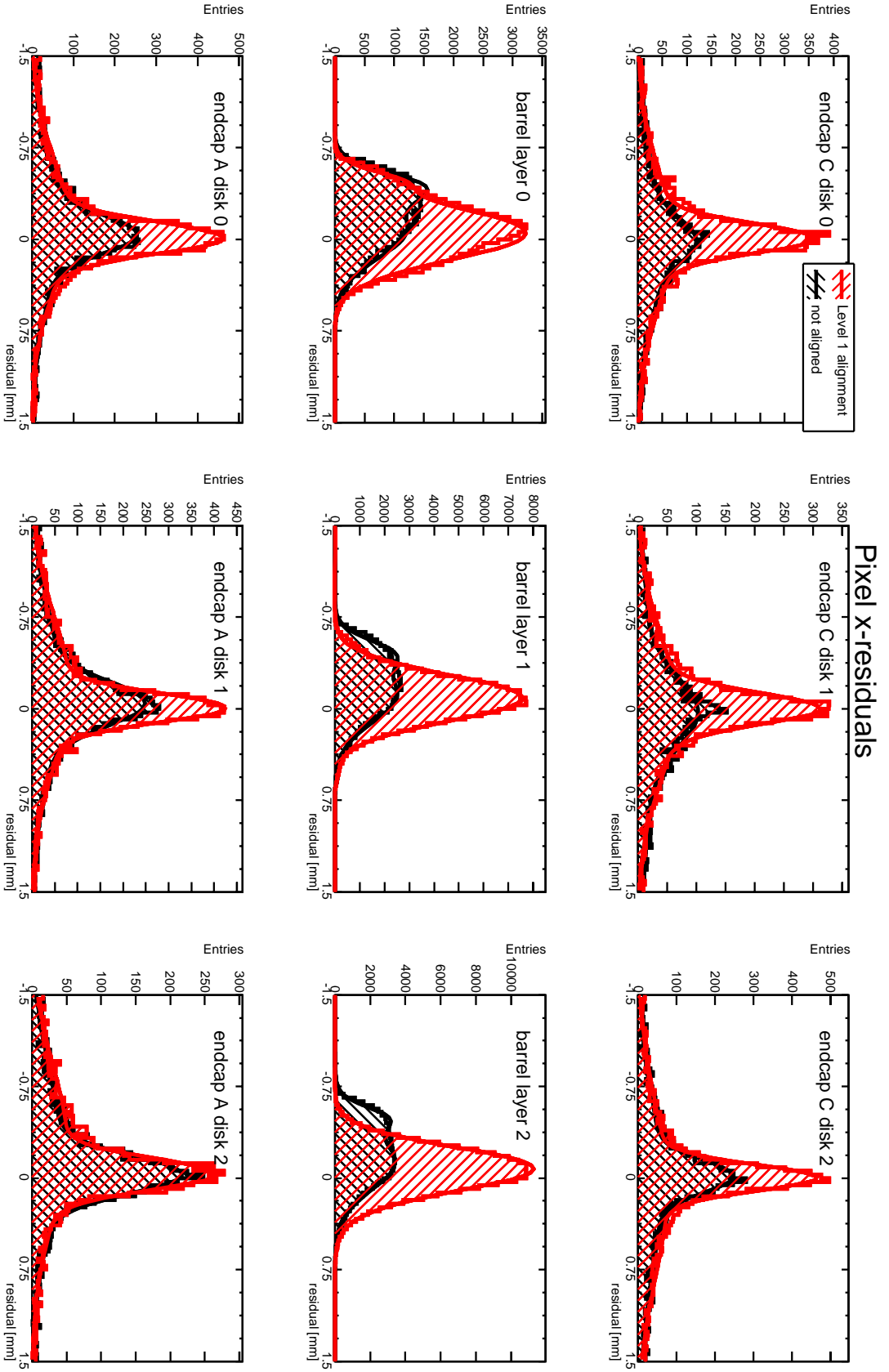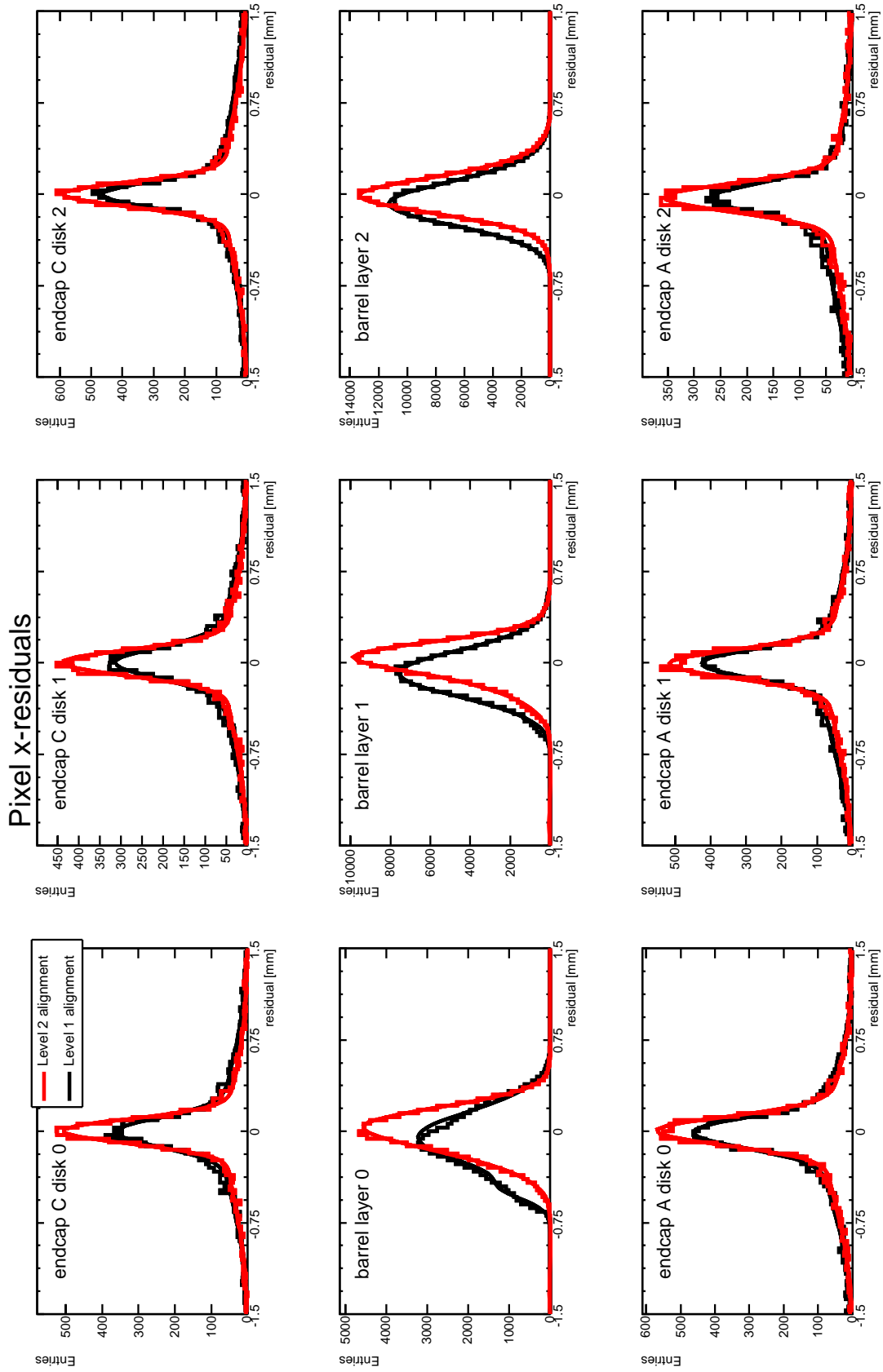
Figure 5.16: *Residual distributions for the short readout coordinate x, for the Pixel endcap disks and barrel layers without any alignment corrections and after level 1 alignment.*
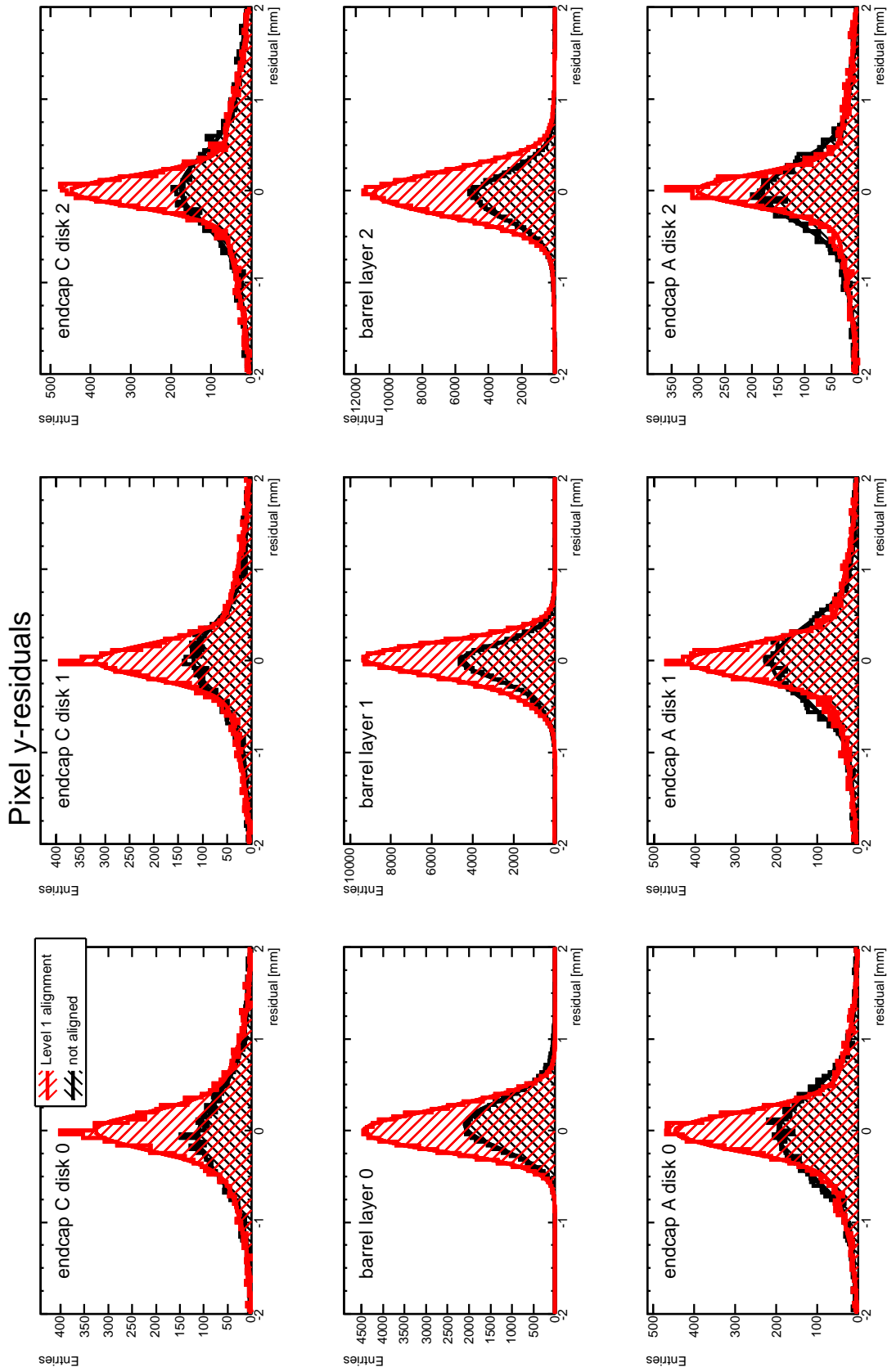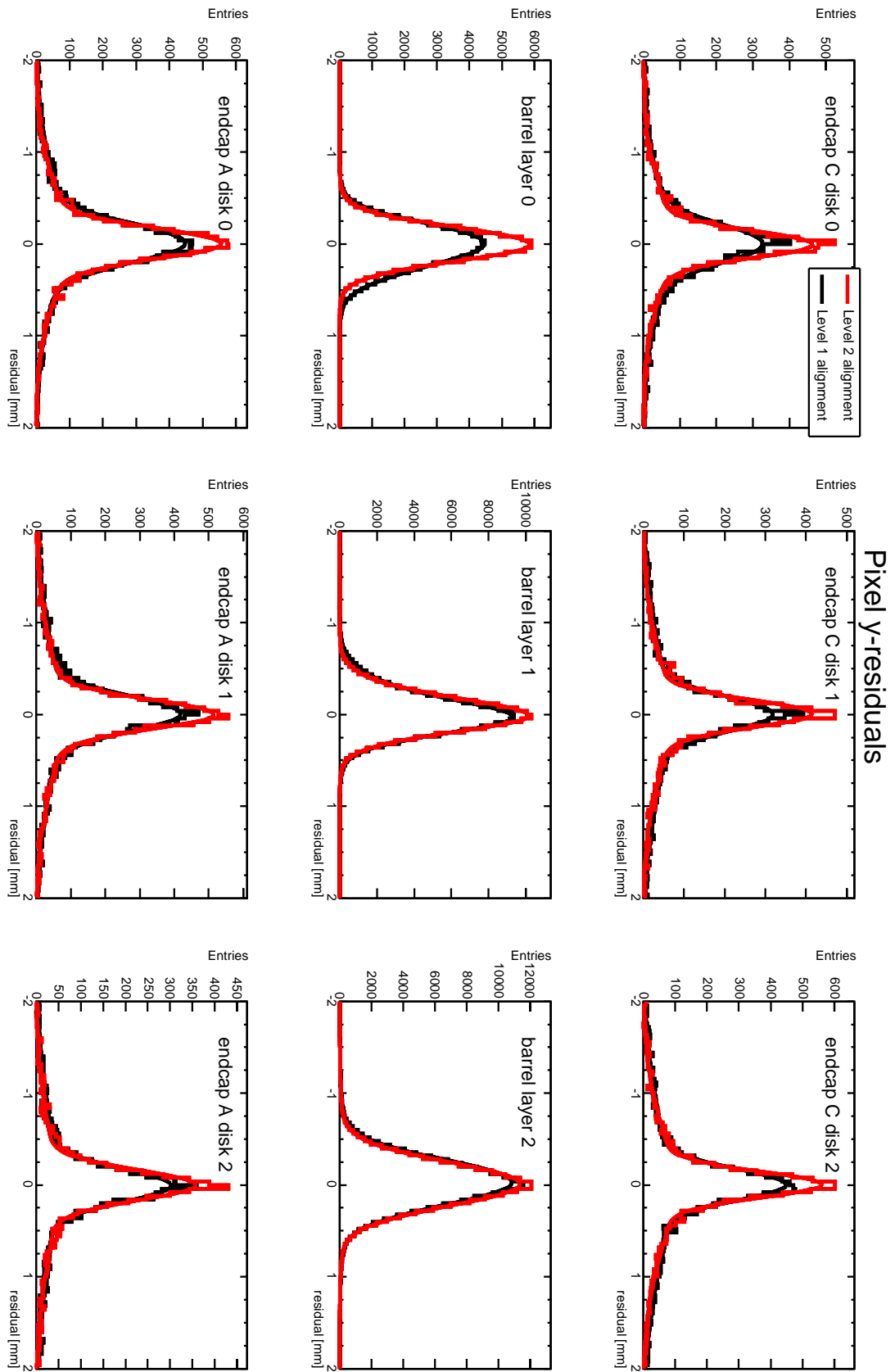
Figure 5.17: *Same as Figure 5.16, but for the long readout coordinate y.*
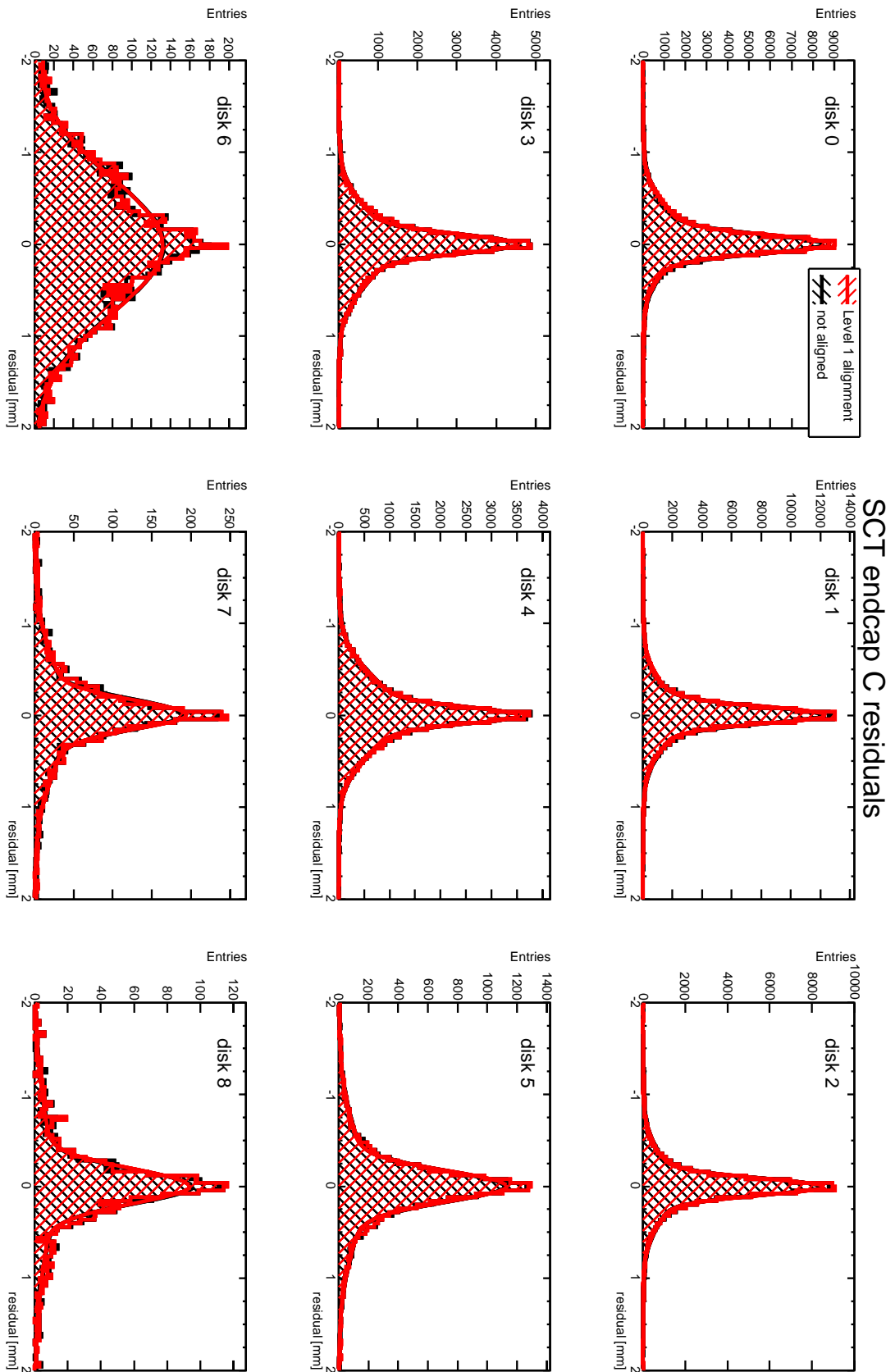
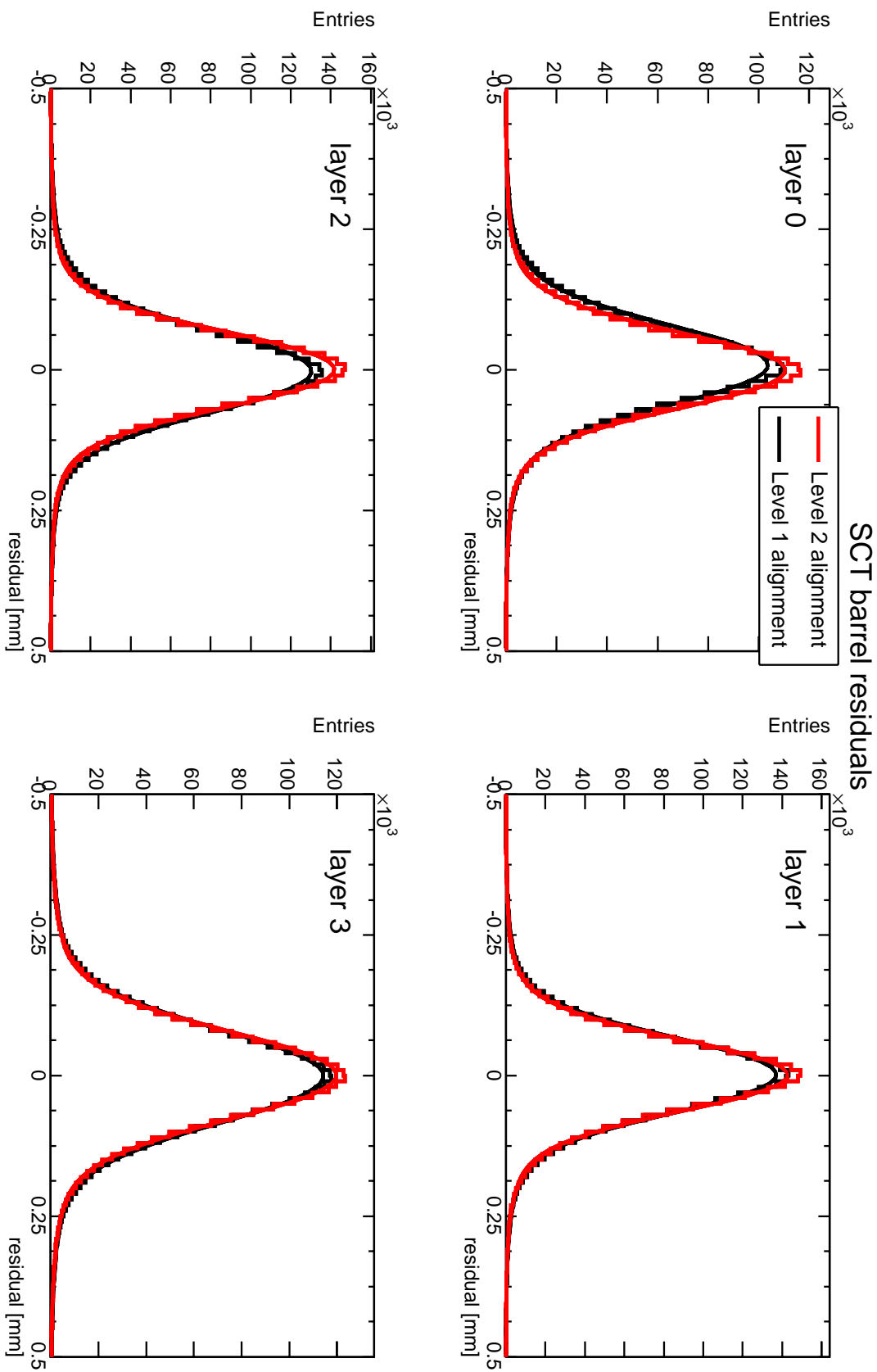Figure 5.18: *Same as Figure 5.16, but for the SCT endcap C disks.*
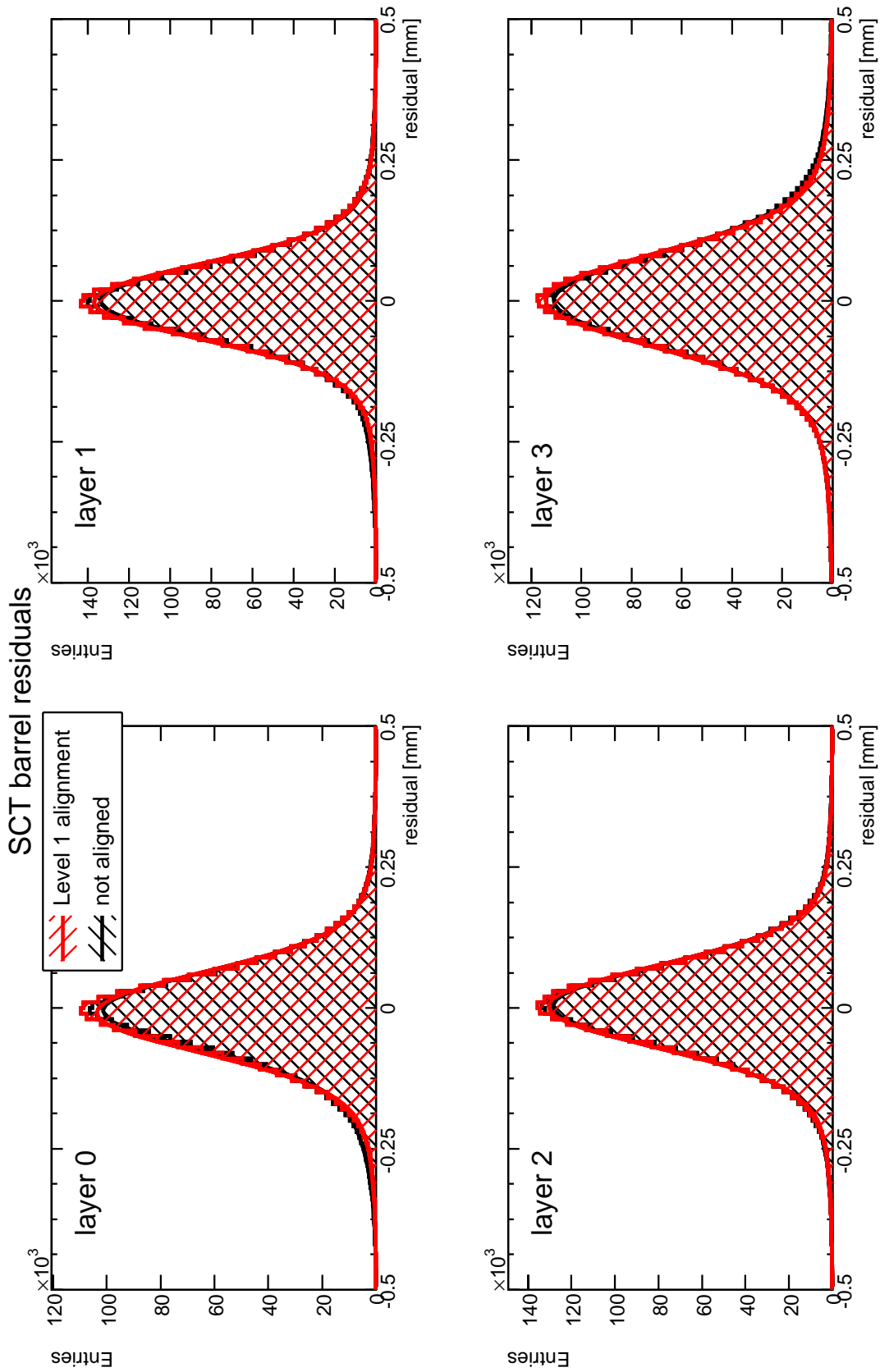
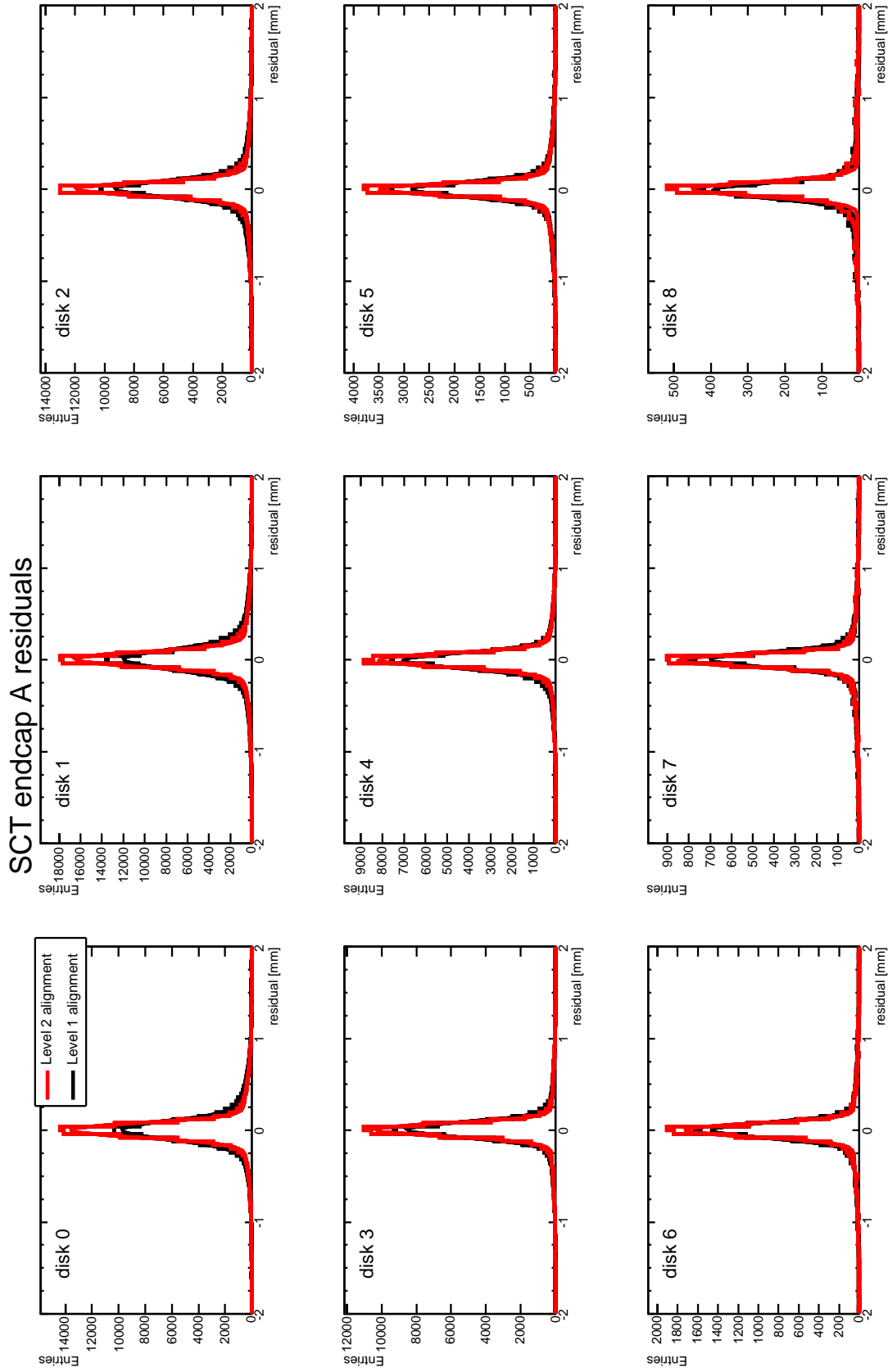Figure 5.19: *Same as Figure 5.16, but for the SCT barrel layers.*

Pixel residuals distributions with level 1 alignment corrections				
Pixel	fit parameters of Double-Gaussian [μm]			
Level 2 structure	$\mu_1 \pm$ error	$\sigma_1 \pm$ error	$\mu_2 \pm$ error	$\sigma_2 \pm$ error
Pixel x residuals				
endcap C disk 0	-6.7 ± 2.5	118.0 ± 3.7	-7.8 ± 9.4	560.9 ± 12.7
endcap C disk 1	0.4 ± 3.3	124.9 ± 4.3	-9.9 ± 8.7	593.8 ± 13.9
endcap C disk 2	-2.2 ± 2.4	106.7 ± 2.9	99.8 ± 9.7	705.8 ± 15.9
barrel layer 0	-480.9 ± 4.9	85.4 ± 2.4	-51.2 ± 1.5	219.8 ± 0.7
barrel layer 1	485.0 ± 10.0	88.7 ± 6.8	-87.4 ± 0.6	192.0 ± 0.5
barrel layer 2	-89.2 ± 2.4	173.2 ± 1.2	82.0 ± 31.9	209.8 ± 6.5
endcap A disk 0	-8.9 ± 2.7	125.8 ± 3.5	-129.1 ± 11.7	539.2 ± 12.3
endcap A disk 1	-5.0 ± 2.7	115.9 ± 2.9	-149.9 ± 10.7	600.2 ± 12.1
endcap A disk 2	-30.5 ± 3.8	125.0 ± 4.2	-293.4 ± 16.5	635.4 ± 19.9
Pixel y residuals				
endcap C disk 0	-4.6 ± 5.1	198.8 ± 7.1	10.4 ± 12.9	662.2 ± 16.9
endcap C disk 1	-2.4 ± 4.4	181.4 ± 5.3	44.2 ± 17.1	842.8 ± 19.9
endcap C disk 2	-3.5 ± 3.6	167.3 ± 4.1	87.7 ± 15.6	901.5 ± 19.1
barrel layer 0	-95.0 ± 9.3	162.5 ± 7.1	52.7 ± 4.0	239.0 ± 1.4
barrel layer 1	46.4 ± 1.7	160.7 ± 1.7	-82.9 ± 2.7	269.9 ± 1.4
barrel layer 2	-28.0 ± 0.7	244.7 ± 0.7	-77.9 ± 8.1	685.0 ± 12.4
endcap A disk 0	-8.3 ± 4.0	205.6 ± 4.7	-80.0 ± 14.3	742.3 ± 17.8
endcap A disk 1	-7.6 ± 3.8	188.7 ± 4.4	-18.4 ± 16.5	856.4 ± 21.2
endcap A disk 2	5.2 ± 4.2	176.1 ± 5.0	3.4 ± 21.2	896.4 ± 29.5

Table 5.2: *Fit results of the Pixel residual distributions for the local x and y coordinates with level 1 alignment corrections. The columns μ_1 and σ_1 list the fit results of the narrow core Gaussians and the columns μ_2 and σ_2 list the fit results of the broad tail Gaussians, all quoted together with the statistical uncertainty taken as the one standard deviation parameter error of the fit.*

SCT residuals distributions with level 1 alignment corrections				
SCT	fit parameters of Double-Gaussian [μm]			
Level 2 structure	$\mu_1 \pm$ error	$\sigma_1 \pm$ error	$\mu_2 \pm$ error	$\sigma_2 \pm$ error
endcap C disk 0	-1.2 ± 0.7	96.1 ± 0.8	-83.2 ± 1.9	338.9 ± 2.2
endcap C disk 1	-2.8 ± 0.5	90.8 ± 0.7	9.9 ± 1.6	338.7 ± 2.4
endcap C disk 2	3.8 ± 0.6	91.4 ± 0.9	20.5 ± 2.0	345.6 ± 3.5
endcap C disk 3	-5.0 ± 1.1	100.1 ± 1.5	22.4 ± 2.4	390.4 ± 2.9
endcap C disk 4	0.3 ± 1.2	88.7 ± 1.7	-18.0 ± 2.5	397.6 ± 2.7
endcap C disk 5	-1.0 ± 2.2	164.2 ± 3.2	8.2 ± 8.1	629.6 ± 11.8
endcap C disk 6				
endcap C disk 7	-6.8 ± 5.6	151.3 ± 9.3	16.0 ± 16.8	595.8 ± 25.3
endcap C disk 8	-0.9 ± 7.4	184.9 ± 8.9	-19.0 ± 41.3	808.5 ± 55.5
barrel layer 0	-8.3 ± 0.1	69.4 ± 0.2	-12.2 ± 0.3	140.1 ± 0.7
barrel layer 1	-1.4 ± 0.1	65.0 ± 0.1	3.5 ± 0.3	135.9 ± 0.6
barrel layer 2	2.5 ± 0.1	71.3 ± 0.1	-6.4 ± 0.3	154.8 ± 0.6
barrel layer 3	0.9 ± 0.1	80.9 ± 0.1	-1.1 ± 0.3	183.2 ± 0.6
endcap A disk 0	1.1 ± 0.5	100.2 ± 0.7	73.3 ± 2.8	403.8 ± 4.4
endcap A disk 1	4.5 ± 0.5	108.7 ± 0.6	48.5 ± 3.0	475.3 ± 5.5
endcap A disk 2	5.4 ± 0.5	90.3 ± 0.6	-14.9 ± 3.3	448.7 ± 5.8
endcap A disk 3	6.0 ± 0.4	81.9 ± 0.5	0.2 ± 4.7	467.5 ± 8.5
endcap A disk 4	-8.5 ± 0.5	82.6 ± 0.6	-24.7 ± 4.2	391.1 ± 8.2
endcap A disk 5	0.1 ± 0.8	82.4 ± 0.9	-17.1 ± 7.7	526.1 ± 12.7
endcap A disk 6	-0.7 ± 1.1	81.8 ± 1.1	-23.2 ± 12.3	555.4 ± 18.9
endcap A disk 7	1.6 ± 1.5	82.2 ± 1.7	-17.1 ± 22.1	682.1 ± 33.1
endcap A disk 8	-10.9 ± 2.1	84.5 ± 2.4	-65.5 ± 26.9	650.5 ± 35.4

Table 5.3: *Same as Table 5.2, but for the SCT residual distributions.*

Figures 5.20 and 5.21 show the Pixel x- and y-residual distributions with level 1 and level 2 alignment corrections applied. Clearly the level 2 alignment corrections improve the residual distributions significantly. Still, the residual distributions are too broad and for the Pixel x-residuals not even centered.

The residual distributions with level 2 alignment corrections for the SCT endcap C, the SCT barrel and the SCT endcap A are shown in Figures 5.22 - 5.24. The improvements of the SCT endcap residual distributions are clearly visible, whereas the improvements for the SCT barrel residual distributions are barely visible because it is already prealigned at level 2.

In Tables 5.4 and 5.5 the fit results for all the residual distributions with level 2 alignment corrections are listed. As for the level 1 alignment, the fitted Pixel barrel Gaussians are not centered, thus defying a clear interpretation as core and tail distributions. For the Pixel endcaps the fitted core Gaussians are centered and the width thus gives an indication of the size of the not corrected random level 3 misalignments. For the Pixel endcap modules this random level 3 misalignment seems to be of the order of $100\,\mu$m. As, due to too low statistics, the Pixel endcaps were not aligned at level 3 this result will only improve indirectly through better Pixel and SCT barrel alignment and the subsequent final level 2 alignment.

For the SCT detector all fitted core Gaussians are centered, so the their width is an indication of the not corrected random level 3 misalignments as well. The SCT endcaps were not aligned at level 3, again for reasons of too low statistics, but the remaining random level 3 misalignments are significantly less than $100\,\mu$m.

Figure 5.20: *Residual distributions for the short readout coordinate x, for the Pixel endcap disks and barrel layers with level 1 alignment corrections and after level 2 alignment.*

Figure 5.21: *Same as Figure 5.20, but for the long readout coordinate y.*
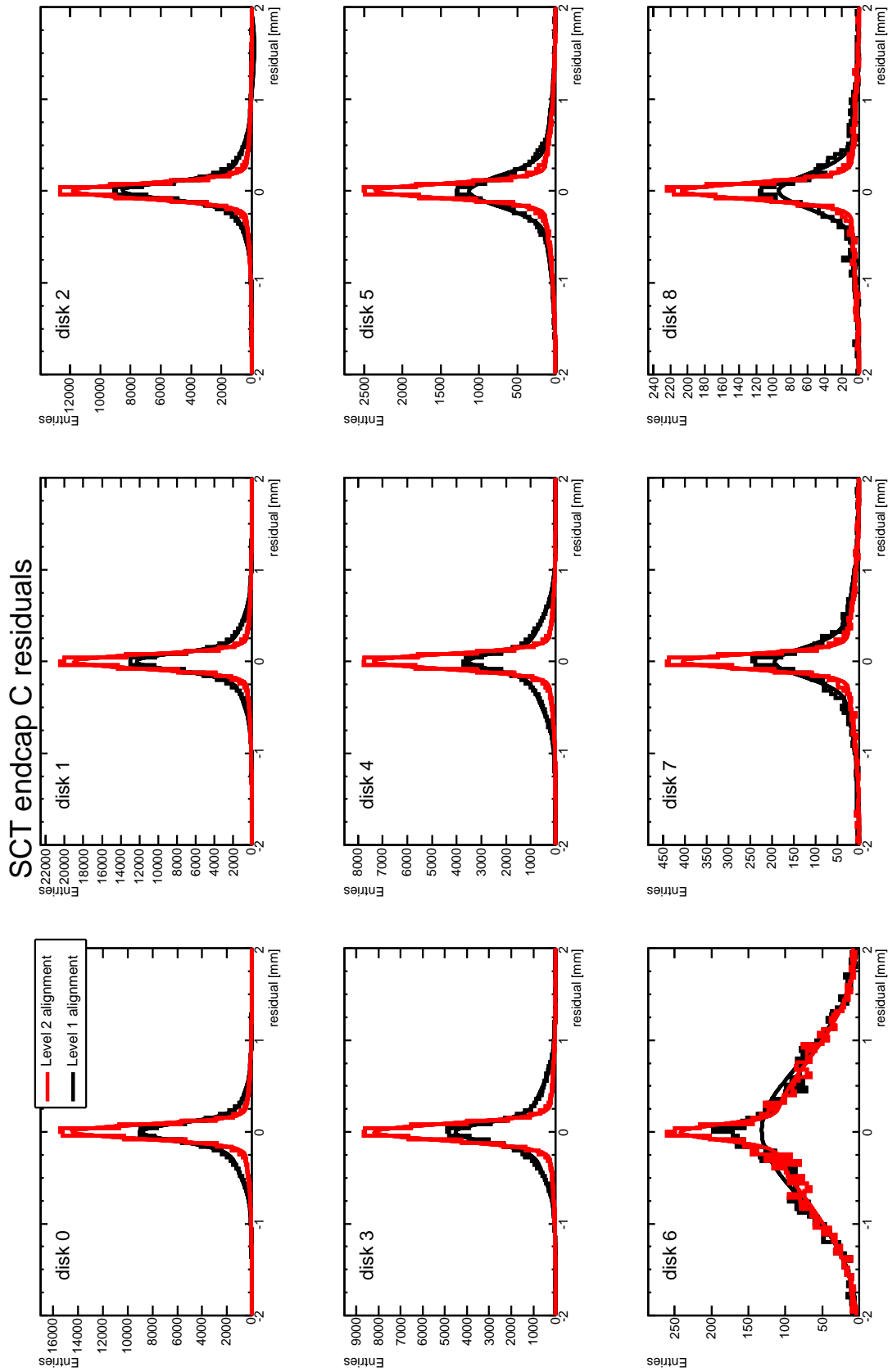
Figure 5.22: *Same as Figure 5.20, but for the SCT endcap C disks.*

Figure 5.23: *Same as Figure 5.20, but for the SCT barrel layers.*

Figure 5.24: *Same as Figure 5.20, but for the SCT endcap A disks.*

Pixel residuals distributions with level 2 alignment corrections				
Pixel	fit parameters of Double-Gaussian [μm]			
Level 2 structure	$\mu_1 \pm$ error	$\sigma_1 \pm$ error	$\mu_2 \pm$ error	$\sigma_2 \pm$ error
Pixel x residuals				
endcap C disk 0	1.6 ± 2.1	99.5 ± 2.2	-71.2 ± 11.5	527.4 ± 12.4
endcap C disk 1	0.5 ± 2.3	106.8 ± 2.4	-3.4 ± 11.9	567.9 ± 13.5
endcap C disk 2	-0.1 ± 1.9	99.6 ± 2.0	59.5 ± 11.3	631.7 ± 14.0
barrel layer 0	82.7 ± 3.2	134.7 ± 3.0	-57.2 ± 5.8	192.3 ± 1.4
barrel layer 1	60.6 ± 1.1	108.1 ± 1.0	-33.7 ± 1.4	196.5 ± 0.8
barrel layer 2	-19.2 ± 1.3	130.7 ± 1.5	27.8 ± 1.6	198.4 ± 1.5
endcap A disk 0	4.1 ± 2.1	115.4 ± 2.2	-115.6 ± 10.6	531.9 ± 11.5
endcap A disk 1	-8.1 ± 2.2	115.0 ± 2.4	-83.5 ± 11.1	588.6 ± 13.4
endcap A disk 2	-26.0 ± 2.6	115.5 ± 2.9	-132.2 ± 14.7	617.4 ± 19.5
Pixel y residuals				
endcap C disk 0	4.6 ± 3.2	143.6 ± 4.0	-24.7 ± 12.0	613.0 ± 15.8
endcap C disk 1	-7.2 ± 3.3	145.3 ± 4.2	11.0 ± 14.1	702.7 ± 16.3
endcap C disk 2	-3.8 ± 2.8	139.2 ± 3.4	39.8 ± 11.9	721.2 ± 13.4
barrel layer 0	3.6 ± 0.9	185.2 ± 1.3	-42.3 ± 13.2	346.2 ± 29.7
barrel layer 1	31.2 ± 2.7	157.2 ± 2.9	-44.5 ± 2.7	235.9 ± 2.1
barrel layer 2	-10.2 ± 0.6	235.8 ± 0.6	-65.5 ± 7.8	655.7 ± 11.2
endcap A disk 0	-3.7 ± 3.1	162.2 ± 3.6	-32.2 ± 11.4	640.1 ± 12.5
endcap A disk 1	-0.7 ± 3.0	157.1 ± 3.5	19.0 ± 13.6	740.9 ± 16.7
endcap A disk 2	1.6 ± 3.6	161.8 ± 4.4	89.3 ± 18.4	760.8 ± 23.6

Table 5.4: *Same as Table 5.2, but for the Pixel residual distributions with level 2 alignment corrections.*
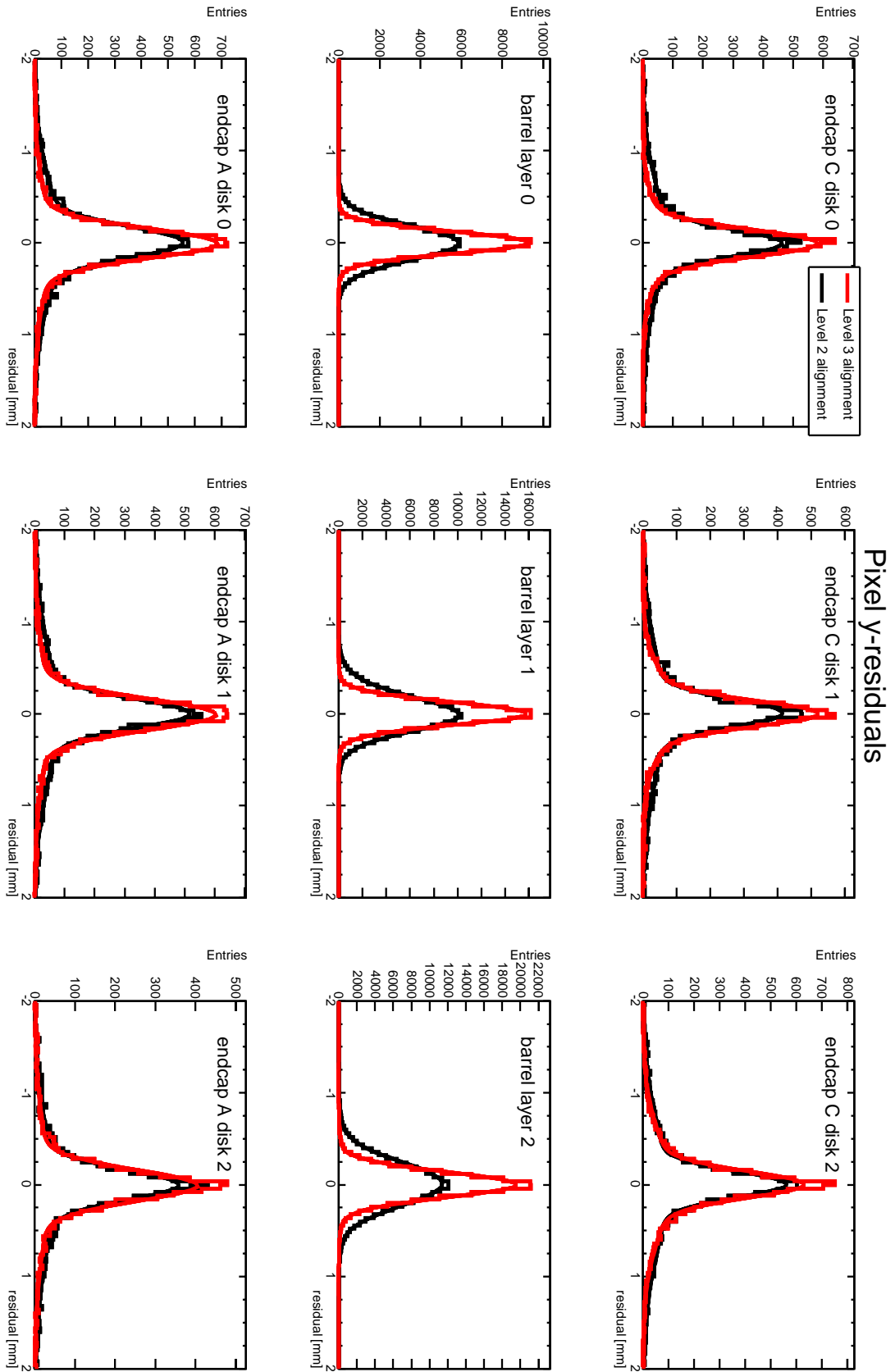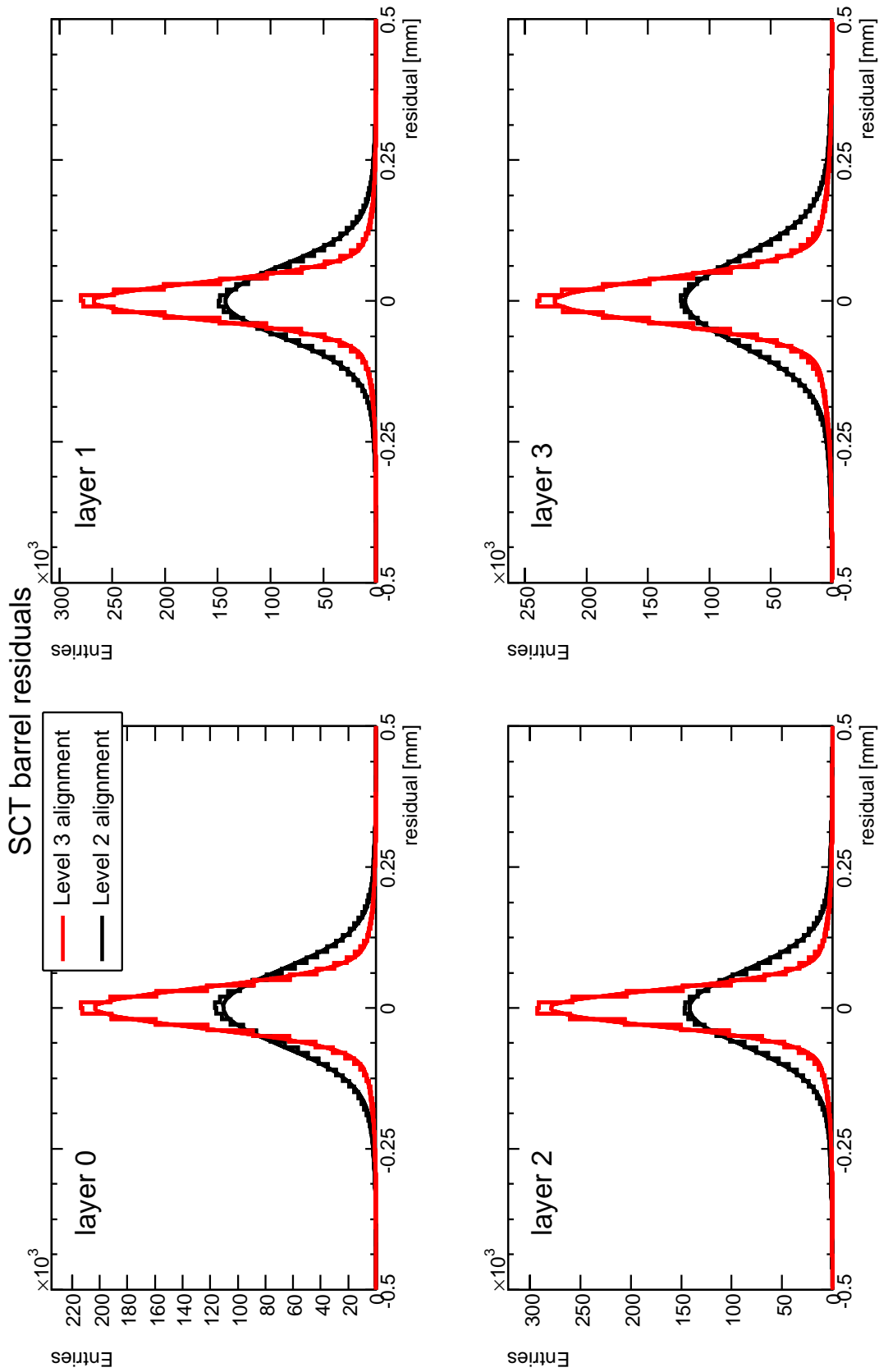
SCT residuals distributions with level 2 alignment corrections				
SCT	fit parameters of Double-Gaussian [μm]			
Level 2 structure	$\mu_1 \pm$ error	$\sigma_1 \pm$ error	$\mu_2 \pm$ error	$\sigma_2 \pm$ error
endcap C disk 0	1.4 ± 0.3	73.1 ± 0.3	-21.3 ± 3.5	423.0 ± 5.8
endcap C disk 1	-2.9 ± 0.3	75.1 ± 0.3	-9.3 ± 3.7	476.8 ± 6.3
endcap C disk 2	-0.1 ± 0.4	81.9 ± 0.4	-8.8 ± 4.5	507.5 ± 7.5
endcap C disk 3	-2.6 ± 0.4	86.9 ± 0.5	-4.9 ± 5.6	505.5 ± 8.0
endcap C disk 4	-0.5 ± 0.5	78.4 ± 0.5	-10.8 ± 5.1	442.9 ± 7.2
endcap C disk 5	1.4 ± 0.9	78.9 ± 0.9	5.5 ± 8.2	602.9 ± 9.3
endcap C disk 6				
endcap C disk 7	-1.0 ± 2.1	-79.9 ± 2.4	15.0 ± 18.6	602.5 ± 21.8
endcap C disk 8	-0.6 ± 2.9	88.5 ± 3.0	-23.8 ± 40.8	774.7 ± 49.2
barrel layer 0	0.7 ± 0.1	66.1 ± 0.1	-2.1 ± 0.3	142.2 ± 0.7
barrel layer 1	-0.9 ± 0.1	62.1 ± 0.1	5.0 ± 0.2	131.7 ± 0.6
barrel layer 2	-0.5 ± 0.1	65.8 ± 0.1	-1.1 ± 0.3	154.7 ± 0.6
barrel layer 3	-0.5 ± 0.1	77.1 ± 0.1	-2.0 ± 0.3	180.8 ± 0.6
endcap A disk 0	0.2 ± 0.3	75.0 ± 0.4	63.1 ± 3.2	422.1 ± 4.7
endcap A disk 1	4.9 ± 0.3	80.2 ± 0.4	37.3 ± 3.3	474.8 ± 5.6
endcap A disk 2	3.3 ± 0.3	74.0 ± 0.4	20.1 ± 4.3	519.8 ± 7.9
endcap A disk 3	5.0 ± 0.3	68.4 ± 0.4	10.4 ± 5.4	490.5 ± 8.7
endcap A disk 4	-4.4 ± 0.5	72.8 ± 0.4	10.3 ± 5.0	431.9 ± 7.8
endcap A disk 5	-0.1 ± 0.6	65.7 ± 0.7	-14.8 ± 6.2	449.3 ± 10.4
endcap A disk 6	0.6 ± 0.9	68.6 ± 0.9	-35.0 ± 11.7	515.2 ± 22.7
endcap A disk 7	-5.9 ± 1.2	67.2 ± 1.3	-5.6 ± 18.2	559.9 ± 39.6
endcap A disk 8	1.3 ± 1.7	69.0 ± 1.8	-27.6 ± 25.0	588.6 ± 30.5

Table 5.5: *Same as Table 5.2, but for the SCT residual distributions with level 2 alignment corrections.*

Figures 5.25 and 5.26 show the Pixel x- and y-residual distributions with level 2 alignment corrections applied for the endcaps and level 3 alignment corrections applied for the barrel. The Pixel barrel residual distributions show a significant improvement. The Pixel endcap distributions are slightly improved due to the level 3 alignment corrections of the Pixel and SCT barrel.

In Figure 5.27 the residual distributions of the SCT barrel with level 3 alignment corrections are shown. The improvements are clearly visible. Tables 5.6 and 5.7 list the fit results for the Pixel and SCT barrel residual distributions. The fitted Gaussians are centered now and the width of the core Gaussian approaches the detector resolution. The difference of the fitted width to the intrinsic detector resolution can be attributed to not fully corrected random level 3 misalignments and the influence of the misaligned endcaps.

Pixel residuals distributions with level 3 alignment corrections				
Pixel	fit parameters of Double-Gaussian [μm]			
Level 2 structure	$\mu_1 \pm$ error	$\sigma_1 \pm$ error	$\mu_2 \pm$ error	$\sigma_2 \pm$ error
Pixel x residuals				
barrel layer 0	1.2 ± 0.2	37.2 ± 0.3	-3.7 ± 1.1	123.8 ± 2.7
barrel layer 1	-7.9 ± 0.0	47.2 ± 498.9	5.8 ± 0.0	51.6 ± 0.1
barrel layer 2	-0.0 ± 0.1	41.8 ± 0.3	-0.5 ± 0.7	127.5 ± 1.7
Pixel y residuals				
barrel layer 0	-0.2 ± 0.5	117.9 ± 0.4	-25.2 ± 15.3	387.1 ± 25.8
barrel layer 1	-0.3 ± 0.4	124.7 ± 0.3	-14.9 ± 10.1	407.7 ± 15.2
barrel layer 2	-0.5 ± 0.4	137.6 ± 0.4	0.7 ± 5.0	418.1 ± 9.3

Table 5.6: *Same as Table 5.2, but for the Pixel residual distributions with level 3 alignment corrections. Statistical uncertainties quoted as 0.0 are smaller than 0.05.*

SCT residuals distributions with level 3 alignment corrections				
SCT	fit parameters of Double-Gaussian [μm]			
Level 2 structure	$\mu_1 \pm$ error	$\sigma_1 \pm$ error	$\mu_2 \pm$ error	$\sigma_2 \pm$ error
barrel layer 0	-0.1 ± 0.0	34.8 ± 0.0	-1.8 ± 0.2	103.1 ± 0.4
barrel layer 1	-0.0 ± 0.0	32.1 ± 0.0	-0.7 ± 0.2	94.1 ± 0.3
barrel layer 2	-0.2 ± 0.0	31.3 ± 0.0	-0.8 ± 0.2	102.0 ± 0.4
barrel layer 3	0.0 ± 0.0	38.7 ± 0.0	-0.2 ± 0.2	143.4 ± 0.4

Table 5.7: *Same as Table 5.2, but for the SCT residual distributions with level 3 alignment corrections. Statistical uncertainties quoted as 0.0 are smaller than 0.05.*
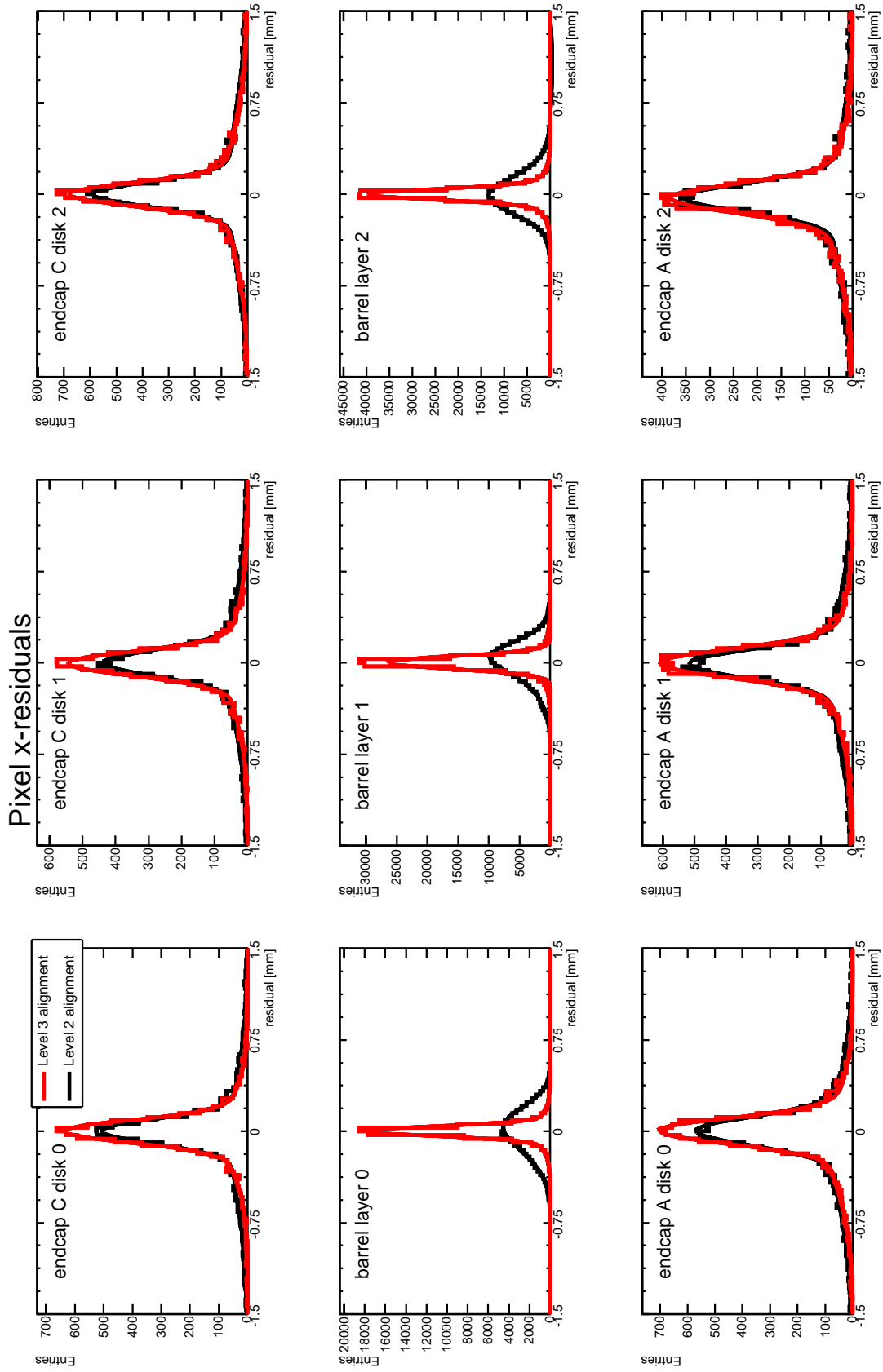
Figure 5.25: *Residual distributions for the short readout coordinate x, for the Pixel endcap disks and barrel layers with level 2 alignment corrections and after level 3 alignment of the barrel modules.*

Figure 5.26: *Same as Figure 5.25, but for the long readout coordinate y.*

Figure 5.27: *Same as Figure 5.25, but for the SCT barrel layers.*

The improvement of the residual distributions due to the final level 2 alignment are only minor. Figure 5.28 shows the Pixel x-residual distributions as an example. The improvement of the Pixel endcap residual distributions is visible. It is caused by the now aligned SCT barrel modules which completely enclose the Pixel endcaps.

A big improvement of the residual distribution can be seen in Figure 5.29 for the SCT endcap C disk 6. For this disk the noisy module was removed from the track fitting during the final 25 level 2 iterations. The reduction in the noise level of this disk is apparent. Still, the overall noise level of this disk is high compared to the other disks. It is unclear whether this comes from an increased number of fake tracks (generated by the noisy module, which still contributed to the pattern recognition) or from a genuine defect of the DAQ of this disk.

Tables 5.8 and 5.9 list the fit results for all residual distributions after the final alignment corrections. All narrow core Gaussians are centered and their width can thus be used to infer the size of the remaining random level 3 misalignments. Upper bounds for these not corrected random level 3 misalignments for the barrel are $40\,\mu$m for the local Pixel x-direction, $60\,\mu$m for the local Pixel y-direction and $25\,\mu$m for the SCT modules. These numbers are estimated by assuming that the σ_1 fit parameter of the residual distributions comes from the remaining level 3 misalignments and the intrinsic detector resolution added in quadrature.

For the Pixel endcap modules this random level 3 misalignment is now below $100\,\mu$m. For the SCT endcaps the remaining random level 3 misalignments are significantly less than $100\,\mu$m, about $70\,\mu$m for endcap C and about $60\,\mu$m for endcap A.

The fact that the Pixel x-residual distributions are wider than the SCT residual distribution (for the barrel and for the endcaps) can be attributed to a known software defect in the Pixel cluster reconstruction in Athena 14.5.0 [84].
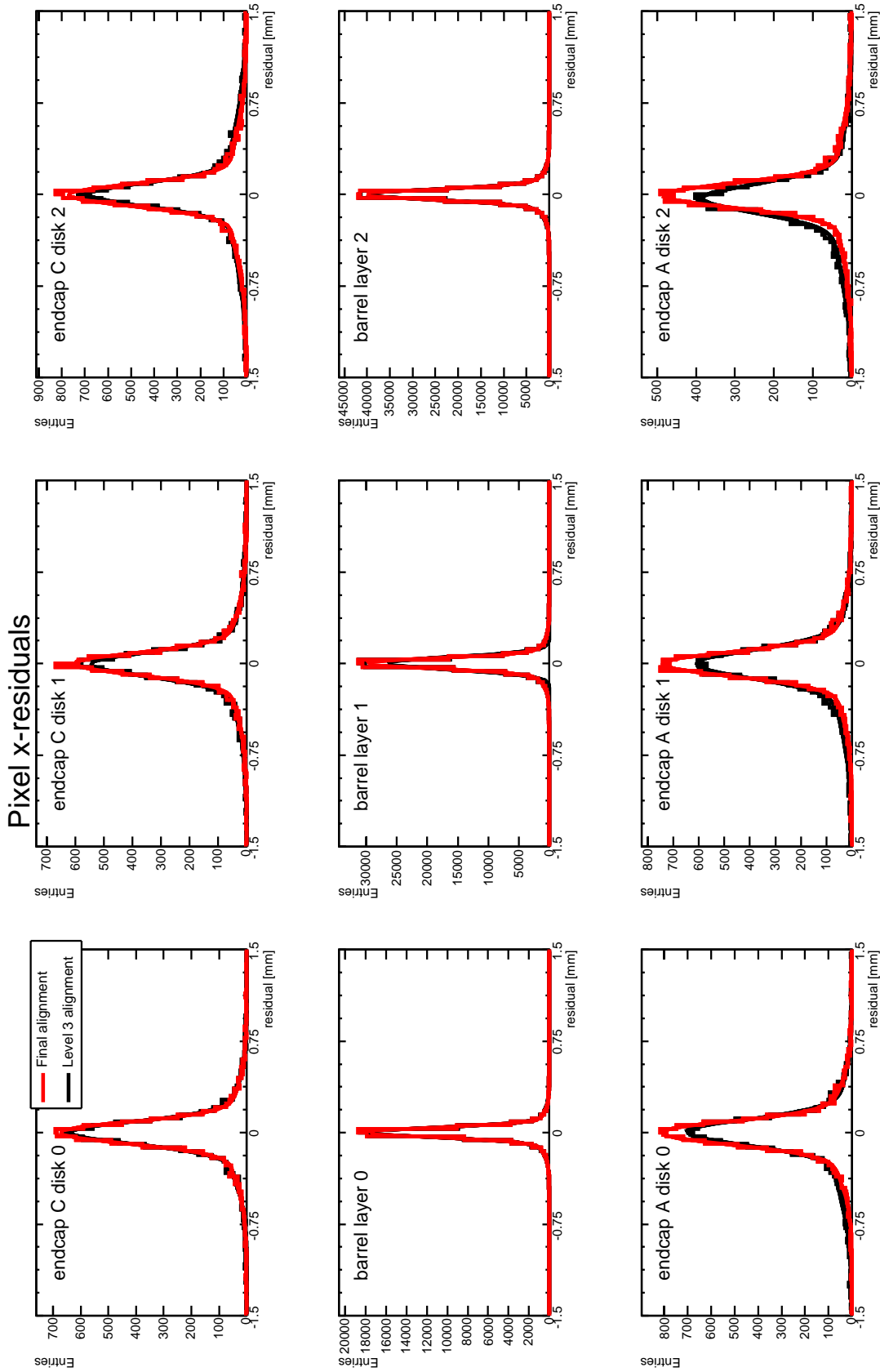
Figure 5.28: *Residual distributions for the short readout coordinate x, for the Pixel endcap disks and barrel layers. Level 3 alignment denotes a set of alignment corrections with preliminary level 2 alignment of the endcap disks and level 3 alignment of the barrel modules. Final alignment denotes the set of alignment corrections with final level 2 alignment of the endcap disks (after 50 iterations) and level 3 alignment of the barrel modules.*
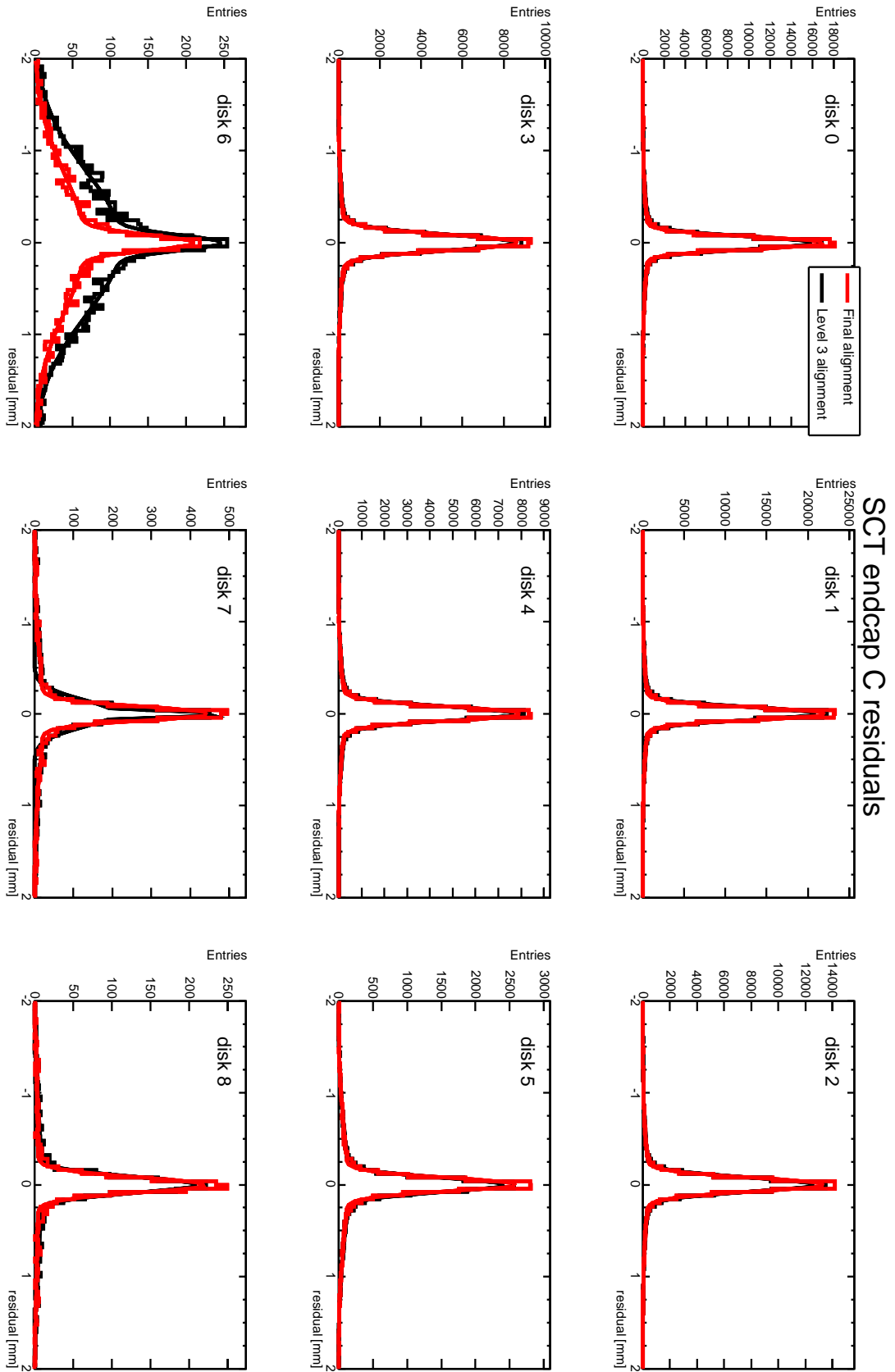
Figure 5.29: *Same as Figure 5.28, but for the SCT endcap C disks.*

Pixel residuals distributions with final alignment corrections				
Pixel	fit parameters of Double-Gaussian [μm]			
Level 2 structure	$\mu_1 \pm$ error	$\sigma_1 \pm$ error	$\mu_2 \pm$ error	$\sigma_2 \pm$ error
Pixel x residuals				
endcap C disk 0	-0.3 ± 1.6	86.5 ± 1.9	-37.3 ± 8.1	323.7 ± 9.5
endcap C disk 1	-1.5 ± 1.8	90.1 ± 2.1	-0.4 ± 8.4	358.7 ± 11.3
endcap C disk 2	-3.7 ± 1.5	90.7 ± 1.8	-0.6 ± 8.3	444.5 ± 11.4
barrel layer 0	1.3 ± 0.2	37.4 ± 0.3	-4.1 ± 1.1	124.1 ± 3.1
barrel layer 1	1.2 ± 0.2	40.1 ± 0.3	-2.8 ± 0.8	123.3 ± 2.3
barrel layer 2	-0.2 ± 0.1	41.8 ± 0.3	-0.2 ± 0.7	127.5 ± 1.8
endcap A disk 0	-1.5 ± 1.6	92.4 ± 1.8	-6.5 ± 6.5	319.6 ± 8.6
endcap A disk 1	-3.5 ± 1.6	98.4 ± 1.9	7.3 ± 8.1	370.4 ± 12.5
endcap A disk 2	-6.8 ± 2.0	99.0 ± 2.1	23.2 ± 11.7	462.4 ± 15.4
Pixel y residuals				
endcap C disk 0	-0.7 ± 2.5	137.4 ± 3.3	4.4 ± 11.3	405.6 ± 17.2
endcap C disk 1	-2.5 ± 3.5	130.9 ± 4.7	-5.5 ± 9.0	390.4 ± 15.8
endcap C disk 2	-5.3 ± 2.4	151.7 ± 3.4	-10.7 ± 12.5	598.9 ± 21.0
barrel layer 0	-0.4 ± 0.5	117.7 ± 0.4	-10.2 ± 14.6	378.2 ± 24.6
barrel layer 1	-0.4 ± 0.4	124.5 ± 0.3	-14.6 ± 10.8	412.1 ± 15.8
barrel layer 2	-0.9 ± 0.4	137.0 ± 0.4	0.1 ± 4.9	402.9 ± 9.4
endcap A disk 0	-1.8 ± 2.4	141.9 ± 3.4	-26.1 ± 9.3	396.1 ± 15.9
endcap A disk 1	-1.1 ± 2.5	149.4 ± 3.3	-22.7 ± 11.1	475.1 ± 17.7
endcap A disk 2	0.7 ± 2.9	157.7 ± 4.5	-54.7 ± 20.0	619.4 ± 44.8

Table 5.8: *Same as Table 5.2, but for the Pixel residual distributions with final alignment corrections.*

SCT residuals distributions with final alignment corrections				
SCT	fit parameters of Double-Gaussian [μm]			
Level 2 structure	$\mu_1 \pm$ error	$\sigma_1 \pm$ error	$\mu_2 \pm$ error	$\sigma_2 \pm$ error
endcap C disk 0	1.8 ± 0.3	64.3 ± 0.3	-3.6 ± 4.0	438.9 ± 6.7
endcap C disk 1	-1.3 ± 0.2	65.4 ± 0.2	0.6 ± 3.7	445.3 ± 6.6
endcap C disk 2	-1.0 ± 0.3	74.1 ± 0.3	-7.0 ± 4.6	483.6 ± 7.4
endcap C disk 3	-2.0 ± 0.4	83.2 ± 0.4	-8.2 ± 5.8	497.3 ± 7.8
endcap C disk 4	-0.4 ± 0.4	74.2 ± 0.4	-5.4 ± 5.6	451.1 ± 7.8
endcap C disk 5	-2.2 ± 0.8	72.8 ± 0.8	0.6 ± 8.7	605.4 ± 9.2
endcap C disk 6				
endcap C disk 7	-1.6 ± 1.8	74.7 ± 2.1	6.2 ± 22.5	625.3 ± 30.2
endcap C disk 8	2.1 ± 2.6	83.9 ± 2.8	-84.8 ± 69.4	948.4 ± 90.5
barrel layer 0	-0.0 ± 0.0	34.5 ± 0.0	-0.6 ± 0.2	101.1 ± 0.4
barrel layer 1	0.0 ± 0.0	31.9 ± 0.0	-0.1 ± 0.2	93.0 ± 0.3
barrel layer 2	-0.1 ± 0.0	31.2 ± 0.0	-0.3 ± 0.2	101.9 ± 0.4
barrel layer 3	-0.1 ± 0.0	38.5 ± 0.0	-0.3 ± 0.2	143.5 ± 0.4
endcap A disk 0	-1.3 ± 0.3	63.1 ± 0.3	16.6 ± 3.9	432.5 ± 6.1
endcap A disk 1	3.4 ± 0.2	68.2 ± 0.3	11.4 ± 4.1	515.3 ± 5.9
endcap A disk 2	3.4 ± 0.3	62.3 ± 0.3	8.4 ± 4.7	497.7 ± 7.3
endcap A disk 3	3.3 ± 0.3	58.8 ± 0.3	15.7 ± 6.2	510.7 ± 8.9
endcap A disk 4	-0.2 ± 0.3	63.9 ± 0.3	8.5 ± 6.4	484.4 ± 9.0
endcap A disk 5	-0.4 ± 0.5	61.1 ± 0.6	5.6 ± 7.7	465.8 ± 18.3
endcap A disk 6	0.2 ± 0.8	64.0 ± 0.8	-11.9 ± 14.5	568.1 ± 19.3
endcap A disk 7	-4.1 ± 1.1	63.6 ± 1.1	-9.0 ± 21.5	619.0 ± 34.2
endcap A disk 8	-3.3 ± 1.5	61.7 ± 1.5	-21.4 ± 22.0	522.2 ± 33.1

Table 5.9: *Same as Table 5.2, but for the SCT residual distributions with final alignment corrections. Statistical uncertainties quoted as 0.0 are smaller than 0.05.*

Track parameter resolution

The alignment corrections obtained at different levels of granularity are further validated with a special alignment monitoring and validation software tool [85, 86]. With this tool it is possible to study the impact of remaining misalignments on the track parameter resolution, utilizing the special properties of the cosmic muons traversing the full Inner Detector and not originating from the nominal interaction point. For this purpose, tracks that go through the barrel part of the Pixel and SCT detector are split into an upper and a lower half. Hits with Y > 0 are associated to the upper track segment and hits with Y < 0 are associated to the lower track segment. Both track segments are then fitted independently and the track parameters are extrapolated to the common perigee to be comparable. The difference of the upper and lower track parameters gives an indication of the achievable track parameter resolution.

To validate the alignment corrections obtained with the *Local* χ^2 alignment approach, this procedure was applied to a run with magnetic field with 20k tracks reconstructed in the Pixel and SCT detector. The resulting track parameter resolution distributions are shown in figures 5.30 - 5.33. Figure 5.30 shows the track parameter resolution distributions without alignment corrections and with level 1 alignment corrections. Similarly, Figure 5.31 shows the comparison of the track parameter resolutions with level 1 and level 2 corrections. In Figure 5.32 the same is shown for level 2 and level 3 alignment corrections. Finally, Figure 5.33 shows the same comparison for level 3 alignment and the final alignment corrections after 25 additional level 2 iterations.

It is apparent that the track parameter resolution improves with finer alignment granularity and that the track parameter resolution with the final alignment corrections is best. Still, the track parameter resolution distributions are not comparable with the final track parameter resolution that ATLAS aims for [31, 87]. This is only in part due to remaining misalignments but also due to the fact that the ATLAS Inner Detector is best suited to measure tracks that pass close to the interaction point (in fact, that originate from the interaction point) and is not optimized for tracks with a wide spectrum of d_0 parameters as shown in Figures 5.10a and 5.11a.

To quantify the quality of the obtained alignment parameters with respect to track parameter resolution would require the comparison with simulated results without misalignment (as it was done for the CTB alignment). These studies are ongoing and beyond the scope of this thesis.
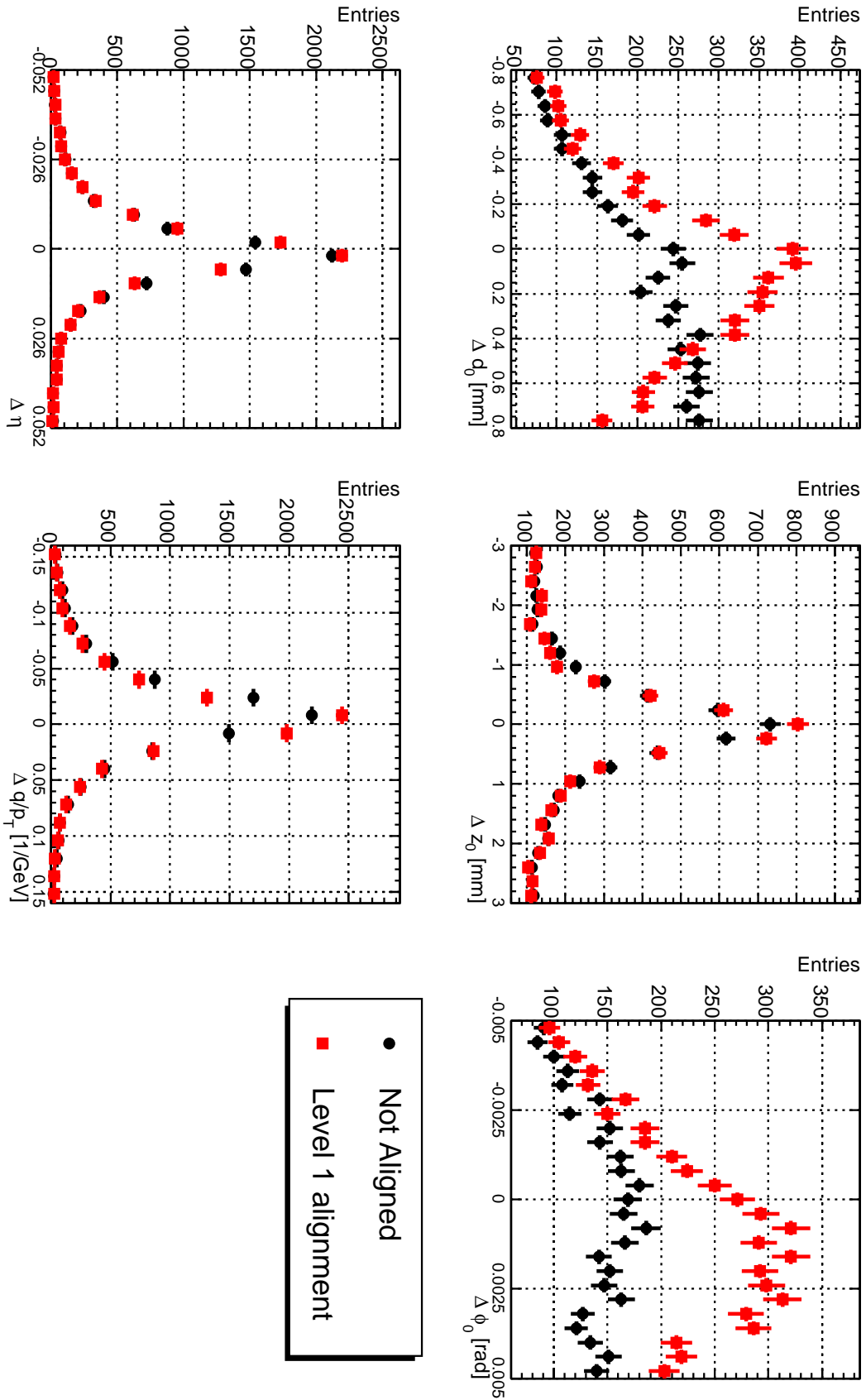
Figure 5.30: *Improvement of the resolution of the track parameters due to Level 1 alignment.*
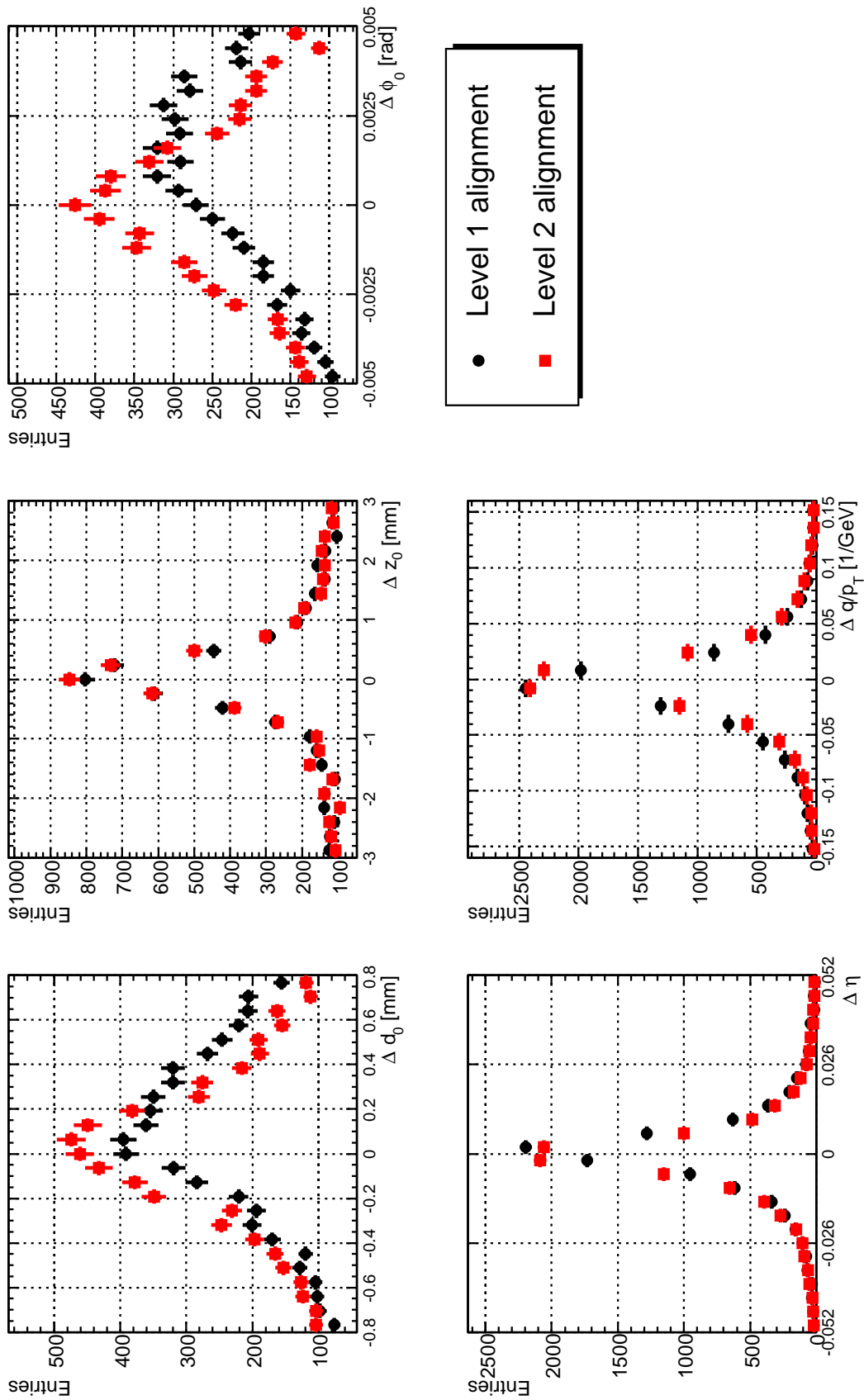
Figure 5.31: *Improvement of the resolution of the track parameters due to Level 2 alignment.*
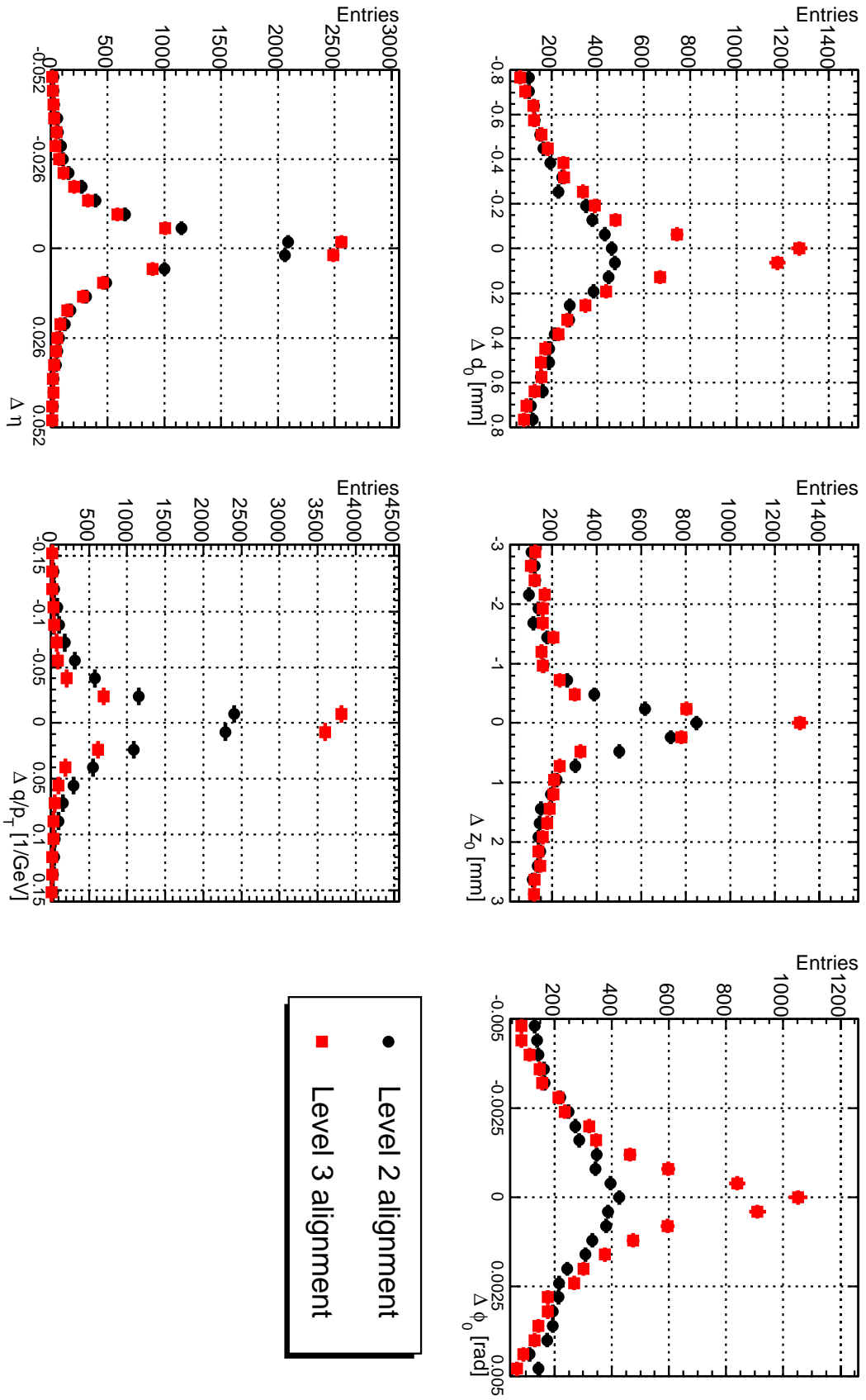
Figure 5.32: *Improvement of the resolution of the track parameters due to Level 3 alignment.*
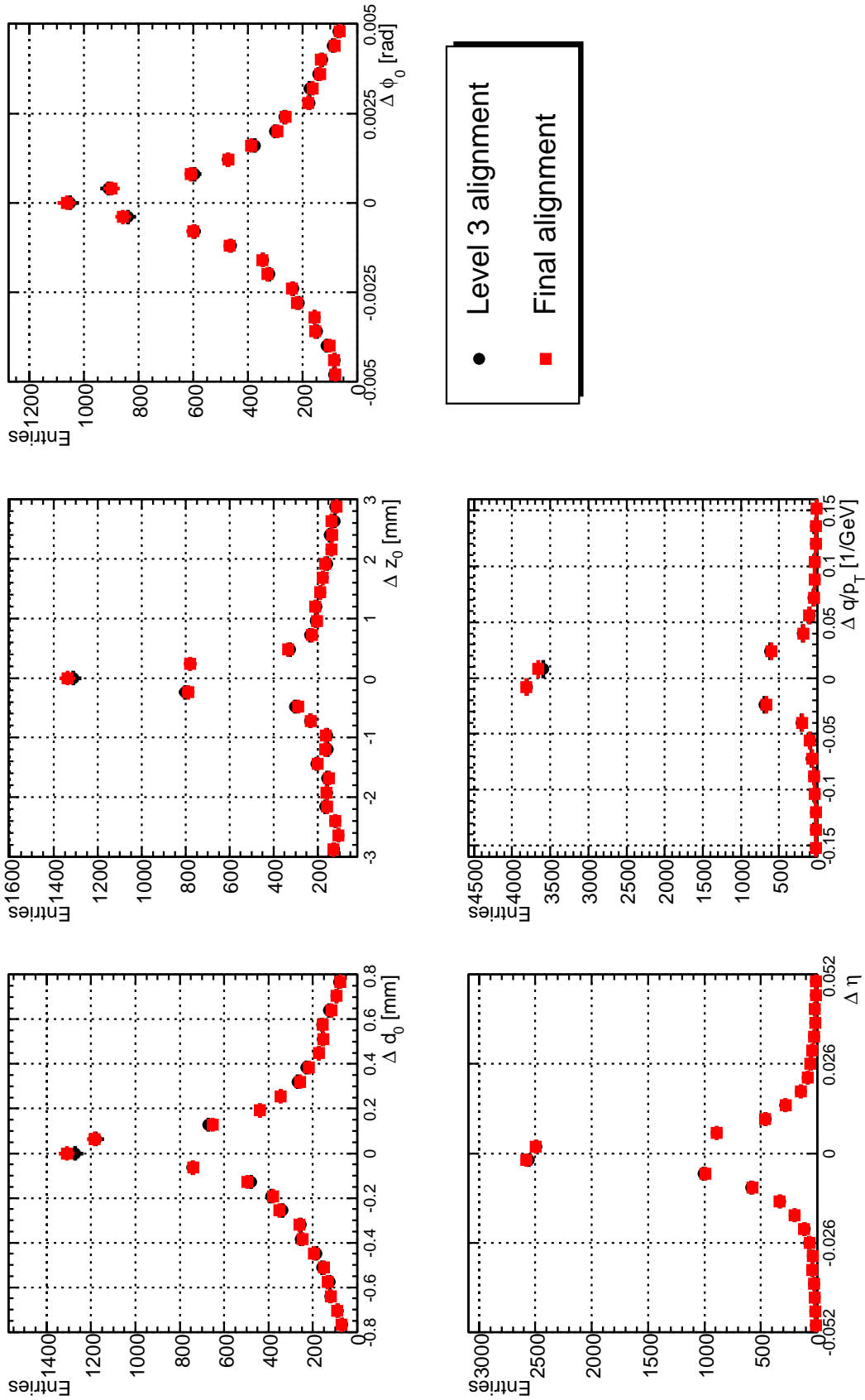
Figure 5.33: *Improvement of the resolution of the track parameters due to the final alignment corrections.*

5.6 Conclusions on the alignment of the Inner Detector

The *Local* χ^2 alignment approach and three other track-based alignment approaches were used successfully to align the CTB Inner Detector setup. This was the first time that the different ATLAS Inner Detector alignment approaches were tested with experimental data. The performance of the alignment approaches is assessed by studying reconstructed track parameters and comparing the results to simulation. All four approaches yield consistent results that agreed with simulation. Deviations are understood and can be explained by individual intrinsic limitations or constraints within the different alignment approaches. Among the four approaches the *Local* χ^2 alignment approach is the only one that provides alignment corrections for all six degrees of freedom for all the Pixel and SCT modules in the CTB Inner Detector setup.

The initially degraded track parameter resolution of the misaligned CTB Inner Detector setup is recovered up to the resolution obtainable without misalignment. This is a promising result that suggests that the ATLAS Inner Detector alignment strategy is successful and that the alignment approaches will be able to provide high-quality alignment parameters for the whole ATLAS Inner Detector.

In pursuit of this goal the *Local* χ^2 alignment approach was used to align the whole Pixel and SCT detector with cosmic muon tracks. These muon tracks illuminate the Pixel and SCT barrel well and an alignment of individual modules was successfully performed for this part of the detector. The remaining random misalignments for the Pixel barrel modules are $40\,\mu$m along the short readout coordinate and $60\,\mu$m along the long readout coordinate. For the SCT barrel modules the remaining random misalignments are $25\,\mu$m.

Because of the incident angle of the cosmic muons the Pixel and SCT endcaps are only poorly illuminated and consequently, only an alignment at the level of individual disks was performed. The remaining module misalignments are less than $100\,\mu$m for the Pixel endcaps and $60\,\mu$m - $70\,\mu$m for the SCT endcaps.

Applying the alignment corrections obtained with *Local* χ^2 approach results in a significant improvement of the track parameter resolution. For a minimal impact on the track parameter resolution the random misalignments of the Pixel modules need to be less than $7\,\mu$m along the short readout coordinate and for the SCT modules less than $12\,\mu$m. Consequently, improvements are still necessary, especially for the endcap alignment. Nonetheless, the alignment performed with cosmic muons is a promising starting point for the alignment of the ATLAS Inner Detector with collision data in 2009.

Chapter 6

Conclusions

Within the scope of this thesis a commissioning style top quark mass analysis for the ATLAS detector was successfully implemented and tested with Monte Carlo datasets. The analysis is tailored to select events from top quark pair decays in the lepton+jets decay channel. The event selection is based purely on kinematic selection cuts and no b-tagging information is used. With the selection cuts presented in Chapter 3 the $e + $ jets $t\bar{t}$ decay channel is selected with an efficiency of 8.7% whereas the $\mu + $ jets channel is selected with an efficiency of 14.2%. A selection purity of 52% is reached with most of the background contribution coming from combinatorial background of the signal datasets themselves, followed by W+jets and single top events. It needs to be noted however that no background from QCD multijet production was considered, because no Monte Carlo datasets were available for this process. QCD multijet production can become a major source of background if the rate of fake lepton reconstruction is high ($\mathrm{p}_{fake} > 10^{-3}$). This is mainly a detector performance issue that cannot be reliably estimated with simulated data but needs to be quantified with collision data.

In the selected events the mass of the hadronically decaying top quarks is reconstructed by 4-vector addition of the three jets that yield the highest p_T sum. For the standard analysis H1-weighted Cone jets with $\mathrm{R}_{cone} = 0.4$ are used. It is possible to perform a parasitic measurement of the W boson mass by selecting two of the three top quark decay jets. Three different methods for this di-jet selection were studied. Instead of performing a W boson mass measurement it is in principle possible to refine the event selection further by imposing a requirement on the reconstructed W boson mass. However, the findings from Chapter 4 indicate that there are shortcomings of all three methods of W boson reconstruction. Two of the methods yield unstable results under a variation of the input statistics, the underlying jet algorithm or the jet energy scale and the third method introduces a strong artificial bias towards the input W boson mass. Consequently, a purification of the event selection via a W boson mass requirement is not advisable and indeed not necessary for this top quark mass analysis.

The reconstructed top quark mass is about $7\,\mathrm{GeV}$ lower than the input top quark mass. The reconstructed W boson mass however is in very good agreement with the input W boson mass. This comes from the fact that the light jet energy scale is well calibrated for the used Monte Carlo datasets whereas the b-jet energy scale is not yet calibrated.

The standard analysis was modified in three ways to estimate the influence of different

sources of uncertainty. The kinematics of the jet selection, the underlying jet algorithm and the jet energy scale were varied. It is found that softer jet selection cuts result in a lower reconstructed top quark mass. Lowering the p_T requirement for one jet from $40\,\text{GeV}$ to $20\,\text{GeV}$ results in a $4\,\text{GeV}$ reduction of the reconstructed top quark mass. Another effect of softer jet selection cuts is a reduced signal purity.

The performance of the analysis was studied for different jet algorithms, i.e. Cone and k_T type algorithms with different steering parameters. Also, two different methods of jet calibration, namely H1-weighting and local hadron calibration were tested. Cone type and k_T type algorithms were compared with H1-weighted jets and it is found that both Cone and inclusive k_T jets with an R-parameter of 0.4 perform equally well. The reconstructed top quark mass difference for these two jet algorithms is $2\,\text{GeV}$. This number is not an uncertainty for the top quark mass measurement, but an estimate of the expected bias.

The different execution modes of the k_T algorithm (inclusive and exclusive) were compared with local hadron calibrated jets. Unfortunately, the calibration constants were not yet final and resulted in an underestimation of the hadronic jet energy scale of 8%. This had a severe impact on the cut-based event selection and the stability of the top quark mass reconstruction. A general observation is that a too small jet size parameter ($R < 0.4$) or a too large parameter ($R > 0.7$) yields degraded results. Also, inclusive and exclusive k_T jets yield inherently different reconstructed top quark masses on two different energy scales. This clearly means that any form of jet calibration will have to be tailored to a specific jet algorithm.

A large systematic uncertainty of the reconstructed top quark mass comes from the uncertainty on the jet energy scale. The jet energy scale has a direct correlation with the reconstructed top quark mass. Depending on the underlying jet algorithm it is found that 1% uncertainty on the jet energy scale results in 0.6% - 0.9% uncertainty on the reconstructed top quark mass.

A main result of these studies was to ascertain the validity of specific choices of jet algorithms, namely Cone and inclusive k_T jet algorithms with an R-parameter of 0.4. This is a first step towards an initial top quark mass measurement at ATLAS. Future steps towards this measurement will require a repetition of the analysis with Monte Carlo datasets simulated with different top quark input masses to determine correction factors for the various observed discrepancies between simulated and reconstructed top quark masses.

The top quark mass analysis depends on electron and muon reconstruction for event selection. Both lepton reconstruction algorithms use Inner Detector tracks to reconstruct and calculate the lepton 4-momenta. The performance of both lepton reconstruction algorithms and thus the quality of the event selection of the analysis directly depends on the quality of the alignment of the ATLAS Inner Detector. Also, any refinement of the analysis that will involve b-tagging needs high quality alignment. One important ingredient in b-tagging is secondary vertex reconstruction and the quality of this is directly affected by residual Pixel misalignment.
To address the issue of a high quality Inner Detector alignment the second part of this thesis deals with the alignment of the ATLAS Pixel and SCT detectors. The alignment is done with the *Local* χ^2 alignment approach. The approach was successfully used to align the combined testbeam Inner Detector setup. The alignment results are compared with Monte Carlo simulated values and with the results of three other alignment approaches. With the *Local* χ^2 alignment corrections the track parameter resolutions are restored to

their nominal values derived from Monte Carlo simulation. The agreement with the other approaches is good and any deviations are understood in terms of individual intrinsic limitations or constraints within the different approaches. Among the four alignment approaches the *Local* χ^2 approach is the only one that provides alignment corrections for all six degrees of freedom for all the Pixel and SCT modules in the CTB Inner Detector setup.

The *Local* χ^2 approach was used to align the whole Pixel and SCT detectors with cosmic muon tracks recorded during six weeks of cosmic data-taking with ATLAS in fall 2008. As input 141k tracks from runs without magnetic field and 658k tracks from runs with magnetic field were used. The Pixel and SCT barrel modules are better illuminated with cosmic muon tracks than the endcap modules due to the angular distribution of cosmic muons in the ATLAS cavern. Consequently, an alignment of the individual modules was performed for the barrel, whereas the endcaps were only aligned at the level of disks. This means that alignment corrections for the six degrees of freedom of a rigid body were determined with the *Local* χ^2 approach for the 1456 Pixel and 2112 SCT barrel modules and for the 6 Pixel and 18 SCT endcap disks, 21.5k alignment constants in total.

From the width of the residual distributions after the alignment the size of the remaining random misalignments can be inferred. For the Pixel endcap modules the remaining random misalignment is less than $100\,\mu$m and $60\,\mu$m - $70\,\mu$m for the SCT endcap modules. The remaining random misalignments for the Pixel barrel modules are $40\,\mu$m along the short readout coordinate and $60\,\mu$m along the long readout coordinate. For the SCT barrel modules the remaining random misalignments are $25\,\mu$m.

Applying the alignment corrections obtained with *Local* χ^2 approach results in a significant improvement of the track parameter resolution. For a minimal impact on the track parameter resolution the random misalignments of the Pixel modules need to be less than $7\,\mu$m along the short readout coordinate and for the SCT modules less than $12\,\mu$m. Consequently, improvements are still necessary, especially for the endcap alignment. Nonetheless, the alignment of the whole Pixel and SCT subdetectors performed with recorded cosmic muon data is an encouraging result and a promising starting point for the alignment of the ATLAS Inner Detector with collision data later this year.

List of Figures

List of Tables

Bibliography

[1] The ATLAS Collaboration, *Jets from Light Quarks in $t\bar{t}$ Events*, CERN, Geneva, 2008, Chapter in [38].

[2] R. Härtel, Alignment of the ATLAS Inner Detector, in *XI International Workshop on Advanced Computing and Analysis Techniques in Physics Research*, 2007, PoS(ACAT)049.

[3] A. Ahmad et al., *Alignment of the Pixel and SCT Modules for the 2004 ATLAS Combined Test Beam*, JINST **3** (2008) P09004.

[4] S. Glashow, *Partial Symmetries of Weak Interactions*, Nucl. Phys. **22** (1961) 579.

[5] S. Weinberg, *A Model of Leptons*, Phys. Rev. Lett. **19** (1967) 1264.

[6] A. Salam, Elementary particle theory, p. 367, Almqvist and Wiksell, Stockholm, 1968.

[7] H. Fritzsch and M. Gell-Mann, Proc. XVI Int. Conf. on High Energy Physics, Chicago-Batavia (1972).

[8] G. Altarelli, *Status of the Standard Model at the LHC Start*, Nuovo Cim. **123B** (2008) 257.

[9] J. Wess and B. Zumino, *Supergauge Transformations in Four-Dimensions*, Nucl. Phys. **B70** (1974) 39.

[10] N. Arkani-Hamed, S. Dimopoulos, and G. Dvali, *The hierarchy problem and new dimensions at a millimetre*, Phys. Lett. **B429** (1998) 263.

[11] M.B. Green and J.H. Schwarz, *Anomaly Cancellation in Supersymmetric D=10 Gauge Theory and Superstring Theory*, Phys. Lett. **B149** (1984) 117.

[12] M. Gell-Mann, *A schematic model of baryons and mesons*, Phys. Rev. Lett. **8** (1964) 214.

[13] (CDF and D0 Collab.), *A Combination of CDF and D0 Results on the Mass of the Top Quark*, (2008), 0803.1683 [hep-ex].

[14] S. Bethke, *Experimental Tests of Asymptotic Freedom*, Prog. Part. Nucl. Phys. **58** (2007) 351.

[15] P. Higgs, *Broken symmetries, massless particles and gauge fields*, Phys. Lett. **12** (1964) 132.

[16] N. Cabibbo, *Unitary Symmetry and Leptonic Decays*, Phys. Rev. Lett. **10** (1963) 531.

[17] M. Kobayashi and T. Maskawa, *CP Violation in the Renormalizable Theory of Weak Interaction*, Prog. Theor. Phys. **49** (1973) 652.

[18] B. Pontecorvo, *Inverse beta processes and nonconservation of lepton charge*, Sov. Phys. JETP **7** (1958) 172.

[19] Z. Maki, M. Nakagawa, and S. Sakata, *Remarks on the unified model of elementary particles*, Prog. Theor. Phys. **28** (1962) 870.

[20] F. Abe et al. (CDF Collab.), *Observation of top quark production in $\bar{p}p$ collisions*, Phys. Rev. Lett. **74** (1995) 2626.

[21] S. Abachi et al. (D0 Collab.), *Observation of the top quark*, Phys. Rev. Lett. **74** (1995) 2632.

[22] J.C. Collins and D.E. Soper, *The Theorems of Perturbative QCD*, Ann. Rev. Nucl. Part. Sci. **37** (1987) 383.

[23] A. Quadt, *Top quark physics at hadron colliders*, Eur. Phys. J. **C48** (2006) 835.

[24] J. Pumplin et al., *New generation of parton distributions with uncertainties from global QCD analysis*, JHEP **07** (2002) 012.

[25] M. Cacciari et al., *Updated predictions for the total production cross sections of top and of heavier quark pairs at the Tevatron and at the LHC*, JHEP **09** (2008) 127.

[26] G.O. Dovier, *Single top cross section*, `http://indico.cern.ch/materialDisplay.py?contribId=5&materialId=slides&confId=25493`, ATLAS internal presentation.

[27] C. Amsler et al. (Particle Data Group Collab.), *Review of Particle Physics*, Phys. Lett. **B667** (2008).

[28] M. Jezabek and J.H. Kuhn, *QCD Corrections to Semileptonic Decays of Heavy Quarks*, Nucl. Phys. **B314** (1989) 1.

[29] L. Evans et al., *LHC Machine*, JINST **3** (2008) S08001.

[30] K. Aamodt et al. (ALICE Collab.), *The ALICE experiment at the CERN LHC*, JINST **3** (2008) S08002.

[31] G. Aad et al. (ATLAS Collab.), *The ATLAS Experiment at the CERN Large Hadron Collider*, JINST **3** (2008) S08003.

[32] R. Adolphi et al. (CMS Collab.), *The CMS experiment at the CERN LHC*, JINST **3** (2008) S08004.

[33] A.A. Alves et al. (LHCb Collab.), *The LHCb Detector at the LHC*, JINST **3** (2008) S08005.

[34] The ATLAS Collaboration, *ATLAS Detector and physics performance: Technical design report*, CERN-LHCC-99-14.

[35] The ATLAS Collaboration, *ATLAS Detector and physics performance: Technical design report*, CERN-LHCC-99-15.

[36] The ATLAS Collaboration, *ATLAS First Level Trigger: Technical design report*, CERN-LHCC-98-14.

[37] The ATLAS Collaboration, *ATLAS High Level Trigger Data Acquisition and Controls: Technical design report*, CERN-LHCC-2003-22.

[38] The ATLAS Collaboration, *Expected Performance of the ATLAS Experiment Detector, Trigger, Physics*, CERN, Geneva, 2008, CERN-OPEN-2008-020, ISBN978-92-9083-321-5.

[39] A. Ahmad et al., *The Silicon microstrip sensors of the ATLAS semiconductor tracker*, Nucl. Instrum. Meth. **A578** (2007) 98.

[40] S. Goldfarb and A. Schaffer, *Definition of Off-line Readout Identifiers for the ATLAS Detector*, ATL-SOFT-2001-004 (2001).

[41] *MPP top quark mass analysis software repository*, `http://atlas-sw.cern.ch/cgi-bin/viewcvs-atlas.cgi/groups/MPP/TopQuarkAnalysis/`.

[42] S.C.M. Bentvelsen and M. Cobal, *Top studies for the Atlas detector commissioning*, CERN, Geneva, 2005, ATL-PHYS-PUB-2005-024.

[43] A. Doxiadis and M. Kayl, *Estimating the isolated lepton rate in multi-jet events*, ATLAS internal Note, ATL-COM-PHYS-2008-004 (2008).

[44] B.P. Kersevan and E. Richter-Was, *The Monte Carlo event generator AcerMC version 2.0 with interfaces to PYTHIA 6.2 and HERWIG 6.5*, (2004), hep-ph/0405247.

[45] M.L. Mangano et al., *ALPGEN, a generator for hard multiparton processes in hadronic collisions*, JHEP **07** (2003) 001.

[46] S. Frixione and B.R. Webber, *Matching NLO QCD computations and parton shower simulations*, JHEP **06** (2002) 029.

[47] S. Frixione, P. Nason and B.R. Webber, *Matching NLO QCD and parton showers in heavy flavour production*, JHEP **08** (2003) 007.

[48] T. Sjöstrand, S. Mrenna, and P. Skands, *PYTHIA 6.4 physics and manual*, JHEP **05** (2006) 026.

[49] G. Corcella et al., *HERWIG 6.5: An event generator for Hadron Emission Reactions With Interfering Gluons (including supersymmetric processes)*, JHEP **01** (2001) 010.

[50] J.M. Butterworth, J.R. Forshaw and M.H. Seymour, *Multiparton interactions in photoproduction at HERA*, Z. Phys. **C72** (1996) 637.

[51] S. Agostinelli et al. (GEANT4 Collab.), *GEANT4: A simulation toolkit*, Nucl. Instrum. Meth. **A506** (2003) 250.

[52] M.L. Mangano, *Merging Matrix elements and shower MCs*, `http://cern.ch/~mlm/talks/lund-alpgen.pdf`, Talk at Lund University.

[53] The ATLAS Collaboration, *Reconstruction and Identification of Electrons*, CERN, Geneva, 2008, Chapter in [38].

[54] S. Hassani et al., *A muon identification and combined reconstruction procedure for the ATLAS detector at the LHC using the (MUONBOY, STACO, MuTag) reconstruction packages*, Nucl. Instrum. Meth. **A572** (2007) 77.

[55] W. Lampl et al., *Calorimeter Clustering Algorithms: Description and Performance*, CERN, Geneva, 2008, ATL-LARG-PUB-2008-002.

[56] G.C. Blazey et al., *Run II jet physics*, (2000), hep-ex/0005012.

[57] I. Abt et al. (H1 Collab.), *The Tracking, calorimeter and muon detectors of the H1 experiment at HERA* , Nucl. Instrum. Meth. **A386** (1997) 348.

[58] The ATLAS Collaboration, *Measurement of Missing Transverse Energy*, CERN, Geneva, 2008, Chapter in [38].

[59] M. Abramowitz and I. Stegun, *Handbook of Mathematical Functions with Formulas, Graphs, and Mathematical Tables*, Dover, New York, ninth dover printing, tenth gpo printing edition, 1964.

[60] F. Fiedler, *Independent measurement of the top quark mass and the light- and bottom-jet energy scales at hadron colliders*, Eur. Phys. J. **C53** (2008) 41.

[61] T. Barillari et al., *Local Hadronic Calibration*, CERN, Geneva, 2008, ATL-LARG-PUB-2009-001.

[62] The ATLAS Collaboration, *Detector Level Jet Corrections*, CERN, Geneva, 2008, Chapter in [38].

[63] J.M. Butterworth et al., *KtJet: A C++ implementation of the K(T) clustering algorithm*, Comput. Phys. Commun. **153** (2003) 85.

[64] M. Cacciari and G.P. Salam, *Dispelling the N**3 myth for the k(t) jet-finder*, Phys. Lett. **B641** (2006) 57.

[65] R. Härtel, Iterative local χ^2 alignment approach for the ATLAS SCT detector, Diploma thesis, TU München, 2005, MPP-2005-174.

[66] T. Göttfert, Iterative local χ^2 alignment algorithm for the ATLAS Pixel detector, Diploma thesis, Universität Würzburg, 2006, MPP-2006-118.

[67] S. Haywood, *Local Coordinate Frames for the Alignment of Silicon Detectors*, CERN, Geneva, 2004, ATL-INDET-2004-001.

[68] F. Åkesson et al., *ATLAS Tracking Event Data Model*, CERN, Geneva, 2006, CERN-ATL-COM-SOFT-2006-005.

[69] S. Gonzalez-Sevilla, private communication.

[70] A. Bocci and W. Hulsbergen, *TRT Alignment For SR1 Cosmics and Beyond*, CERN, Geneva, 2007, CERN-ATL-COM-INDET-2007-011.

[71] T. Cornelissen, *Track fitting in the ATLAS experiment*, PhD thesis, Universiteit van Amsterdam (Netherlands), 2006.

[72] F. Heinemann, *Robust Track Based Alignment of the ATLAS Silicon Detectors and Assessing Parton Distribution Uncertainties in Drell-Yan Processes*, PhD thesis, University of Oxford, 2007.

[73] S. Gonzalez-Sevilla, *Inner Detector performance and alignment studies*, PhD thesis, Universitat de Valencia, 2007.

[74] P. Bruckman de Renstrom, A. Hicheur and S. Haywood, *Global χ^2 approach to the Alignment of the ATLAS Silicon Tracking Detectors*, ATLAS internal Note, ATL-COM-INDET-2005-004 (2005).

[75] T. Golling, *Alignment of the Silicon Tracking Detector using Survey Constraints*, CERN, Geneva, 2006, CERN-ATL-INDET-PUB-2006-001.

[76] T. K. Gaisser, *Cosmic rays and particle physics*, Cambridge, UK: Univ. Pr. (1990) 279 p.

[77] K. Greisen, *Cosmic ray showers*, Ann. Rev. Nucl. Part. Sci. **10** (1960) 63.

[78] J. von Loeben, *First cosmic ray results of the ATLAS barrel muon spectrometer with magnetic field*, **3** (2007) 1891 , Nuclear Science Symposium Conference Record, 2007. NSS '07. IEEE.

[79] N. Konstantinidis et al., *Fast tracking for the ATLAS LVL2 Trigger*, CERN Yellow Report, ATL-DAQ-CONF-2005-001.

[80] C. Schiavi et al., *Fast Tracking for the Second Level Trigger of the ATLAS Experiment Using Silicon Detectors Data*, ATLAS Note, ATL-DAQ-CONF-2005-011.

[81] M. Karagöz Ünel et al., *Cosmic alignment run list*, `https://twiki.cern.ch/twiki/bin/view/Atlas/InDetAlignCosmicCavern`, ATLAS Computing Wiki.

[82] P. Achard et al. (L3 Collab.), *Measurement of the atmospheric muon spectrum from 20-GeV to 3000-GeV*, Phys. Lett. **B598** (2004) 15.

[83] E. Abat et al. (ATLAS Collab.), *Combined performance tests before installation of the ATLAS Semiconductor and Transition Radiation Tracking Detectors*, Journal of Instrumentation **3** (2008) P08003.

[84] G. Gorfine, *Savannah bug report*, `https://savannah.cern.ch/bugs/?44402`, known software defect of release 14.5.0.

[85] T. Golling et al., *InDetAlignmentMonitoring*, `https://twiki.cern.ch/twiki/bin/view/Atlas/InDetAlignmentMonitoring`, ATLAS Computing Wiki.

[86] *Inner Detector alignment monitoring software repository*, `http://atlas-sw.cern.ch/cgi-bin/viewcvs-atlas.cgi/offline/InnerDetector/InDetMonitoring/InDetAlignmentMonitoring/`.

[87] The ATLAS Collaboration, *ATLAS Inner Detector: Technical design report Vol. 1*, CERN-LHCC-97-16.

Acknowledgements